NAVAL POSTGRADUATE SCHOOL

MONTEREY, CALIFORNIA

THESIS

**INFLUENCE OF MOMENTUM EXCESS
ON THE PATTERN AND DYNAMICS OF
INTERMEDIATE-RANGE STRATIFIED WAKES**

by

Michael A. Martin

June 2016

Thesis Advisor: Timour Radko
Second Reader: Peter Chu

Approved for public release; distribution is unlimited

THIS PAGE INTENTIONALLY LEFT BLANK

REPORT DOCUMENTATION PAGE		*Form Approved OMB No. 0704-0188*

Public reporting burden for this collection of information is estimated to average 1 hour per response, including the time for reviewing instruction, searching existing data sources, gathering and maintaining the data needed, and completing and reviewing the collection of information. Send comments regarding this burden estimate or any other aspect of this collection of information, including suggestions for reducing this burden, to Washington headquarters Services, Directorate for Information Operations and Reports, 1215 Jefferson Davis Highway, Suite 1204, Arlington, VA 22202-4302, and to the Office of Management and Budget, Paperwork Reduction Project (0704-0188) Washington, DC 20503.

1. AGENCY USE ONLY (*Leave blank*)	2. REPORT DATE June 2016	3. REPORT TYPE AND DATES COVERED Master's Thesis	
4. TITLE AND SUBTITLE INFLUENCE OF MOMENTUM EXCESS ON THE PATTERN AND DYNAMICS OF INTERMEDIATE-RANGE STRATIFIED WAKES		**5. FUNDING NUMBERS**	
6. AUTHOR(S) Michael A. Martin			
7. PERFORMING ORGANIZATION NAME(S) AND ADDRESS(ES) Naval Postgraduate School Monterey, CA 93943-5000		**8. PERFORMING ORGANIZATION REPORT NUMBER**	
9. SPONSORING /MONITORING AGENCY NAME(S) AND ADDRESS(ES) N/A		**10. SPONSORING / MONITORING AGENCY REPORT NUMBER**	

11. SUPPLEMENTARY NOTES The views expressed in this thesis are those of the author and do not reflect the official policy or position of the Department of Defense or the U.S. Government. IRB Protocol number __N/A__.

12a. DISTRIBUTION / AVAILABILITY STATEMENT Approved for public release; distribution is unlimited	12b. DISTRIBUTION CODE A

13. ABSTRACT (maximum 200 words)

Submerged bodies propagating in stratified fluids frequently create disturbances in temperature, salinity, and momentum that are detectable at the air-sea interface. This project includes the addition of momentum excess in order to model the fundamental differences between signatures generated by towed and self-propelled bodies in various ocean states. In cases where the body forces, form drag and thrust were balanced, fewer and less expansive surface signatures were observed. In cases where the balance was disturbed by either lack or excess of self-propulsion, a greater perturbation was achieved, particularly in the ocean interior. Discovering the significance of the internal, intermediate-range wakes has transformed the focus of the entire study. With the increasing employment of unmanned underwater vehicles, it is equally imperative to research the internal ocean dynamics as it is to study the physics at the surface. This study was focused on direct numerical simulations. However, the data collected in this investigation have produced new insights into the dynamics of stratified wakes, which can be used on the operational level for developing and improving algorithms for non-acoustic signature prediction and detection.

14. SUBJECT TERMS stratified wakes, direct numerical simulations, momentum excess, dimensional analysis, surface thermal signatures, internal velocity signatures	15. NUMBER OF PAGES 111
	16. PRICE CODE

17. SECURITY CLASSIFICATION OF REPORT Unclassified	18. SECURITY CLASSIFICATION OF THIS PAGE Unclassified	19. SECURITY CLASSIFICATION OF ABSTRACT Unclassified	20. LIMITATION OF ABSTRACT UU

THIS PAGE INTENTIONALLY LEFT BLANK

INFLUENCE OF MOMENTUM EXCESS ON THE PATTERN AND DYNAMICS OF INTERMEDIATE-RANGE STRATIFIED WAKES

Michael A. Martin
Lieutenant, United States Navy
B.S., United States Naval Academy, 2009

Submitted in partial fulfillment of the
requirements for the degree of

**MASTER OF SCIENCE IN METEOROLOGY
AND PHYSICAL OCEANOGRAPHY**

from the

**NAVAL POSTGRADUATE SCHOOL
June 2016**

Approved by: Timour Radko
Thesis Advisor

Peter Chu
Second Reader

Peter Chu
Chair, Department of Oceanography

THIS PAGE INTENTIONALLY LEFT BLANK

ABSTRACT

Submerged bodies propagating in stratified fluids frequently create disturbances in temperature, salinity, and momentum that are detectable at the air-sea interface. This project includes the addition of momentum excess in order to model the fundamental differences between signatures generated by towed and self-propelled bodies in various ocean states. In cases where the body forces, form drag and thrust were balanced, fewer and less expansive surface signatures were observed. In cases where the balance was disturbed by either lack or excess of self-propulsion, a greater perturbation was achieved, particularly in the ocean interior. Discovering the significance of the internal, intermediate-range wakes has transformed the focus of the entire study. With the increasing employment of unmanned underwater vehicles, it is equally imperative to research the internal ocean dynamics as it is to study the physics at the surface. This study was focused on direct numerical simulations. However, the data collected in this investigation have produced new insights into the dynamics of stratified wakes, which can be used on the operational level for developing and improving algorithms for non-acoustic signature prediction and detection.

THIS PAGE INTENTIONALLY LEFT BLANK

TABLE OF CONTENTS

LIST OF FIGURES

x

THIS PAGE INTENTIONALLY LEFT BLANK

LIST OF TABLES

THIS PAGE INTENTIONALLY LEFT BLANK

LIST OF ACRONYMS AND ABBREVIATIONS

CFD	Computational Fluid Dynamics
DNS	Direct Numerical Simulations
HPCMP	High Performance Computing Modernization Program
MITgcm	Massachusetts Institute of Technology General Circulation Model
MLD	Mixed Layer Depth
PSU	Practical Salinity Units
RMS	Root Mean Square
SAR	Synthetic Aperture Radar
SB	Submerged Body
SONAR	Sound Navigation and Ranging
SSB	Self-propelled Submerged Body
TACC	University of Texas at Austin's Advanced Computing Center
T-S	Temperature and Salinity
UUV	Unmanned Underwater Vehicle
WOA13	World Ocean Atlas 2013
WOD13	World Ocean Database 2013

THIS PAGE INTENTIONALLY LEFT BLANK

ACKNOWLEDGMENTS

My thesis advisor, Dr. Radko, was instrumental in rousing the dream behind this research and encouraging me to continue to dive deeper into the study. I am honored to be supported by my loving family, especially my husband, Rob. His silent service in honor of our great nation inspired my interest in exploring both of our lines of duty: oceanography and submarines. With a heart of gold, he believed in me beyond my own faith. And of course, I have to thank my Lord and savior, Jesus Christ.

THIS PAGE INTENTIONALLY LEFT BLANK

I.   INTRODUCTION

Fluid mechanics is the study of fluids and the forces that act upon them. Depending on flow characteristics, they can be subdivided into fluid statics for fluids at rest or fluid dynamics for those in motion (Landau and Lifshitz 1987). This study solely focuses on fluid dynamics; more specifically, the dynamic responses of fluid flows interacting with submerged bodies. The Navier-Stokes equations, which uniquely describe many fluid flows, comprise the complex foundation on which this study was modeled. Fortunately, the computational power necessary to solve this intricate series of equations is more readily accessible with the advent of high-performance supercomputers. Computational fluid dynamics (CFD) is the method to study fluid flows by solving the Navier-Stokes equations using numerical analysis and algorithms (Diamessis et al. 2010), as shown in Figure 1. The Massachusetts Institute of Technology Global Circulation Model (MITgcm) uses the full Navier-Stokes equations in their setup to replicate oceanic and atmospheric motions. This intricate series of codes allows the addition of small perturbations, vorticity, viscosity, boundary conditions, and a number of other variations which more closely realize environmental flows (Adcroft et al. 2004).

$$\begin{cases}
\dfrac{\partial u}{\partial t} + u\dfrac{\partial u}{\partial x} + v\dfrac{\partial u}{\partial y} + w\dfrac{\partial u}{\partial z} - fv = -\dfrac{1}{\rho}\dfrac{\partial p}{\partial x} + \upsilon\left(\dfrac{\partial^2 u}{\partial x^2} + \dfrac{\partial^2 u}{\partial y^2} + \dfrac{\partial^2 u}{\partial z^2}\right) \\[2em]
\dfrac{\partial v}{\partial t} + u\dfrac{\partial v}{\partial x} + v\dfrac{\partial v}{\partial y} + w\dfrac{\partial v}{\partial z} + fu = -\dfrac{1}{\rho}\dfrac{\partial p}{\partial y} + \upsilon\left(\dfrac{\partial^2 v}{\partial x^2} + \dfrac{\partial^2 v}{\partial y^2} + \dfrac{\partial^2 v}{\partial z^2}\right) \\[2em]
\dfrac{\partial w}{\partial t} + u\dfrac{\partial w}{\partial x} + v\dfrac{\partial w}{\partial y} + w\dfrac{\partial w}{\partial z} = -\dfrac{1}{\rho}\dfrac{\partial p}{\partial z} - g + \upsilon\left(\dfrac{\partial^2 w}{\partial x^2} + \dfrac{\partial^2 w}{\partial y^2} + \dfrac{\partial^2 w}{\partial z^2}\right) \\[2em]
\dfrac{\partial}{\partial t}T + u\dfrac{\partial}{\partial x}T + v\dfrac{\partial}{\partial y}T + w\dfrac{\partial}{\partial z}T = k_T\left(\dfrac{\partial^2 T}{\partial x^2} + \dfrac{\partial^2 T}{\partial y^2} + \dfrac{\partial^2 T}{\partial z^2}\right) \\[2em]
\dfrac{\partial}{\partial t}S + u\dfrac{\partial}{\partial x}S + v\dfrac{\partial}{\partial y}S + w\dfrac{\partial}{\partial z}S = k_S\left(\dfrac{\partial^2 S}{\partial x^2} + \dfrac{\partial^2 S}{\partial y^2} + \dfrac{\partial^2 S}{\partial z^2}\right) \\[2em]
\dfrac{\partial u}{\partial x} + \dfrac{\partial v}{\partial y} + \dfrac{\partial w}{\partial z} = 0 \\[2em]
\dfrac{\rho - \rho_0}{\rho_0} = \beta(S - S_0) - \alpha(T - T_0)
\end{cases}$$

Environmental flow variations are caused by pressure and density differences which change with fluctuations in temperature and salinity. [u, v, w are the velocities in the x, y, z directions. p is pressure, ρ represents density, T is temperature and S is for salinity].

Figure 1.   Navier-Stokes Equations of Motion

A.   FLUID FLOWS

Internal waves are gravity waves that propagate in the ocean interior and exist when the medium is stratified. Stratification occurs when the ocean layer densities vary with increasing depth. Temperature, salinity, and pressure changes lead to oceanic density changes (Klemas 2012). The restoring force for internal waves is buoyancy and the restoring tendency is often quantified using the Brunt-Väisälä Frequency, N, or buoyancy frequency. It determines the frequency at which a particle will oscillate if perturbed from its equilibrium. The strength of the stratification and the magnitude of the perturbation determine the size and dispersion of the internal waves generated (Diamessis et al. 2010). Generation of internal waves occurs when the stratified interface is interrupted or perturbed (Alpers 2015). The most common perturbations that drive internal waves in the ocean are bathymetric changes, atmospheric pressure variations, river outflow regions, and flows around a submerged object. The waves oscillate between density regimes and their phase speed travels along the stratification zones, but their energy or group speed traverses orthogonal to the phase. With spatial scales of several-kilometer zonal propagation, ten-meter vertical propagation, and temporal scales of hours, they are quite readily observable (Garrett and Munk 1979). In our study, we capture images of the zonal propagating waves with energy that reaches both to the surface of the ocean as well as its depths. The energy detected at the air-sea interface has an important connection to the initial disturbance.

The two dimensionless parameters that typically define fluid flow around a geometric body are the Froude number, Fr, and the Reynolds number, Re. In the ocean, we consider very large Re, to the point that this ratio is negligible with respect to our experiment. When the Re increases above a critical value, wakes generated from the interaction cause turbulent fluid mixing (Lin and Pao 1979). We also assume large Fr (Fr > 50) for these experiments. Therefore, unlike ship-wave patterns and dynamics, we consider a supercritical flow around the submerged body. Turbulent wakes generated in the lee of the SSB propagation transport environmental and source properties from the ocean interior to its surface and depths. These advected properties can be calculated and observed using the Navier-Stokes equations of motion in the MITgcm. Relatively cooler

temperatures and momentum excesses/deficits are transported to the surface by the turbulent wake energy. By resolving the temperature and velocity responses generated by the SSB, we will better understand the pattern and dynamics of turbulent wakes in stratified regimes.

The ability to measure real-time hydrodynamic anomalies, both at the ocean surface and interior, is becoming increasingly imperative to naval operators. Technological advances in strategic systems make remote measurements of these anomalies a more viable method for submersible detection than the traditional sound navigation and ranging (SONAR) acoustic detection. Understanding internal fluid turbulent motions and energy propagation will only increase remote detection capabilities. It similarly affords naval architects the knowledge for further design-stealth, and operators the optimal use of their tactical limitations.

B.   HISTORICAL STUDIES

Several related papers have linked biological phenomena as inspiration for this field of research. The fisherman bat (Noctilio leporinus) uses echolocation as a means to hunt its prey. Internal perturbations generated by the motions of fish below are detected at the water surface through bio sonar, and enable a precise strike (Schnitzler et al. 1994). This provoked a slew of research questions as well as great interest in testing remote sensing capabilities to detect submarine vessels.

Many studies have been conducted to understand fluid flows around submerged bodies, to better engineer the body for improved maneuverability, or to study a non-acoustic method of submerged body (SB) detection (Gallacher and Hebert 2008). Airborne sensors, multispectral and synthetic aperture radar (SAR) satellite imagery, and even space shuttle photos have visually traced large scale internal waves. There are limitations to consider in remote sensing that clutter the received signal. Wind-wave interaction at the sea surface, precipitation, atmospheric aerosols, and other elements are a few of the limiting factors. But technological advances in data acquisition and processing have improved sensing precision. Satellite infrared measurements of sea surface temperatures have an accuracy of approximately ± 0.1 degrees Celsius (°C)

4

(Emery et al. 2001). With this knowledge, we can roughly state temperature signatures with changes greater than 0.1°C, can be measured in real time. As doctors determine internal functions by observing symptoms on the surface of the human body, detecting ocean surface signatures enables a further understanding of internal wake dynamics. We are interested in the surface detection of disturbances simply because they can be measured by remote airborne sensors; but of equal importance are the dynamic responses in the ocean interior.

Two similar studies that precede this work using direct numerical simulations (DNS) to model surface signatures created by submerged bodies propagating in stratified fluids are Haun (2012) and Newman (2014). Haun focused on the late-wake signatures created in double diffusive or salt-finger convection regions. Newman concentrated on near-wake surface responses generated from broader stratifications observed in the mid-latitudes. Our study more closely resembles the setup and dynamic research of Newman (2014), with the intent to introduce the concept of momentum excess. This addition enables us to compare signatures of a self-propelled submerged body (SSB) with those generated by a towed body.

C.   MOMENTUM EXCESS

An additional forcing term is introduced when a submerged body is self-propelled. In a towed body case, there exists only a momentum wake induced by the drag force of the body interacting with the surrounding fluid medium. The net drag force consists of the pressure force, also known as the form drag, and frictional component. In the self-propelled body case, however, there exists the same drag force wake as well as a signature generated by the jet or propeller behind the sub, known as the thrust force. The misbalance between the drag and thrust forces ultimately lead to acceleration/deceleration of the object and it is often referred to as the momentum excess/deficit. In their paper on self-propelled wakes with moderate momentum excess, de Stadler and Sarkar (2011) discuss the differences in viewing the velocity profile of the two scenarios. For a towed body experiment, there is only a momentum deficit. When modeling a self-propelled body, a momentum deficit and excess can be represented (de Stadler and Sarkar, 2011).

By adjusting the momentum coefficient, we are able to visualize both surface and internal temperature and velocity signatures of SSBs in varying environmental flow fields.

D.   DIRECT NUMERICAL SIMULATION

The Navier-Stokes equations (Figure 1) describe the physics of fluid motions, and are not limited to a specific medium. Their vast range of applications and the utter complexity are what make their results so highly coveted. Because of this intricacy, it requires high-performance supercomputers to resolve approximate solutions. Nearly impossible to replicate in the laboratory or through field experiments, DNS enables researchers to numerically model turbulent motions natural in a fluid medium. To accurately isolate the results of varying parameters, we conducted 33 control experiments. In altering a single variable at a time, we determine not just the response, but the extent of the response. Three of the controlling variables were modeled from experiments conducted by Newman (2014), two of them were included from the algorithm created by Newman, and the last two were used to explore and optimize the wake signature.

E.   EXPERIMENTAL DESIGN

The original intent of this project was to further investigate the surface signatures of submerged bodies propagating in stratified fluids, specifically with bodies that are self-propelled. The addition of self-propulsion introduces momentum to the environment, which more closely models the true dynamic responses of a fluid medium perturbed by the propagating submerged body. In the initial stages of data analysis, we determined the investigation must be broadened to include the patterns and dynamics in the ocean interior. A comprehensive understanding of the effects at the air-sea interface is critical for fluid dynamic and operational oceanographic research. But with the increasing deployments of unmanned underwater vehicles, the ability to understand and detect internal disturbances is becoming rapidly imperative.

Our temporal scale is on the order of the inverse Brunt-Väisälä Frequency, Nt, or buoyancy period, which compares to 20 minutes. A number of studies have explored the effects in the near-wake ($Nt \ll 20$) and late-wake ($Nt > 20$), but we have chosen to

examine the intermediate-range wakes ($Nt \sim 20$) formed by the disturbance of our self-propagating submerged body. This range supports more probable detection period than that of the near or late wakes.

In analysis of the control-response relationships, we were able to create a non-dimensional algorithm that computes similar results to those of DNS with a fraction of the time and cost. Applying the algorithmic outcomes to a MATLAB database of world ocean sea surface temperatures, we were able to generate seasonal maps of expected sea surface temperatures (SSTs) seen when a SSB is propagating in the ocean interior.

THIS PAGE INTENTIONALLY LEFT BLANK

II.   MODEL DESCRIPTION

MITgcm was the model used to conduct the entire breadth of experiments for this study. It provides users a vast scope of numerical proficiencies to model and manipulate atmospheric and oceanic processes. Using the finite volume method, this numerical code solves the equations of motion that govern the environment. Its unique non-hydrostatic capability can compute both small and large scale phenomena (Adcroft et al. 2004). Given our study requires a comprehensive understanding of the ocean's governing equations, harnessing the ability to perturb fine-scale parameters, and view their responses on a much larger dimension, MITgcm proved ideal.

To run this complex series of experiments, equations with our inputs required nearly 500,000 central processing unit hours (33 experiments [with multiple runs] multiplied by 512 processors running for 24 hours each). Two supercomputers were utilized to run the model, analyze outputs, and store data. The primary computer is based in Mississippi at the Department of Defense High Performance Computing Modernization Program (HPCMP). The second computer is at the University of Texas at Austin's Advanced Computing Center (TACC).

MITgcm computes the Navier-Stokes equations for each grid space and time step that we determine and set in the model inputs. Though its primary mission lies with resolving large scale oceanic and atmospheric flows, flexibility exists in its domain to perturb the environment in a way that suits our research. In order to model a submerged body propagating in a fluid, we set inflow boundary conditions around an ellipsoidal volume of zero flow velocity. It mimics the identical responses as a moving body, but allows us to remain visually focused on the body and its intermediate-range disturbances.

The model grid used to conduct our experiments remains spatially constant in depth, z, but expands exponentially in longitude, x and latitude, y (Newman 2014). The idea is to fully resolve the wakes generated in the vicinity of the source and their vertical propagation yet conserve computational power and time with decreased resolution at the edges of the grid. The inputs set were $Nx = 2048$ steps in x with an initial delta dx_0 of 1.5

meter (m) increasing to dx_1 of 7.5 m. Similarly, in y, we used Ny = 64 steps with a dy_0 of 3.0 m increasing to dy_1 of 30 m. The grid remained undeviating in z, with a number of steps 200 and a dz of 0.5 m. Therefore, the dimensions of the experimental box are z depth of 100 meters, an x-zonal distance of nearly 7500 m and a y-zonal distance of approximately 730 m.

MITgcm enables the operator to prescribe boundary conditions that best suit the experiment. Since the grid exists to model conditions at the ocean surface and reach a depth of 100 meters, we selected a rigid lid to model the air-sea interface, and the no-slip conditions at depth z = 100 m to model a bottom that is continuous with its surroundings. In contrast, the eastern and western boundary conditions differ and fluctuate. We prescribe the inflow conditions on the western boundary for every run, specifically to input the uniform U = 10 m/s flow around the stationary submerged body. Orlanski open boundary conditions are used for the eastern boundary outflow to eliminate the possibility of disturbance interaction with the grid that could interfere with anticipated signatures (Orlanski 1976). Figure 2 depicts the setup of experiment.
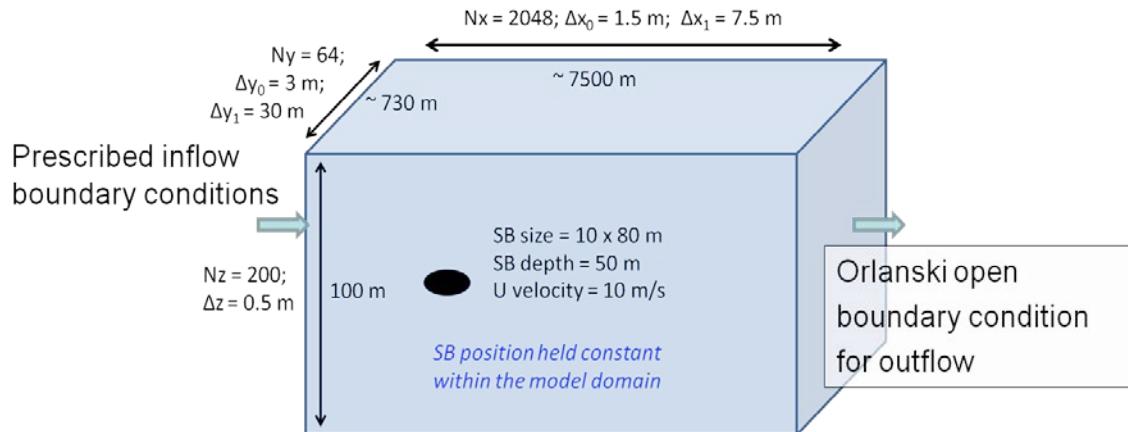
This box represents the model grid spacing, resolution, source parameters, and boundary conditions. Source: Newman (2014).

Figure 2.   Experimental Setup

The variables measured were surface and internal perturbations in temperature, T and internal velocity perturbations, U. Analysis of these parameters signify the relationship between the control parameter and the detection response. In MATLAB we were able to make millions of numerical outputs into visual and meaningful results. The common data analysis techniques were applied to the output, showing us direct correlations between the control and the response.

THIS PAGE INTENTIONALLY LEFT BLANK

III.   DIRECT NUMERICAL SIMULATIONS

The control experiments conducted to model the effects of propagating bodies include varying the same parameters as Newman (2014), with the inclusion of his algorithm parameters, as well as varying the size of the submerged body, and the introduction of excess momentum. The control parameters in this study are divided into environmental and source parameters, and are varied to demonstrate their respective effects on wake characteristics. Measurements of temperature perturbation signatures at the ocean surface and interior, as well as internal velocity variations, were made to determine parametric influences on wake dynamics. Modeling the SSB wake motions provides additional value to the detection problem. The control variables chosen for this research are buoyancy frequency, mixed layer depth, temperature gradient, source depth, source velocity, source size, and momentum excess.

Oceanic stratification is composed of the three environmental parameters, buoyancy frequency, N, mixed layer depth (MLD), and temperature gradient, $\partial T / \partial z$. The buoyancy frequency, formally known as the Brunt-Väisälä Frequency, is defined as a stability parameter, where $N = \sqrt[2]{-(\frac{g}{\rho_0})(\frac{\partial \rho}{\partial z})}$. When a parcel in the ocean is displaced vertically, the buoyancy frequency determines the rate at which said parcel will oscillate in an internal wave, and eventually return to its equilibrium. A square frequency of $1e^{-5}$ s^{-2} was determined as base value from which to vary. Much of the global ocean is represented by these stable values of N^2. The buoyancy frequency is largely dependent on density stratification which incorporates both temperature and salinity gradients. Average salinity values range from 34 to 36 practical salinity units (PSU) which is equivalent to 1 gram of sea salt per 1 kilogram of seawater. Mid-latitude temperature gradients in the upper ocean range from several degrees per hundred meters. Mixed layers are representative of regions where there is no temperature-salinity (T-S) gradient; where, rather, the layer is density-homogenous. The T-S profiles used in our study were derived from the *World Ocean Atlas 2013 (WOA13)* statistical and analyzed data fields for the mid-latitude Atlantic Ocean (Locarnini et al. 2013; Zweng et al. 2013). *WOA13* is

generated from the National Oceanographic Data Center's *World Ocean Database 2013 (WOD13)*, the largest database of oceanic observations (Boyer et al. 2013). Past studies have proved that the use of the World Ocean Atlas data fields are extremely valuable in understanding oceanic states and changes. For modeling purposes, however, they present some challenges. In order for the models to overcome the disparities in the fields, we created similar T-S profiles using smoothing techniques in MATLAB. These "synthetic" profiles represent the real world ocean and enable the supercomputers to calculate the complex momentum equations of motion, while including our desired stratification and a well-mixed layer. Examples of the profiles in the ocean are shown in Figure 3.
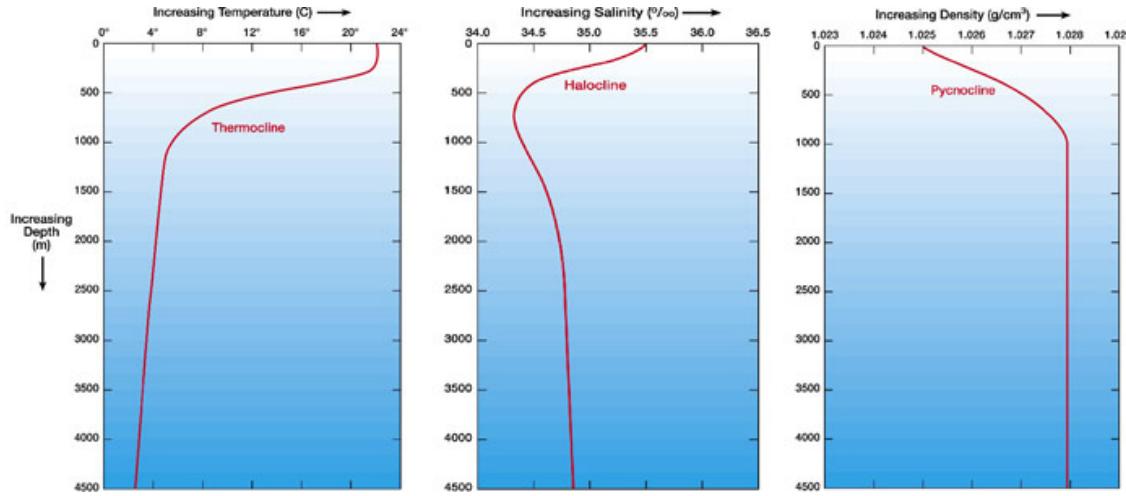
The profiles represent general temperatures, salinities and densities in the open ocean.

Figure 3.   Temperature, Salinity, and Density Profiles

Source velocity, *U*; sub depth, *H*; SB size, *L*; and momentum excess coefficient, *a*; all compose the source parameters. For naval relevance, we chose source velocities similar to those seen by submarines in the fleet, from 5 m/s to 15 m/s. These speeds also enabled us to use consistent code resolution throughout all the experiments. Depths from 10 m to 70 m were selected to portray a range of reasonable sub propagation depths, as well as to determine wake characteristics when SSBs transit in various environmental

14

regimes. We did have issues resolving the depths closes to the MLD, but our results still proved useful. Three submerged body sizes were chosen to demonstrate wake dynamics generated by various fluid displacements. The baseline SSB is proportional to many operational submarines in the oceans today.

The most important variable in this research is momentum excess coefficient. Momentum, put simply, is mass in motion. All fluids have mass, and their flow velocity is their motion. When forces are exerted on a fluid medium, the flow characteristics change, resulting in momentum differences. Even the momentum behind a towed body propagating at a constant velocity undergoes changes, as the fluid vorticity creates wakes that interact. The introduction of self-propulsion, however, further complicates the momentum wakes induced behind the submersible. To simulate propulsion, a volume of excess momentum was inserted in the grid space behind the submerged body. At each time step, the model measured the drag force on the front of the SSB, calculated the Navier-Stokes equations with the adjusted momentum, and inserted this momentum change into the volume as a thrust force. By counterbalancing the thrust and drag forces, we created a zero net momentum, self-propelled SSB (Voropayev and Smirnov 2003). The variation of our momentum excess parameter, a, ranges from -1.0 to 2.0, to model towed and self-propelled submarine propagation.

In order to determine the environmental responses induced from variations in control parameters, and the subsequent control-response relationship, we conducted an extensive data analysis. Our focus rested at the surface of the ocean for a majority of the study. It was not until we questioned particular results that we broadened our concentration and became curious about the interior.

A.   VARYING BUOYANCY FREQUENCY

The Brunt-Väisälä Frequency was varied in the DNS production runs in a series of five values that range from $N^2 = 5e^{-6}$ to $4e^{-5}$ s^{-2}. The median value of $1e^{-5}$ s^{-2} represents the buoyancy frequency found in a majority of the world's oceans. Variations around this base value provide insight into how temperature and velocity perturbations propagate in more and less stably stratified regimes. The buoyancy frequency is subject to changes in

potential density with depth as well as the acceleration of gravity. Since our study focuses on the upper 100 m of the ocean, we recognize only the gradients in density, neglecting changes in gravity. Higher frequencies are representative of more stably stratified regimes, where lower frequency domains represent those with less stratification and therefore, less stability. A larger N^2 will dampen the wake oscillations much faster than a small value. Similarly, less stable regions will display more turbulent motions. Knowing this, we proceed to our dynamic responses with respect to changes in the buoyancy frequency, N^2.

1.   Impact on Thermal Surface Signatures and Extent

The baseline buoyancy frequency, which closely matches the frequency representative of the mid-latitude ocean, generates the largest maximum change in surface temperature. As the Brunt- Väisälä frequency increases greater than the baseline value, the surface signature greatly decreases, as seen in Figure 4. A stable water column is necessary for oscillatory motion to propagate a wake. If the medium is unstable or less stable, the turbulent motions dissipate the energy, and the signature is less significant. More stability presents opportunity for wakes to transfer water properties away from the focal point. After a particular stability, however, the restoring force is strong enough that it dampens the energy propagation. The buoyancy frequency for the greatest signature in this study is the baseline value of $1e\text{-}5s^{-2}$.
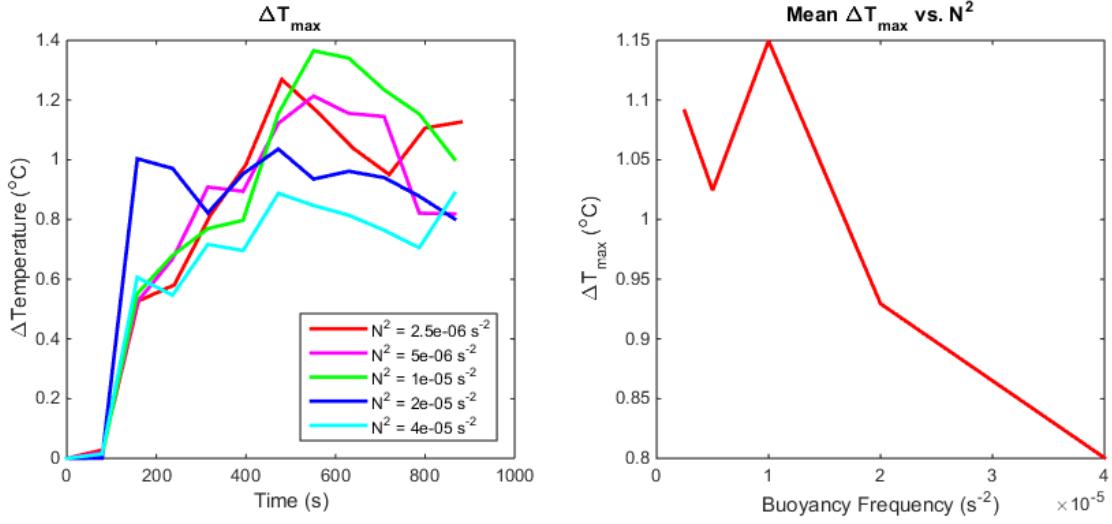
Time series of ΔT_{max} while varying N^2 (left). Relationship of mean ΔT_{max} and N^2 (right).

Figure 4.   Thermal Surface Signature

Temperature perturbations that reach the air-sea interface can be detected by remote sensing capabilities. For the baseline conditions, a temperature perturbation of nearly 1.4°C reached the surface and persisted for almost 7 kilometers. Figure 5 portrays this revolutionary finding for wake detection.
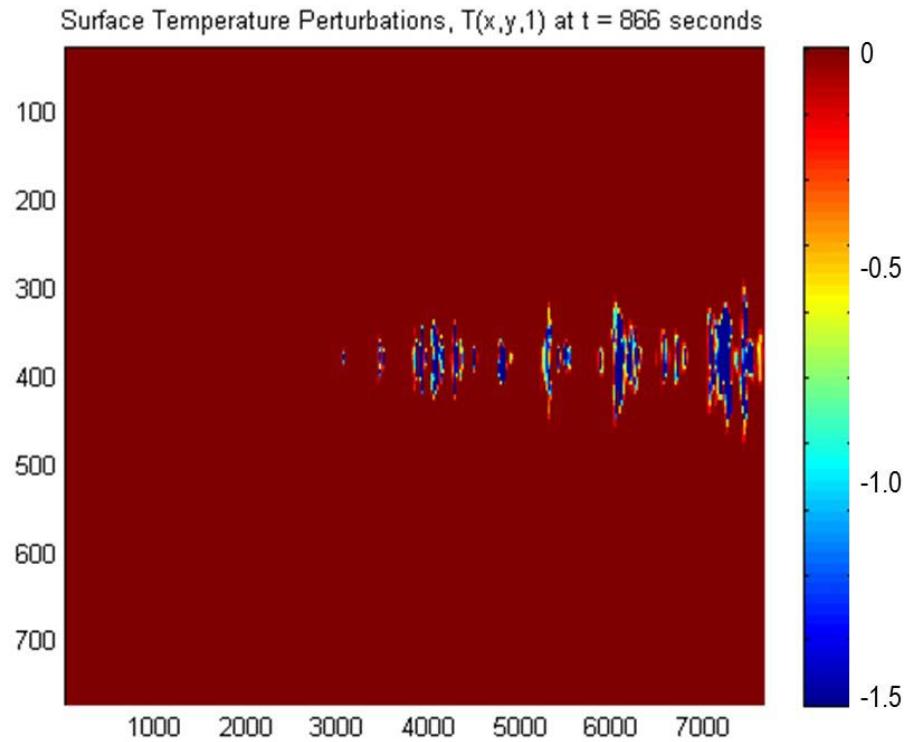
Surface cross-section of thermal signature generated from submerged body propagating with baseline conditions, $N^2 = 1e^{-5}s^{-2}$ at t = 880s. The blue values yield temperature changes below -1.0 °C.

Figure 5.   Surface Temperature Perturbations

It is equally as important to investigate the surface area of the thermal signature as the signature itself. The maximum surface area of the thermal response is approximately 63,000 square meters (m^2), and the maximum mean signature is just under 50,000 m^2, shown in Figure 6. The extent of the signature decreases linearly with increasing buoyancy frequency. An increased stratification dampens the spatial extent of the response, similar to the effect it has on the magnitude of the thermal signature.
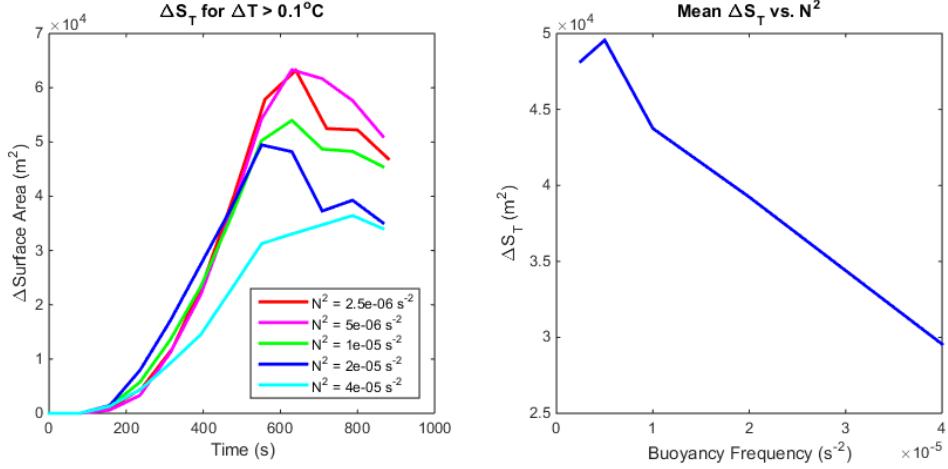
Time series of ΔS_T while varying N^2 (left). Relationship of mean ΔS_T and N^2 (right).

Figure 6.   Areal Extent of Thermal Surface Signature

Internal wake signatures show an increased temperature perturbation near the mixed layer depth. The region where the mixed layer and the thermocline interact, severely impacts the temperature signatures at the surface as the energy is advected both to the surface and the depths. Figure 7 demonstrates the internal variations of temperature when the submerged body propagates through the stratified medium.
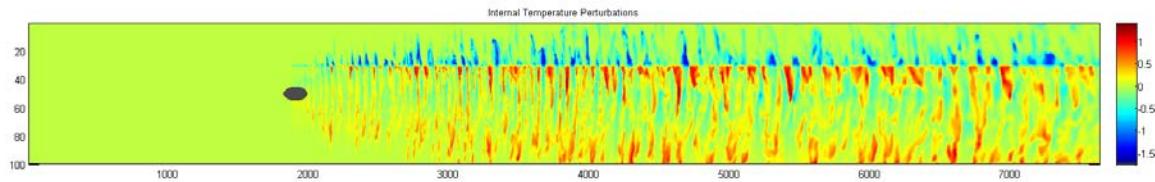
Internal cross-section of temperature perturbations generated from submerged body propagating with baseline conditions, $N^2 = 1e^{-5}s^{-2}$, at t = 880s.

Figure 7.   Internal Temperature Perturbations

19

2.   Impact on Temperature Perturbations in the Interior

The snapshots of the perturbations in depth for each buoyancy frequency are taken at the end of the model run to allow for wakes to propagate fully. As depicted in Figure 8, each of the root mean square (RMS) temperature perturbations follow a similar pattern with increasing depth. There exists a prominent, initial slope from the surface to the mixed layer depth, a jagged interruption where wakes perturb the upper thermocline, followed by a decreasing temperature difference with depth. Though mean RMS temperature values are close respectively, there is a slight decreasing trend in the interior temperature perturbations with respect to frequency increases. Essentially, the more stable the medium, the more damped the perturbation will be.
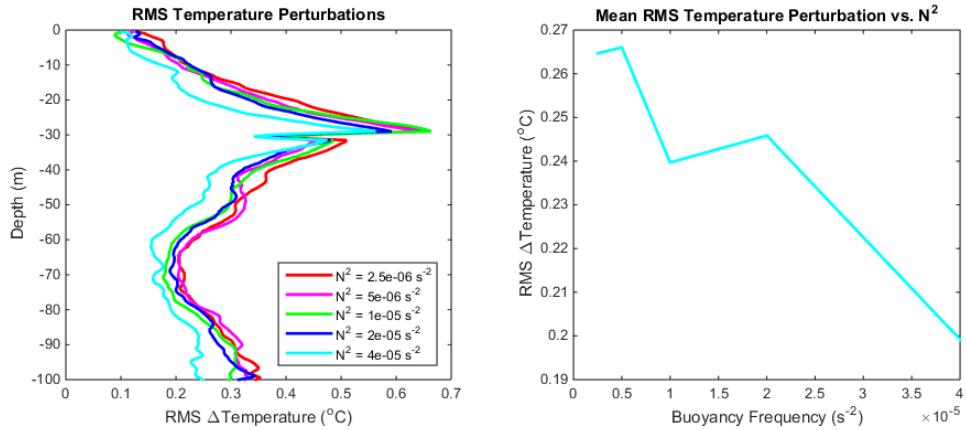
RMS temperature perturbations in depth, z, while varying N^2 (left). Relationship of mean RMS temperature perturbation and N^2 (right).

Figure 8.   Internal RMS Temperature Perturbations

The RMS plots help to reveal the signature against the background values. In the interior, positive and negative temperatures are advected, both to the surface and to the depths of the experimental grid space. By removing the temperature signs, we visualize the magnitude of the perturbation. Whether positive or negative, the RMS values yield a more representative image of the mean interior signatures over time. In Figure 9, all buoyancy frequencies maintain an increasing temperature change in signal time until they

plateau around t = 900s. And as the N^2 values increase, there exists a declining trend in mean RMS temperature perturbations.
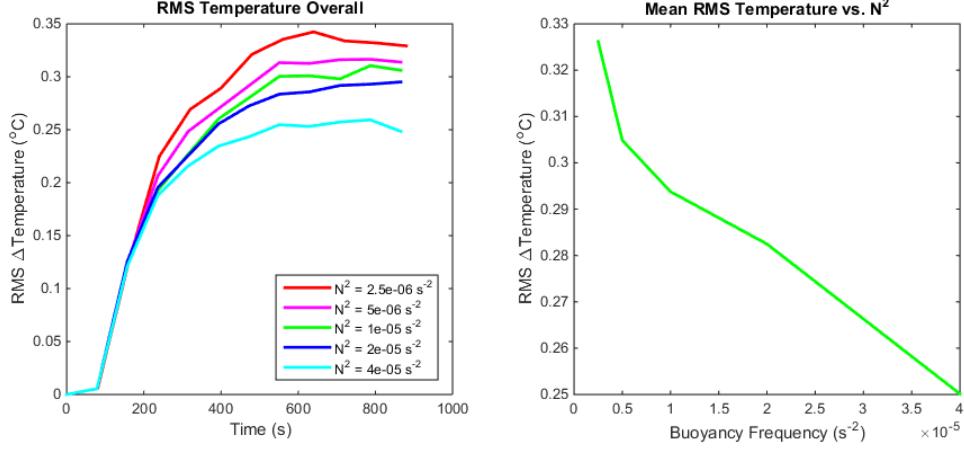
RMS temperature perturbations while varying N^2 (left). Relationship of mean RMS temperature perturbation and N^2 (right).

Figure 9.   Overall Internal RMS Temperature Perturbations

3.   Impact on Velocity Perturbations in the Interior

Similar to the internal temperature perturbation plots, the RMS velocity perturbations represent a snapshot in time of the N^2 related interior changes in velocity. As expected, a wake signature in the positive x direction (behind the submerged body) exists with two smaller wake peaks toward the surface and depths, respectively. This velocity signature is comparable to de Stadler and Sarkar (2011), a study noting the internal velocity flow responses behind an ellipsoid propagating in a stratified medium. It is similar throughout our study, with slight changes specific to varying parameters. With buoyancy frequency as the parameter varied in this experiment set, we notice a slightly intensified peak velocity perturbation with the greatest N^2 value at 50 m depth following the body. The average RMS values plotted with respect to N^2 however are less clear. The velocity perturbation differences are so small that the plot in Figure 10 is almost inconclusive.
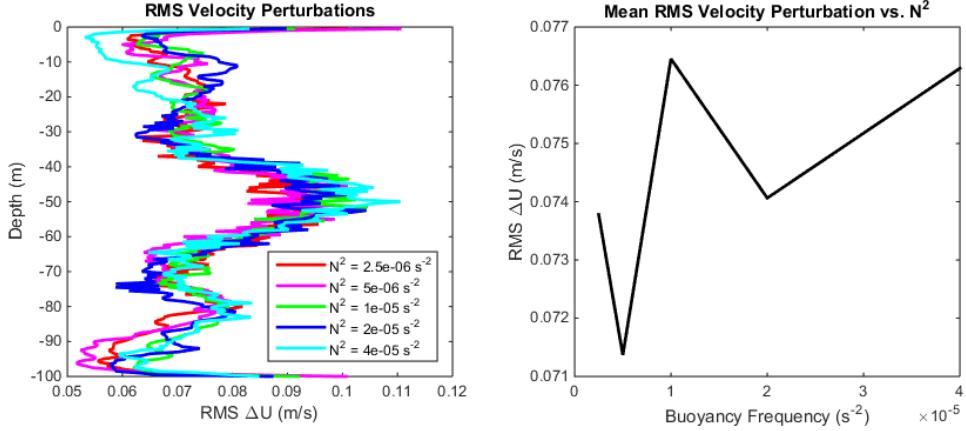
RMS velocity perturbations in depth, z, while varying N^2 (left). Relationship of mean RMS velocity perturbation and N^2 (right).

Figure 10.   Internal RMS Velocity Perturbations

An overall RMS velocity image is plotted in Figure 11 to display the increasing changes in the interior over time. Again, we notice a trend of increasing velocity perturbations in time with a plateau toward the end of the run, and less conclusive signature differences due to varying N^2 values.
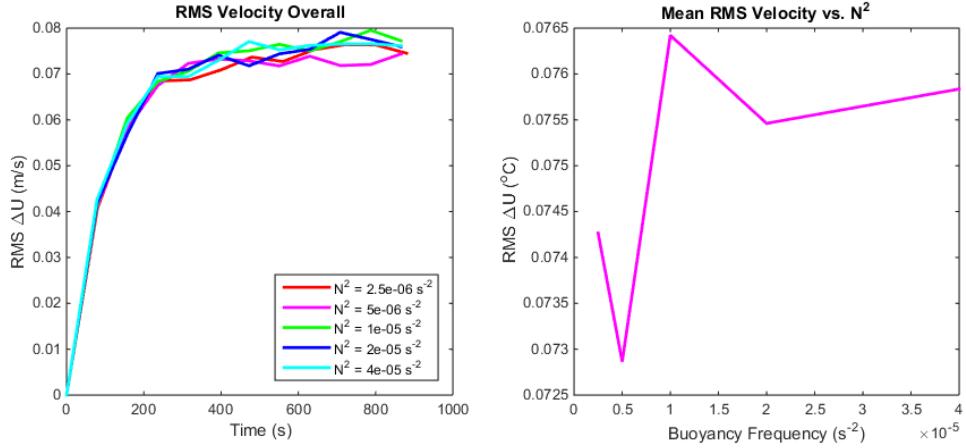
RMS velocity perturbations while varying N^2 (left). Relationship of mean RMS velocity perturbation and N^2 (right).

Figure 11.   Overall Internal RMS Velocity Perturbations

22

B.   VARYING MIXED LAYER DEPTH

A mixed layer is the layer in depth from the ocean's surface that is composed of uniform properties of temperature, salinity, and velocity flows. Layer homogenization can stem from temperature fluctuations by day, season, and location, salinity changes, and turbulent oceanic mixing in the form of currents and waves. The mixed layer depth marks the bottom of that layer, and it varies based on the properties above. The reference temperature-salinity profiles in Figure 12 denote the baseline MLD of 30 m. Variations in both properties cause abrupt changes in density and generate a pycnocline. As noted in the buoyancy frequency analysis, the pycnocline plays a large role in wake signatures at the surface and interior. Similarly, the mixed layer depth will result in considerable impacts on wake dynamics.

The MLDs in the experiments were varied, a span of five depths, from 1 m to 40 m. A 1 m MLD essentially marks a region where a temperature and salinity gradient exist throughout the column of water. Broadly speaking, the shallowest mixed layers reside in the equatorial region, with an increasing depth by latitude, and a profound MLD at the poles. Correspondingly, the deepest MLDs exist in the winter and the shallowest in the summer. We hypothesized that as the mixed layer deepens, because of its homogeneity, the response to the surface will decrease. As the initial disturbances around the SSB propagate, there will be less thermal gradient to advect to the air-ocean interface. The signatures in the interior, we suspected, would be much different.
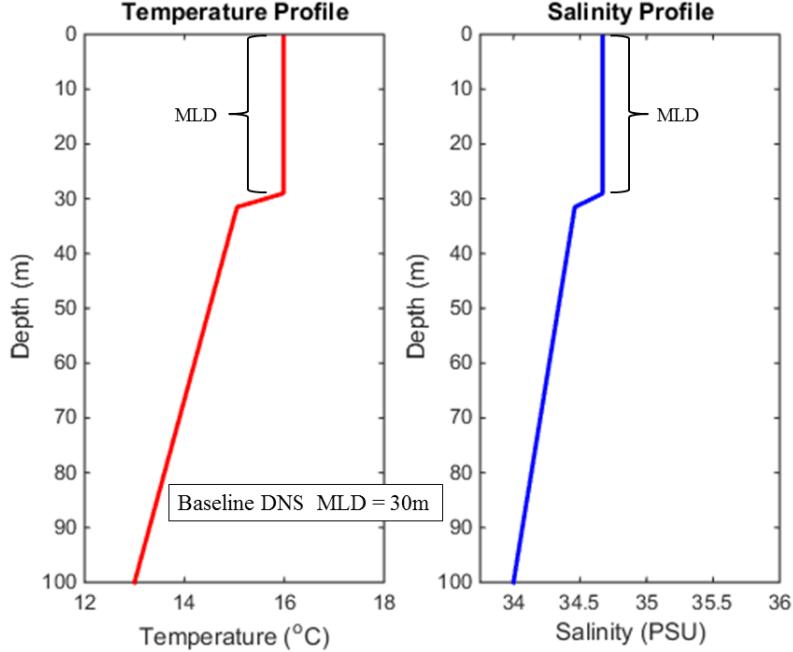
Baseline T-S profiles generated using *WOA13* data and MATLAB code.

Figure 12.   Reference Temperature and Salinity Profiles with Mixed Layer

1.   Impact on Thermal Surface Signature and Extent

It is apparent in Figure 13 that the temperature perturbations vary with changes in mixed layer depths, and a declining trend is observed where the MLD is increased. The first mixed layer depth of 1 m is indicative of a well-stratified column with the exception of the top three feet of the ocean. With this stratification in both temperature and salinity, we expect a distinct surface temperature perturbation for the submerged body operating at baseline depth, as there are 50 m of varying properties to advect to the surface. As the MLD increases, less of the stratified medium is perturbed. There is visual proof of this decrease in temperature change as the depth of the MLD increases.
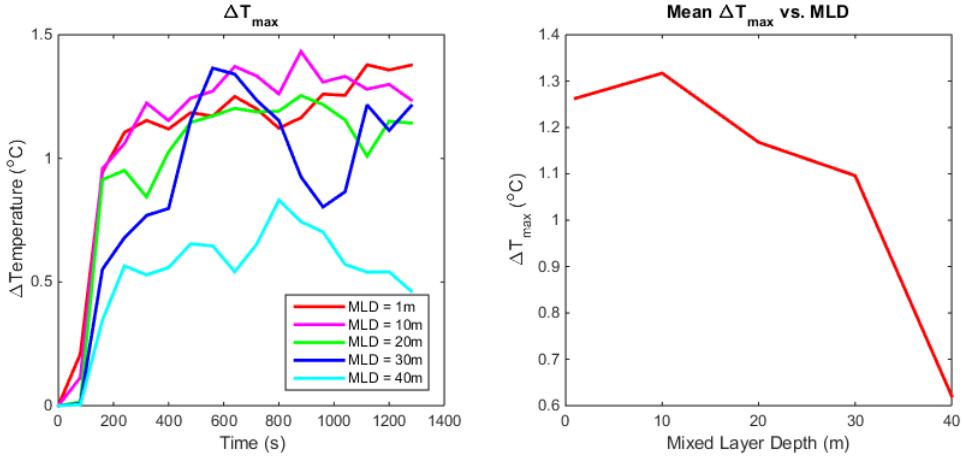
Time series of ΔT_{max} while varying MLD (left). Relationship of ΔT_{max} and MLD (right).

Figure 13.   Thermal Surface Signature

The slope of the areal extent of the surface area temperature change is even more noticeable as MLD is increased in Figure 14. The loss of density gradient significantly dampens the extent of the change reaching the air-sea interface.
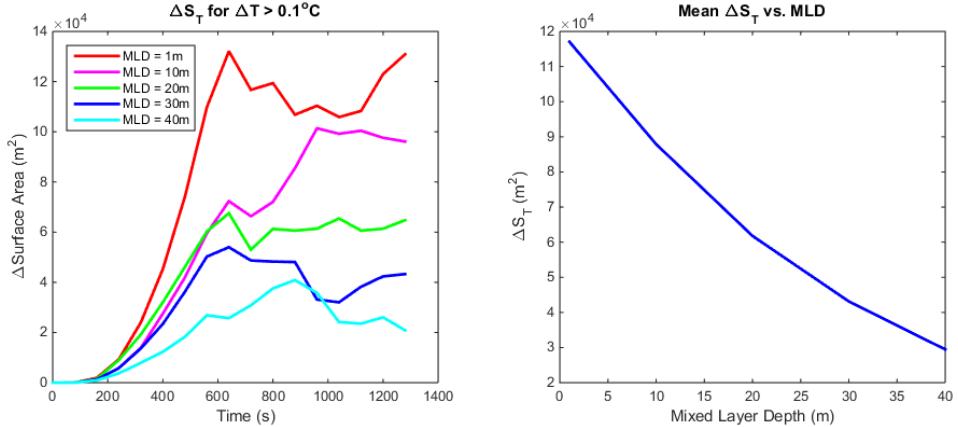
Time series of ΔS_T while varying MLD (left). Relationship of ΔS_T and MLD (right).

Figure 14.   Areal Extent of Thermal Surface Signature

2. Impact on Temperature Perturbations in the Interior

The internal signatures yielded quite fascinating results. The closer in proximity the MLD and submerged body were, the more distinct the internal disturbance is, in Figure 15. While the surface signature decreased with increasing MLD, the opposite occurs internally. The MLD-submersible depth relationship is important, and was overlooked until graphing these quantities. This finding sparked profound interest in the internal signatures and patterns of the study.
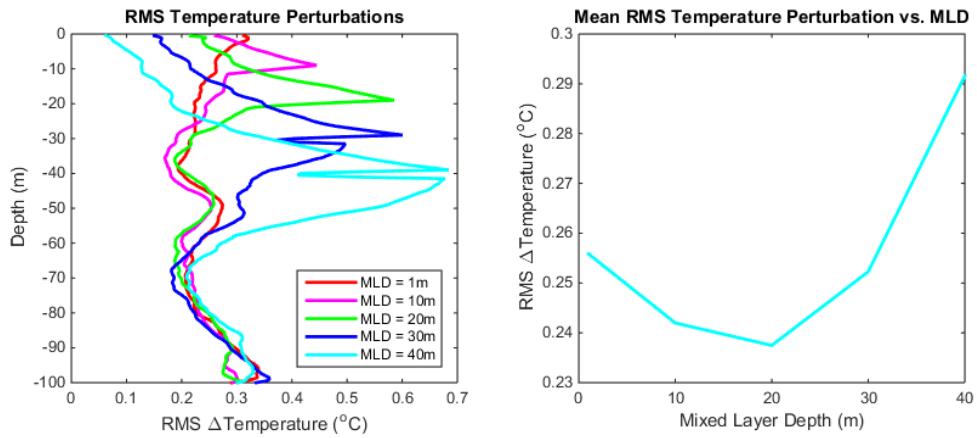
RMS temperature perturbations in depth, z, while varying MLD (left). Relationship of RMS temperature perturbation and MLD (right).

Figure 15.   Internal RMS Temperature Perturbations

Again, the RMS snapshot at the end of the model run above differs from the overall RMS plot in Figure 16. The overall figure more fully depicts the true trend that may not be gathered by one image in time. It is even more clearly observed that the internal temperature signature increases with reduced proximity of the MLD and propagating body.
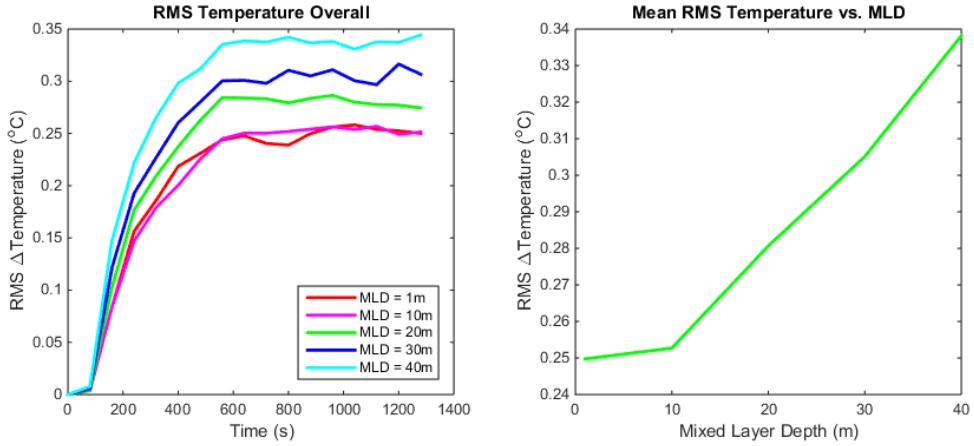
26

RMS temperature perturbations while varying MLD (left). Relationship of RMS temperature perturbation and MLD (right).

Figure 16.   Overall Internal RMS Temperature Perturbations

3.   Impact on Velocity Perturbations in the Interior

Less certain are the internal velocity perturbation signatures. The difference in RMS values of velocity changes versus depth are so small that no pattern is discerned in Figure 17.
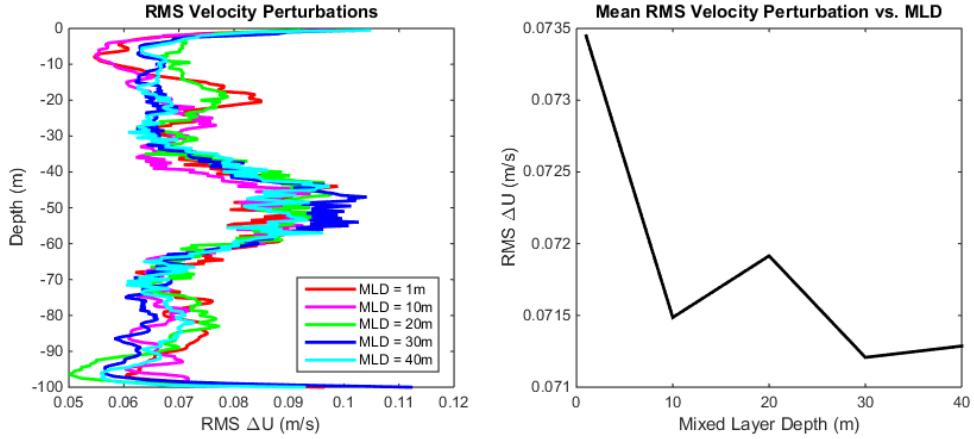
RMS velocity perturbations in depth, z, while varying MLD (left). Relationship of RMS velocity perturbation and MLD (right).

Figure 17.   Internal RMS Velocity Perturbations

The changes in the RMS velocity deltas are so insignificant that again, no trend is recognized. The left plot in Figure 18, indicates, however, a noticeable increase in RMS velocity change over time followed by an immediate plateau.
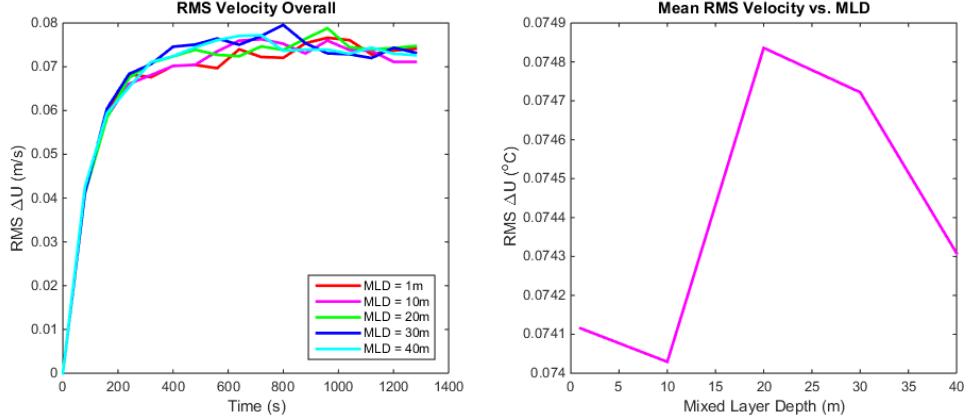
RMS velocity perturbations while varying MLD (left). Relationship of RMS velocity perturbation and MLD (right).

Figure 18.   Overall Internal RMS Velocity Perturbations

C.   VARYING TEMPERATURE GRADIENT

Temperature gradients generally exist below the MLD, but in the case of a well-mixed ocean, they can occur immediately under the surface. In this study, the temperature gradients, $\partial T/\partial z$, occur below the baseline MLD value of 30 m, and range from -0.01°C/m to -0.05°C/m. Keeping all other parameters constant, it becomes apparent how dynamic the surface and internal temperature perturbations from the varying $\partial T/\partial z$ are. Near linear responses are observed when the temperature gradient is increased. As with the parameters above, the impacts of the interior velocity signatures with varying temperature gradient are less conclusive.
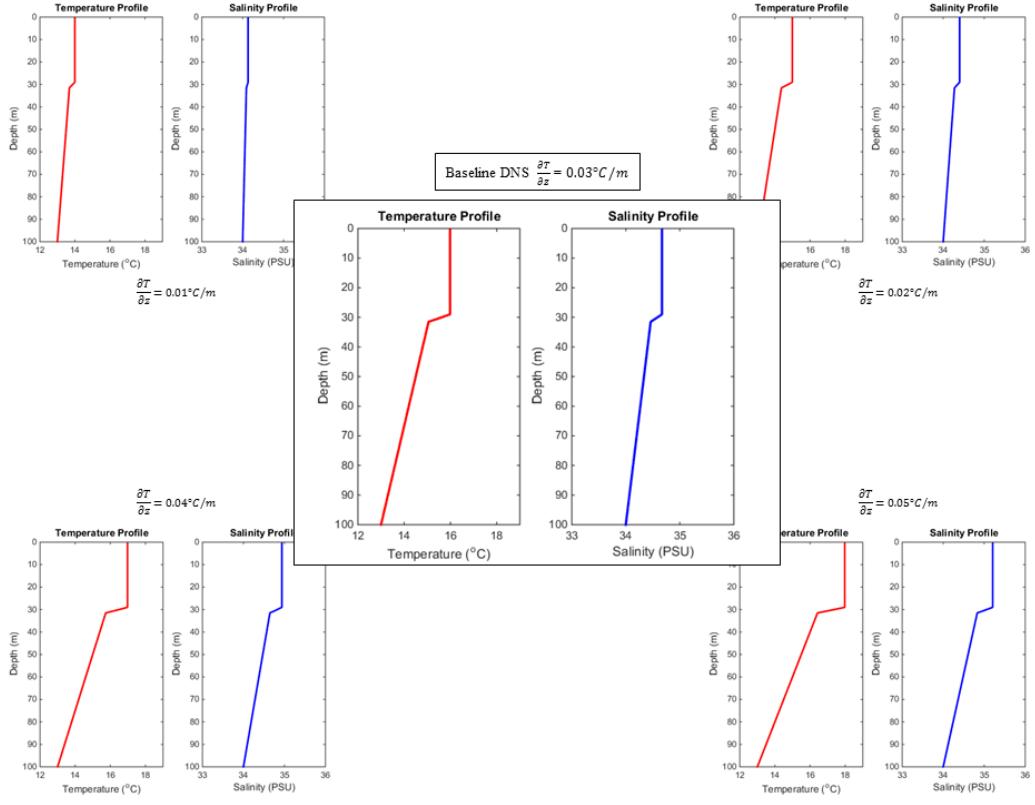
The baseline experiment is centered above with the other four gradients on each corner.

Figure 19.   T-S Profiles Generated from Variations in $\partial T/\partial z$

1.   Impact on Thermal Surface Signature and Extent

With a baseline value of 30 m MLD, we expect the temperature perturbations near the submerged body to penetrate and propagate through the top 30 m of mixed ocean. A well-stratified column below the mixed layer will induce increased temperature perturbations to be transported to the surface. Both images, Figure 20 and Figure 21, illustrate this concept well.
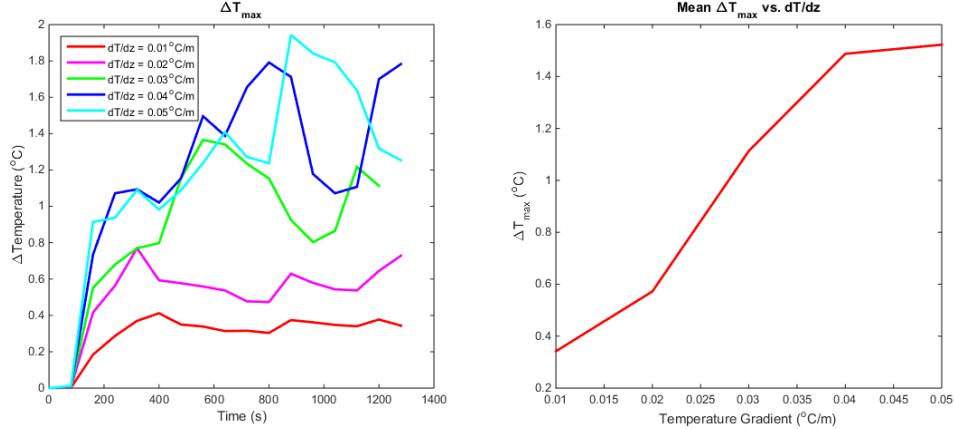
Time series of ΔT_{max} while varying $\partial T/\partial z$ (left). Relationship of ΔT_{max} and $\partial T/\partial z$ (right).

Figure 20.   Thermal Surface Signature

Similar to the image above, we notice Figure 21 depicts the correlation of the areal extent of the signature to the trend of the signature itself. An increase in the change in temperature at the surface will correspondingly increase the extent of said signature.
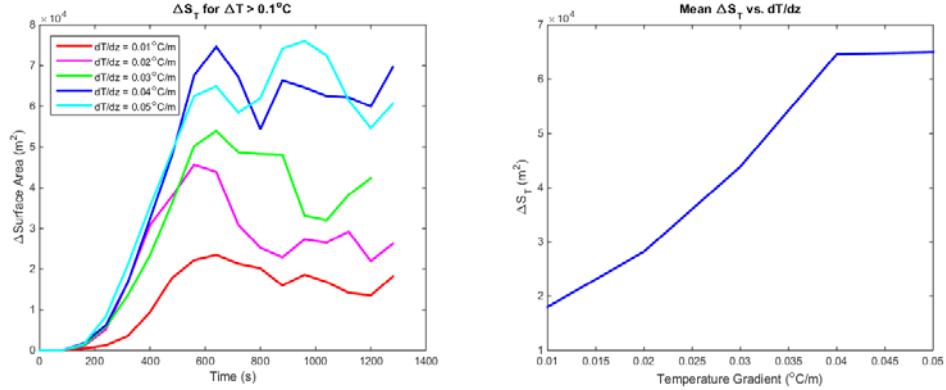
Time series of ΔS_T while varying $\partial T/\partial z$ (left). Relationship of ΔS_T and $\partial T/\partial z$ (right).

Figure 21.   Areal Extent of Thermal Surface Signature

30

2. Impact on Temperature Perturbations in the Interior

The distinction between each of the internal signatures in Figure 22 is noteworthy. Significant temperature differences in the interior are evident as the stratification is increased. The mixed layer depth marks the location of the most drastic signature perturbation as well as the two wave peaks, which advect temperatures both to the surface and to the depths.
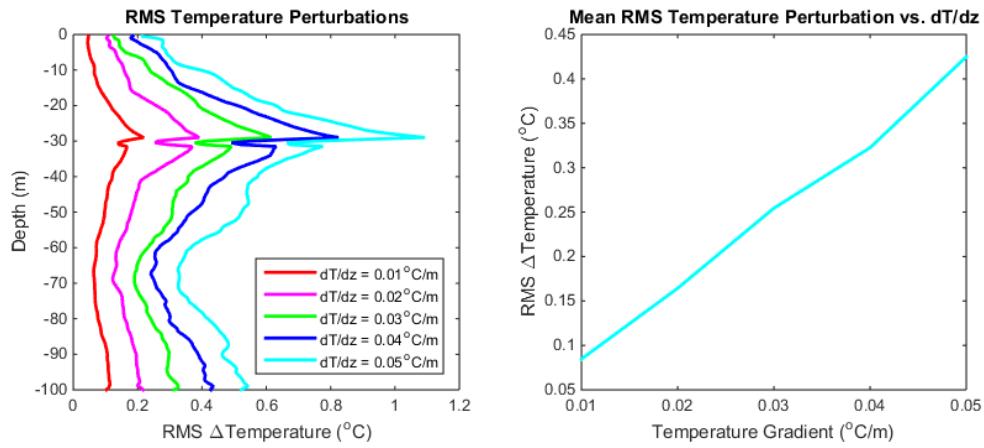
RMS temperature perturbations in depth, z, while varying $\partial T/\partial z$ (left). Relationship of RMS temperature perturbation and $\partial T/\partial z$ (right).

Figure 22.   Internal RMS Temperature Perturbations

Just as obvious are the overall internal RMS temperature values in Figure 23. Less variation in perturbation exists over time as it did in previous experiments.
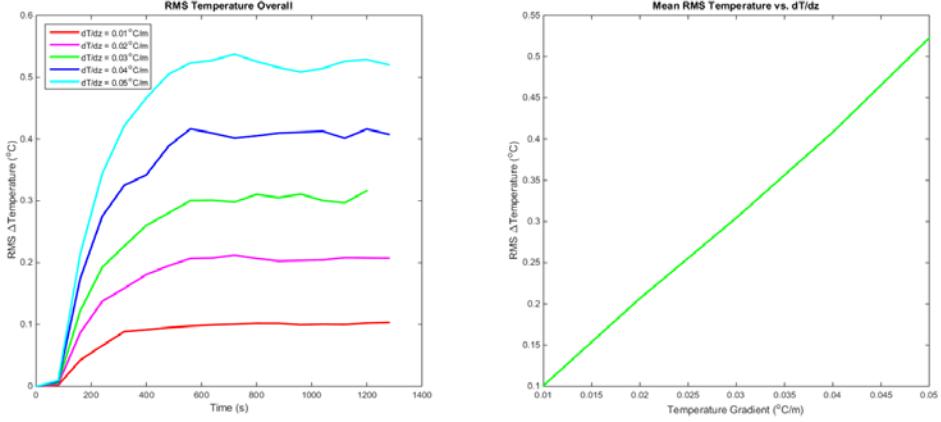
RMS temperature perturbations while varying $\partial T/\partial z$ (left). Relationship of RMS temperature perturbation and $\partial T/\partial z$ (right).

Figure 23.   Overall Internal RMS Temperature Perturbations

3.   Impact on Velocity Perturbations in the Interior

Velocity differences, we find, are not as variant as temperature when modifying the thermal properties of the model runs. The velocity wave signature occurs, but no pattern is realized, particularly in the right-hand plot of Figure 24.
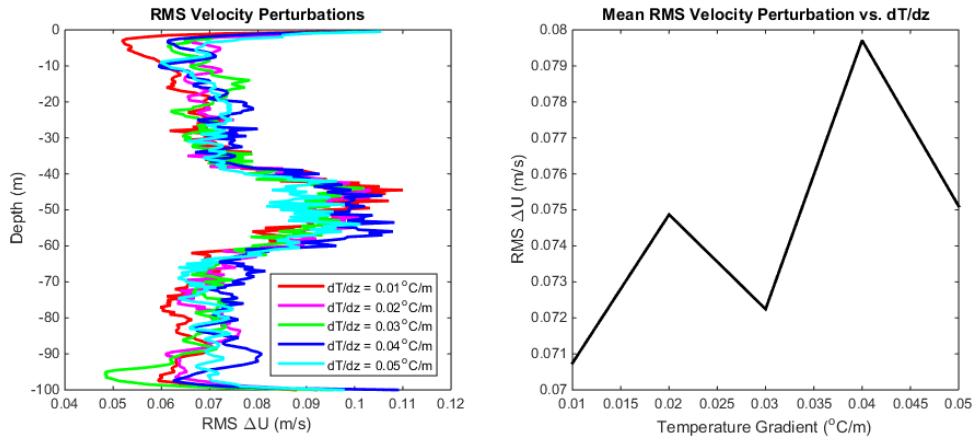
RMS velocity perturbations in depth, z, while varying $\partial T/\partial z$ (left). Relationship of RMS velocity perturbation and $\partial T/\partial z$ (right).

Figure 24.   Internal RMS Velocity Perturbations

The overall RMS velocity perturbation represented in Figure 25 does not portray any more of a trend than the values at the end of the run. We hypothesize that in the following experiment, however, a velocity pattern will transpire.
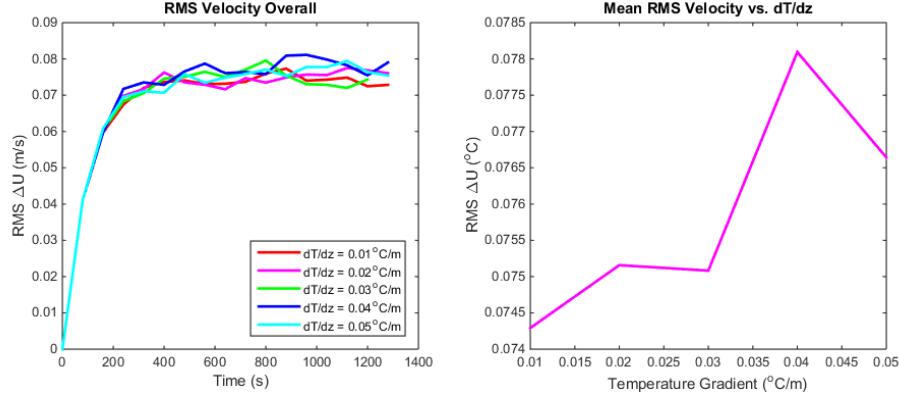
RMS velocity perturbations while varying $\partial T/\partial z$ (left). Relationship of RMS velocity perturbation and $\partial T/\partial z$ (right).

Figure 25.   Overall Internal RMS Velocity Perturbations

D.   VARYING SOURCE VELOCITY

Variations in the submerged body velocity are an important addition to other studies. Realistically, submerged bodies, like their environment, are dynamic. Understanding how changes in their motion modify the surrounding medium is pivotal in fluid mechanics as well as to the operator. A series of source velocities from 5 to 15 meters per second (m/s) was tested to determine the resultant surface and internal signatures. Again, the baseline run of 10 m/s was executed to provide a reference, as shown in Figure 26. The first thing to note is the timing of the temperature response. The slower flow velocities presented much smoother plots as well as higher resolution, two-dimensional images. The higher velocity runs peaked at the surface earlier but their responses subsequently decayed much faster.

33

Like the temperature responses in the temperature gradient runs, the velocity responses in this series of experiments were most profound. A significant demarcation in the internal signals denotes a linear increase in velocity perturbation versus flow.
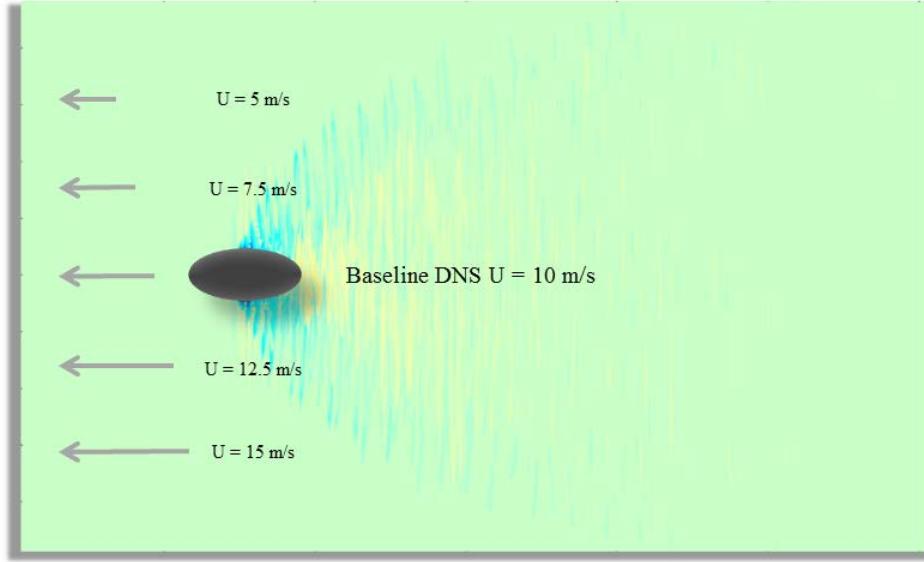
The experimental values of zonal velocity were varied around the baseline value.

Figure 26.   DNS Variations in Zonal Velocity, U

1.   Impact on Thermal Surface Signature and Extent

Analogous to the inconclusive results obtained when determining velocity signatures from temperature changes, Figure 27, which depicts the temperature perturbations in the velocity varying experiments, yields uncertain trends. Of note, the timing of the initial surface signature differs with increasing SB velocities, as expected.
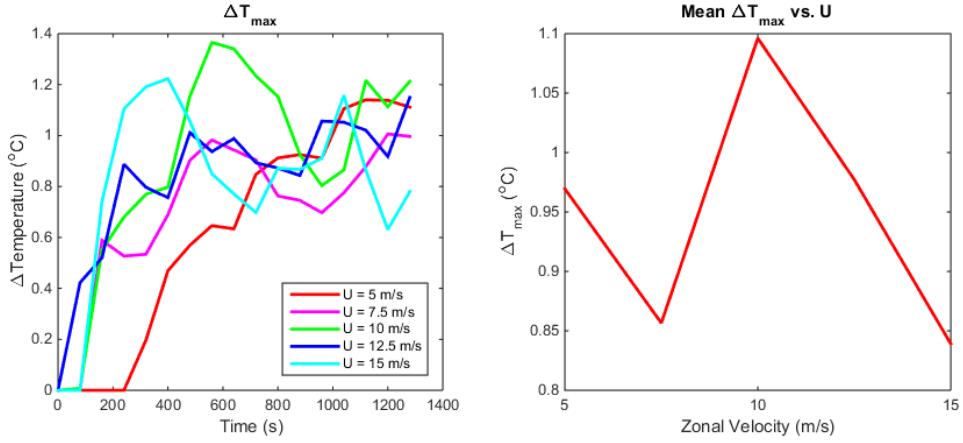
Time series of ΔT_{max} while varying U (left). Relationship of ΔT_{max} and U (right).

Figure 27.   Thermal Surface Signature

The extent of the signatures was interesting. The slowest and fastest experimental speeds resulted in the smallest surface area extent, where the velocities around baseline value of $U = 10$ m/s delivered greater area, as seen in Figure 28.
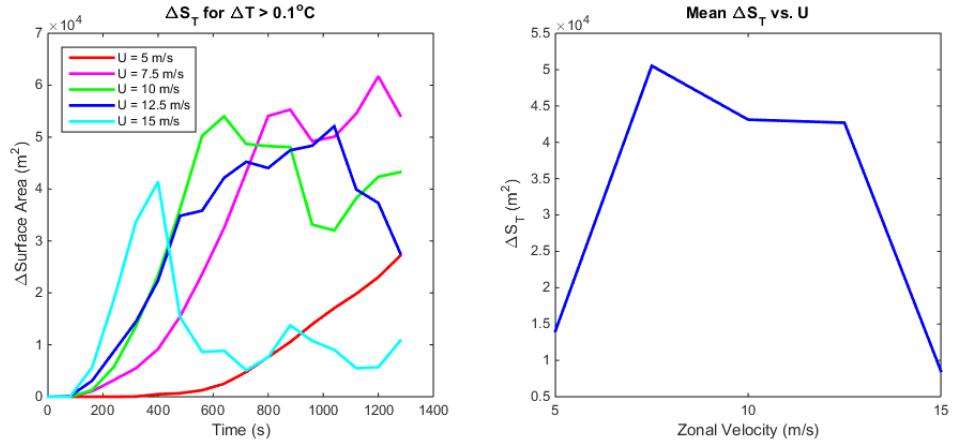
Time series of ΔS_T while varying U (left). Relationship of ΔS_T and U (right).

Figure 28.   Areal Extent of Thermal Surface Signature

2. Impact on Temperature Perturbations in the Interior

Figure 29 illustrates how the fastest sub velocity caused the greatest temperature perturbation internally, though the differences were minor. The largest temperature jump was again at the MLD, and the 15 m/s velocity quite noticeably distinguishes itself by nearly 0.2°C ΔT_{RMS} greater than the other speeds.
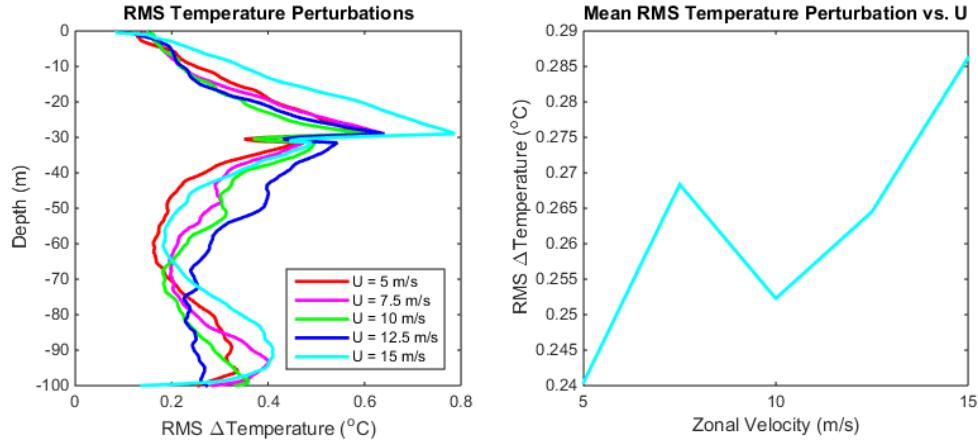
RMS temperature perturbations in depth, z, while varying U (left). Relationship of RMS temperature perturbation and U (right).

Figure 29.   Internal RMS Temperature Perturbations

The overall internal RMS temperature signatures are more convincing that the changes in *U* velocity do in fact play a role in the interior. Not only do the signatures propagate from the sub more quickly with increasing *U* values, but for this study's model run time, the faster speeds transported a relatively greater temperature variation internally. Figure 30 depicts the overall mean variations well.
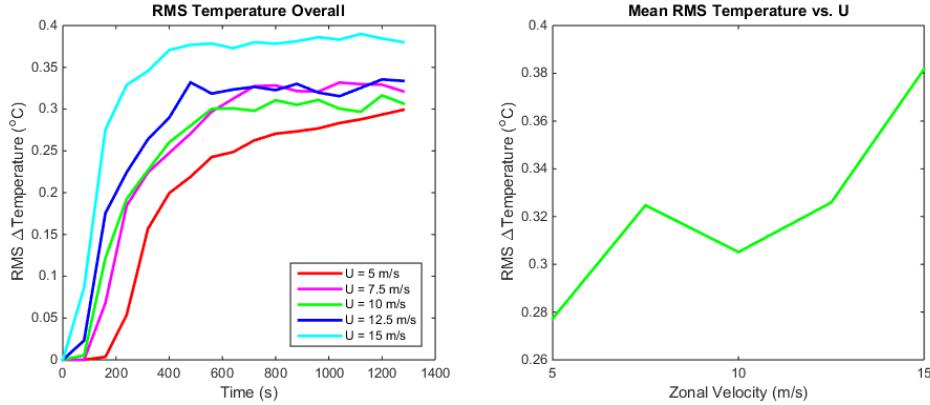
RMS temperature perturbations while varying U (left). Relationship of RMS temperature perturbation and U (right).

Figure 30.   Overall Internal RMS Temperature Perturbations

3.   Impact on Velocity Perturbations in the Interior

The representation in Figure 31 of the experimental velocity variation to the perturbation velocity results in a definitive relationship. While the internal pattern of ΔU remain, the 0.6 m/s RMS change from $U = 5$ m/s to $U = 15$ m/s is rather remarkable. The largest changes in velocity perturbation exist directly following the submerged body at the baseline depth of 50 m.
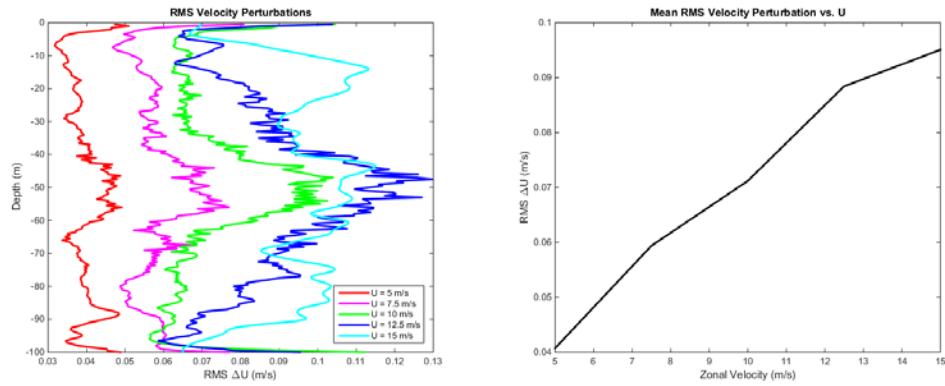
RMS velocity perturbations in depth, z, while varying U (left). Relationship of RMS velocity perturbation and U (right).

Figure 31.   Internal RMS Velocity Perturbations

The overall signatures in Figure 32 are just as definitive, noting that the trend exists for all time, not merely at the end of the experimental run.
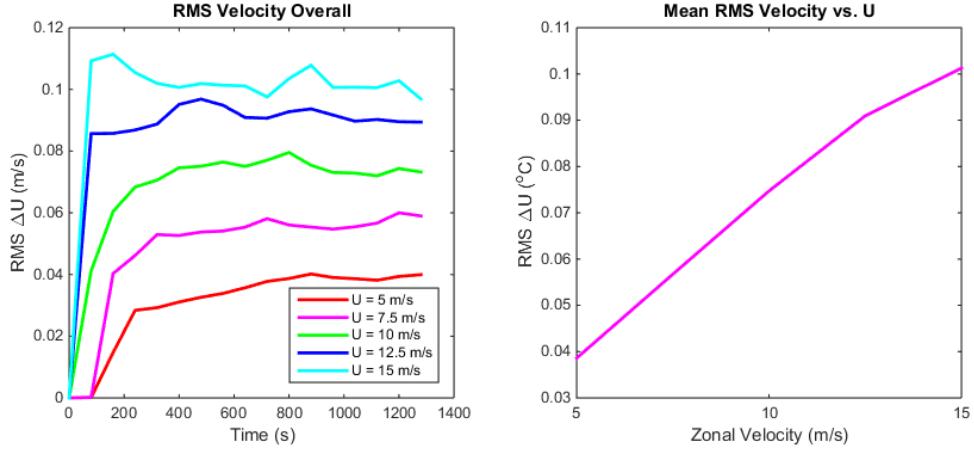
RMS velocity perturbations while varying U (left). Relationship of RMS velocity perturbation and U (right).

Figure 32.   Overall Internal RMS Velocity Perturbations

E.   VARYING SOURCE DEPTH

The concept of source depth variance is extremely operational. In fact, it is highly unlikely a submersible would maneuver at the same depth for an extensive period of time. Bathymetry, environmental conditions, and of course operational demands cause the body to alter course and change depth. The proximity of the SB to the unique oceanic properties of temperature and salinity will have the most notable findings in this research. Due to the nature of the model computations and resolution, when running the depths of 30 m and 40 m, where the MLD existed, the model runs blew up. It was not until after the experimentation was complete that changes in viscosity were made to better resolve the quantities around the mixed layer depth. In the findings, we discovered that even in the shallowest depths, a better model resolution for those runs would have more clearly determined the internal patterns of the wake and signatures. Figure 33 represents the experiments varying source depth.

38
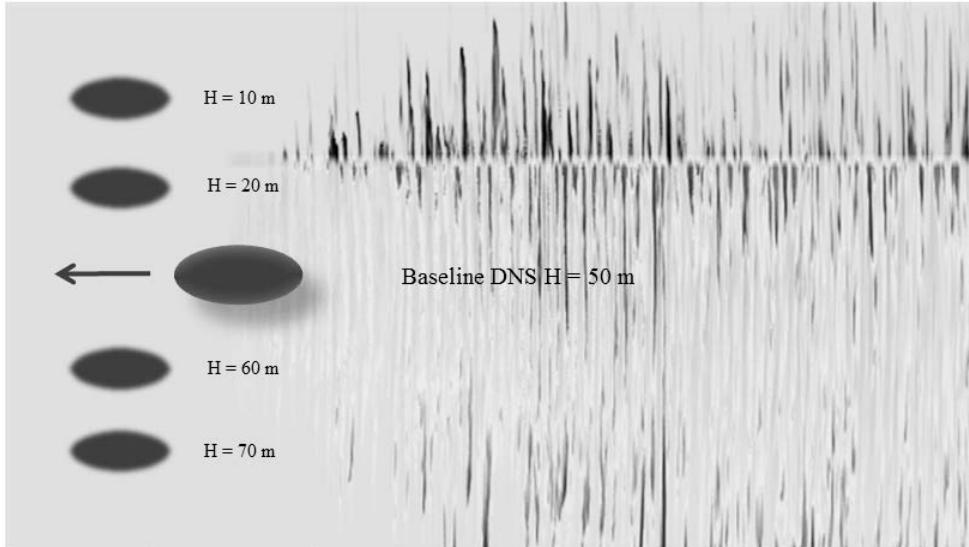
Depths of 10, 20, 50, 60, 70 meters were used for these experimental runs.

Figure 33.   DNS Variations in Source Depth, *H*

1.   Impact on Thermal Surface Signature and Extent

When the submerged body propagates within the mixed layer, there is little chance for temperature perturbations to penetrate the layer below. As soon as the source depth is in the stratified or gradient layer, the opportunity exists for the gradient properties to be transported to the surface. The further the distance from the surface, however, the smaller the signatures will be, as seen in Figure 34. We suspected a bell-shaped curve for the second plot, should the 30 m and 40 m runs have been completed for this study.
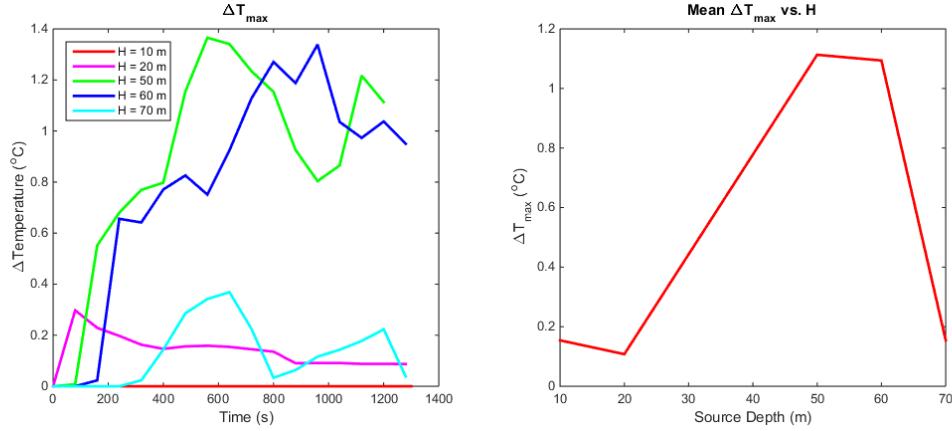
Time series of ΔT_{max} while varying H (left). Relationship of ΔT_{max} and H (right).

Figure 34.   Thermal Surface Signature

The extent of the signature was similar to the signature itself. The peak thermal extent was at 50 m, which is the depth closest to the MLD that exists in the stratified water. The 70 m source depth was just out of reach. This finding in Figure 35 is comparable with that of Newman (2014), which discovered a source greater than 75 m depth would not yield a surface temperature signature with the baseline conditions set for these studies.
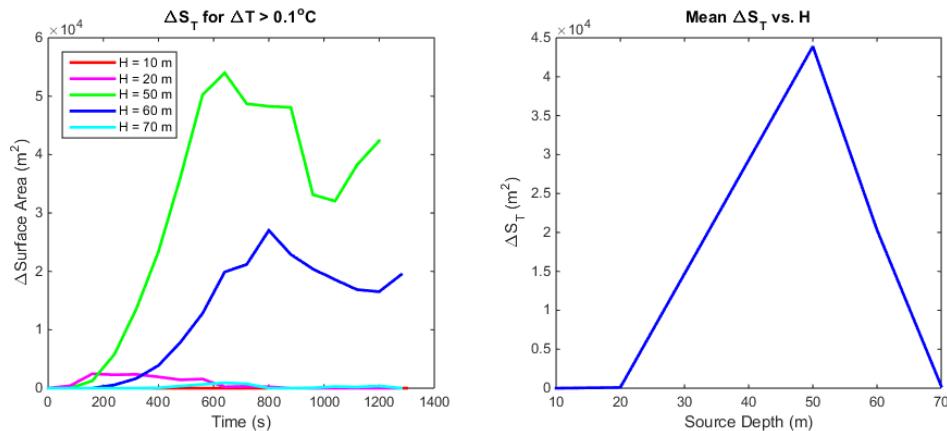
Time series of ΔS_T while varying H (left). Relationship of ΔS_T and H (right).

Figure 35.   Areal Extent of Thermal Surface Signature

2. Impact on Temperature Perturbations in the Interior

The sub propagating in the upper mixed layer has unique results as the wake interacts with the MLD at 30 m depth. When operating in the gradient waters, the interaction is more characteristic of the previous runs. While the signatures of the $H = 10$ m and $H = 20$ m experiments did not impact the surface, we see in Figure 36 that the internal signatures are more substantial. Clearly, the closer the source is to the MLD, the more significant the internal effects are. The deeper runs have less of an interior presence, but a decreasing trend is present with increasing depth.
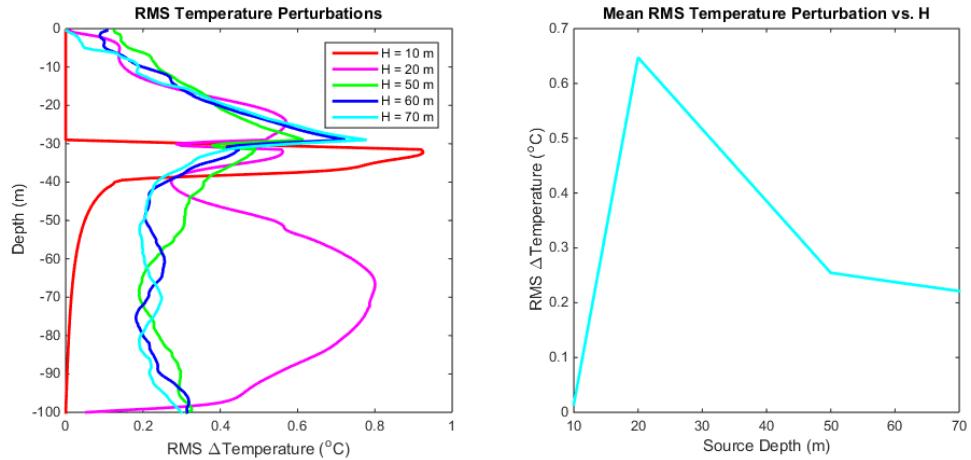
RMS temperature perturbations in depth, z, while varying H (left). Relationship of RMS temperature perturbation and H (right).

Figure 36.   Internal RMS Temperature Perturbations

With the exception of the $H = 30$ m and $H = 40$ m model runs, it is difficult to state deterministically that the proximity of the source and the MLD is the greatest effect on the internal signature. But with the data presented in Figure 37, we can say confidently that is does have the greatest impact.
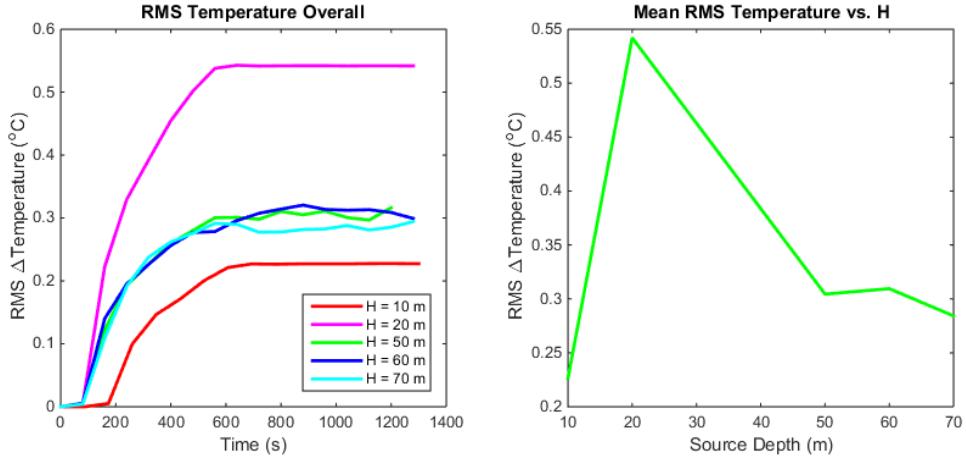
RMS temperature perturbations while varying H (left). Relationship of RMS temperature perturbation and H (right).

Figure 37.   Overall Internal RMS Temperature Perturbations

### 3.   Impact on Velocity Perturbation in the Interior

The signatures produced by the depths within the upper layer are much smoother than the convoluted perturbations below the MLD. And again they do not follow the characteristic patterns of the signatures seen in past experiments. The interaction of the wakes on either side of the MLD are unique. The shallower runs have greater velocity flux at particular depths but their signature is dampened. The deeper ones portray a more oscillatory, wavelike pattern throughout the column. The left plot in Figure 38 portrays these explanations well.
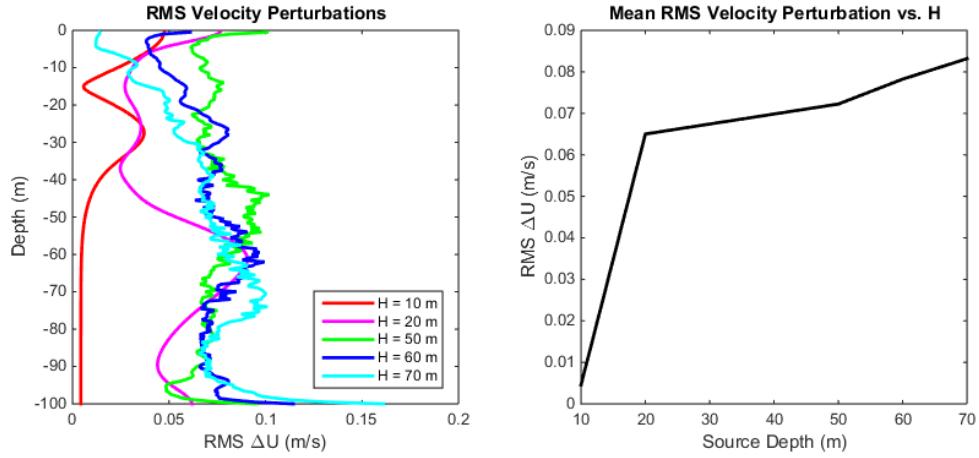
RMS velocity perturbations in depth, z, while varying H (left). Relationship of RMS velocity perturbation and H (right).

Figure 38.   Internal RMS Velocity Perturbations

Toward the beginning of the model runs, the shallowest depths of 10 m and 20 m show a peak in the interior velocity signature around 200–300 seconds. The greatest U velocity fluctuations occur as the perturbed medium reaches the vicinity of the MLD as depicted in Figure 39.
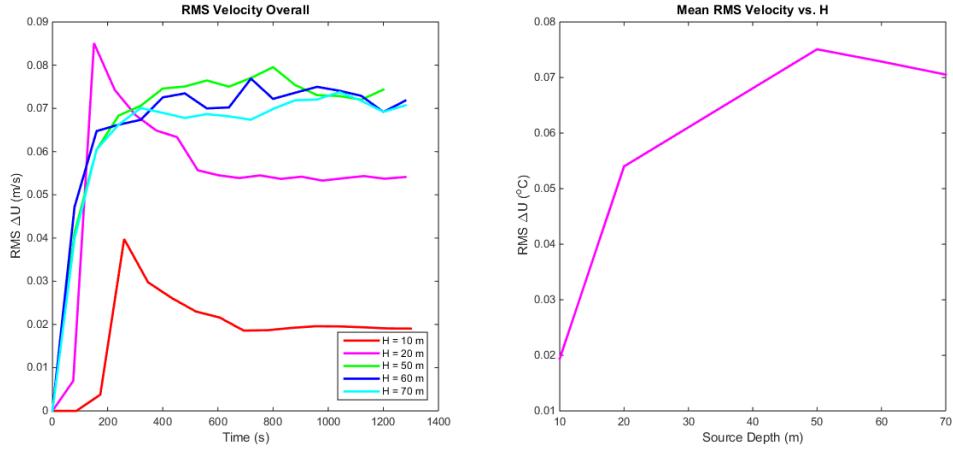
RMS velocity perturbations while varying H (left). Relationship of RMS velocity perturbation and H (right).

Figure 39.   Overall Internal RMS Velocity Perturbations

43

F.   VARYING SOURCE SIZE

The source size variation experiments expectedly produced the most distinct results; a probable effect of the choice in variation. The mid-size submerged body, on which the study was based, was chosen as an optimization for naval hydrodynamics. This size brought to light the effect of small submarines propagating through a stratified medium. The idea from there was to extrapolate the signatures to other size submerged bodies. If small sources result in temperature signatures at the surface, then large submerged bodies will surely generate the same, if not higher signatures. This series of model runs gives validity to that argument. A smaller body of half the diameter and length as well as a larger body of twice the ellipsoidal volume were used to model the wake patterns. The findings were fascinating. There was no surprise that the larger body would considerably perturb the medium, and the thermal and flow signals were large and vast. And although the small source did not result in thermal signatures detectable at the surface of the ocean, the interior patterns were significant, and sufficient for internal unmanned underwater vehicle (UUV) detection.

1.   Impact on Thermal Surface Signature and Extent

Figure 40 yields our hypothesized results with respect to surface thermal signature. The initial, most striking feature of the results is the absence of the surface response for the smallest ellipsoid. Next is the increase in temperature change of the largest sub both in the early stages of the run as well as sustained throughout the duration of the experiment. The flat-line signal from the small submerged body is precisely the reason why a larger sized sub was chosen as the baseline size. It is not only important to acquire a signature for scientific study, but it is also more representative of operational submarines.
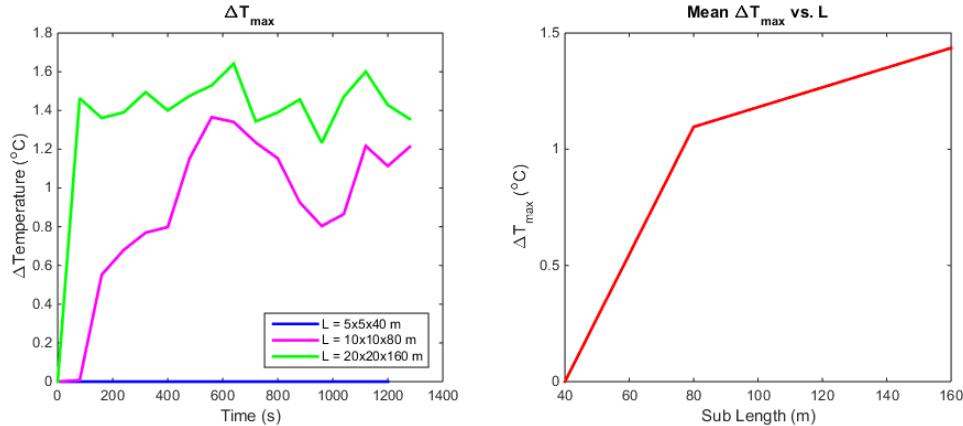
Time series of ΔT_{max} while varying L (left). Relationship of ΔT_{max} and L (right).

Figure 40.　Thermal Surface Signature

What appeared a significant increase in temperature in the plot above is dulled by the vastness of the signature in Figure 41. The temperature perturbation from the baseline to large submerged body was a difference of approximately $0.25°C$, but the areal extent is nearly nine times that of the baseline source signature. The oceanic surface area impacted by the large sub propagating through the medium is impressive.
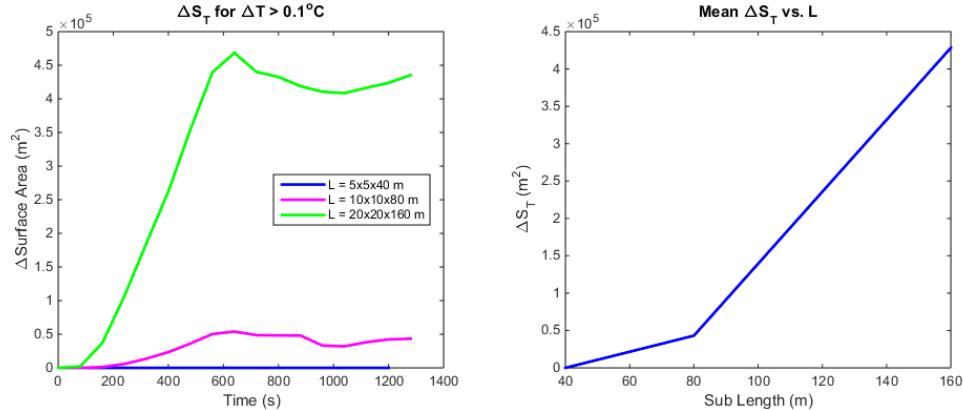
Time series of ΔS_T while varying L (left). Relationship ΔS_T of and L (right).

Figure 41.　Areal Extent of Thermal Surface Signature

45

2.   Impact on Temperature Perturbations in the Interior

While no surface response was generated with the smallest sub, there were definitely internal wakes both produced and measured. In fact, at the mixed layer depth, with all other variables constant, the smallest ellipsoid generated the same temperature difference as the sub twice its size. Otherwise, throughout the 100 m depth, the changes in temperature were notably different. The largest sub would reasonably generate wakes that perturb the water considerably more than the smaller vessels. The differences are near linear in proportion. The right plot in Figure 42 expresses these relations. The sub sizes have a 1:4 ratio; 40 m:160 m and the measured temperature changes are 0.1°C:0.4°C.
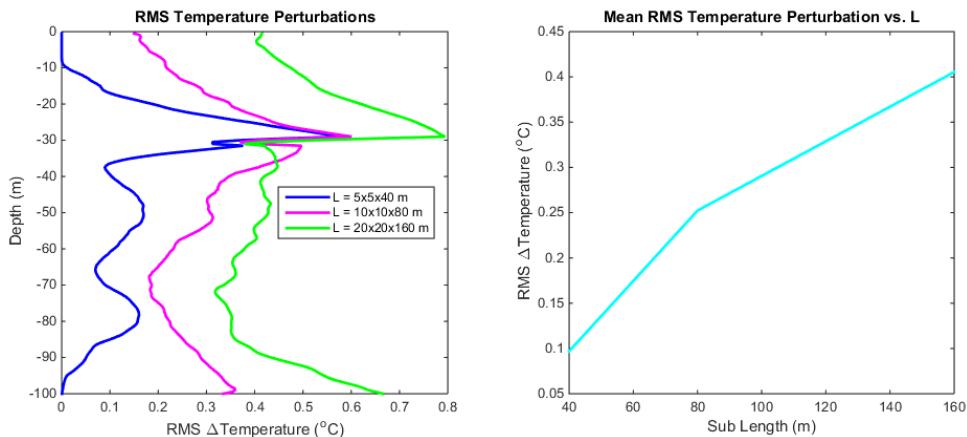
RMS temperature perturbations in depth, z, while varying L (left). Relationship of RMS temperature perturbation and L (right).

Figure 42.   Internal RMS Temperature Perturbations

The overall internal temperature perturbations, as presented in Figure 43, are slightly less than what is captured in the snapshot of the signatures at time, t = 1200s, but that image does convey the significant differences that the sub size brings to the interior. Disrupting the column of stratified fluid at these various surface areas has distinct impacts both at the surface and internally.
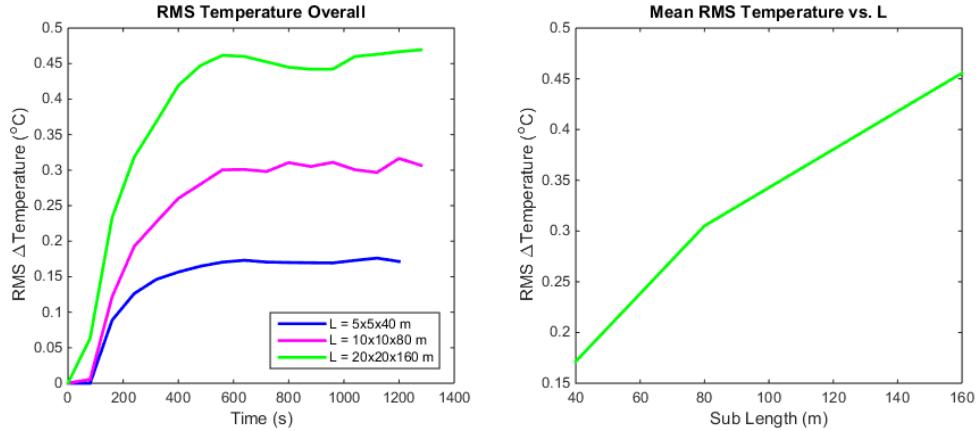
46

RMS temperature perturbations while varying L (left). Relationship of RMS temperature perturbation and L (right).

Figure 43.   Overall Internal RMS Temperature Perturbations

### 3.   Impact on Velocity Perturbations in the Interior

Comparable to the temperature perturbations, the changes in velocity signatures between the three submarines are sizeable. Interestingly, the internal velocity changes match the size of the submerged bodies. The smallest sub yields one large hump with one subtle peak and two even more subtle troughs. The baseline sub has a noticeable peak immediately following the sub flow at 50 m depth and two larger troughs on either side. The largest sub has a trough behind the flow with to peaks on either side and two more troughs adjacent to the peaks. The velocity flows are wavelike and move faster with the larger sized undersea vessels. The issue with the left plot in Figure 44 is that it does not reveal the direction of the flow, only the changes in velocity. The flow on either side of each sub as it transits through the medium is the main perturbation from surface friction. The flow following this sub is the propulsion.
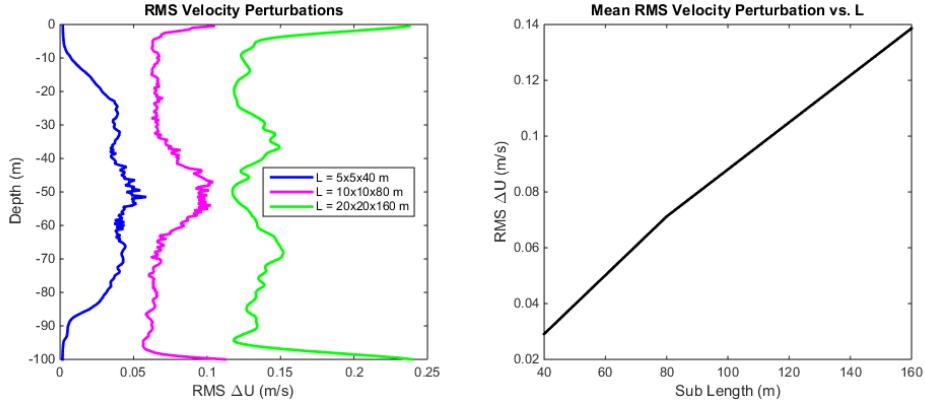
47

RMS velocity perturbations in depth, z, while varying L (left). Relationship of RMS velocity perturbation and L (right).

Figure 44.   Internal RMS Velocity Perturbations

Figure 45 pictorially denotes the vertical cross-section of the self-propelled submerged body flow propagation. The submerged volume is transiting at U = -10 m/s with a background velocity (flow depicted in green) of U = 0 m/s. The blue wakes are in the negative U zonal direction indicating that the perturbations are due to form drag or surface friction. The medium is being pulled in the direction of propagation. The yellow wakes represent the propulsion of U = 5 m/s in the positive zonal direction.
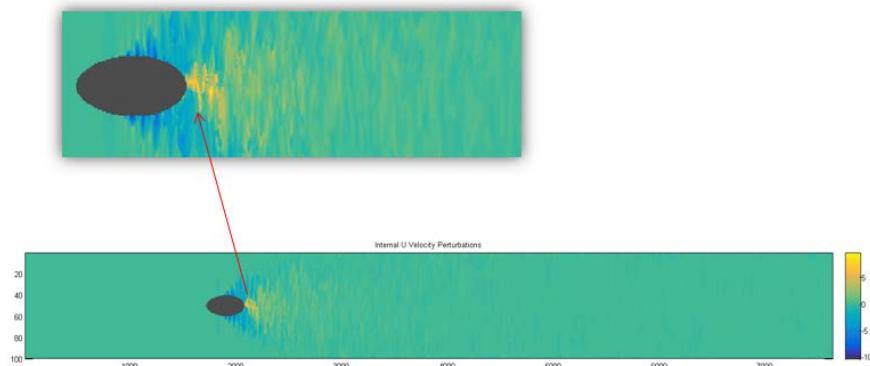
Internal cross-section of velocity perturbations generated from a self-propelled submerged body propagating with varied source size, L = 20×20×160 m.

Figure 45.   Internal Velocity Perturbations

48

A clearer depiction of the velocity changes over time is displayed in Figure 46. The largest sub disturbs the column more quickly and at nearly double the rate of the baseline sub.
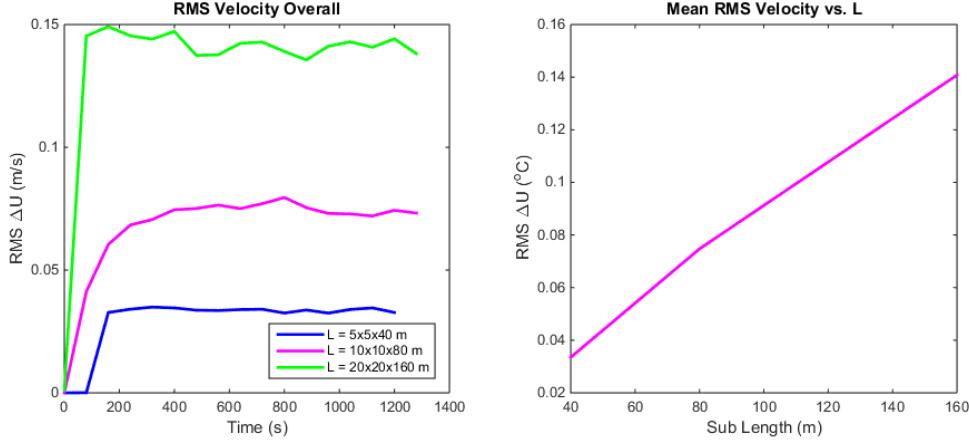
RMS velocity perturbations while varying L (left). Relationship of RMS velocity perturbation and L (right).

Figure 46.   Overall Internal RMS Velocity Perturbations

G.   VARYING MOMENTUM EXCESS

The crux of this study lies in the variations of the parameter, momentum excess. Momentum, $p = m \times U$, is the product of a mass and a velocity of a given object. In this study, we will use momentum per unit volume, $p = \rho \times U$, where density, $\rho = {m}/{V}$, is the ratio of a mass and its volume. With a changing velocity, also known as acceleration, momentum can be derived to yield a difference of forces, $m\frac{dU}{dt} = F_{thrust} - F_{drag}$ (Meunier and Spedding 2004).

Thrust, formally propulsion, is generated by the propeller at the rear of the submarine, which drives fluid mass away from the submerged body at a given rate of motion. The thrust force is the reaction force in the opposite direction of mass flow. The drag force is created by the parasitic drag of the submarine against the fluid medium. Form drag and skin drag compose the drag force. Figure 47 depicts the force body

49

diagram of all the forces that act on the propagating SSB. In a three-dimensional, axis-symmetric experiment, where the fluid flow and submarine propagation are in *U*-zonal direction, the difference of forces is equivalent to the change in net momentum from one time step to the next (Higuchi and Kubota 1990).
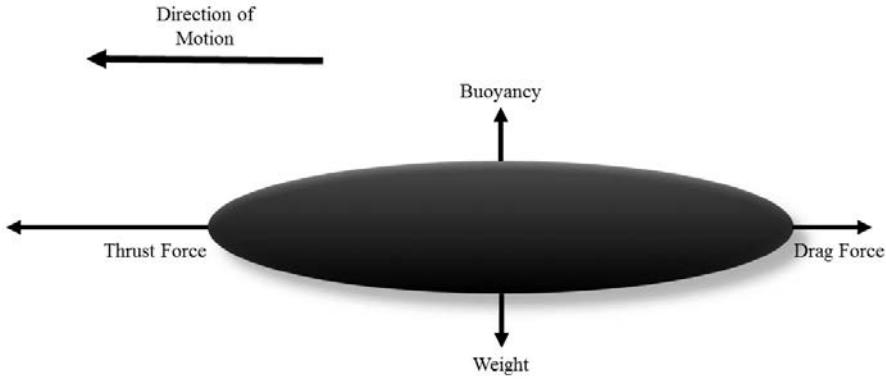
An axisymmetric self-propelled submerged body propagating in the U zonal direction with a strong thrust to drag ratio.

Figure 47.   Submerged Body Force Diagram

In our case, the thrust force-generated momentum excess is the calculated value of the drag form against the source. We then inject that value into a region or volume behind the SSB, as to induce propulsion. Without this inserted momentum, the experiment would model a towed body (Newman 2014). The towed body experiment would be considered a non-zero momentum case, as there is an uninterrupted transfer of momentum from the body to the medium (Afanasyev 2004). No active interaction, like blades of the propeller pushing against the water, is being produced between the fluid and the body (Afanasyev and Korabel 2006). There is passive interaction between the body and the medium due to pressure and viscosity. With the addition of the momentum in the region behind the submerged body, we model a self-propelled source. Variations in this momentum represent scenarios where a submerged body would need an excess of momentum in order to maintain a given velocity. The towed body run is a full momentum case. The excess momentum coefficient, *a*, at a value of 1.0 signifies a zero momentum-

excess case. A zero-momentum flow is one where the self-propelled submerged body is transiting at a constant velocity. The constant speed means no acceleration, therefore the difference in F_{thrust} and F_{drag} is zero. The force generated by the rear propeller is perfectly offset by the drag applied to the front of the body (Afanasyev and Korabel 2006); the momentum of the source is counterbalanced by the propulsion.

Many experiments compare wakes of various submerged body forms, such as cubes, spheres, and cylinders, as the size and amplitude of the wakes both depend on the shape of the bluff body (Meunier and Spedding 2004). We chose the streamlined prolate spheroid or ellipsoid not only because it most closely resembles a submarine, for naval relevance, but because if we acquired significant results with an elliptical bluff body, the rigid edges of other bluff bodies would produce even more notable results. The most important part of the submerged body is its size. Meunier and Spedding (2004) found that wakes do not recall the shape of the bluff body, only the amount of water transported by said body. With a value of 2.0 we model the addition of double the momentum, or the momentum required to maintain a velocity of 10 m/s against a current. A value of -1.0 simulates the decay of momentum, or the loss of momentum necessary to maintain a 10 m/s velocity, perhaps riding a current. Each time step, the code forces the sub velocity to 0 m/s, obtains the change in momentum calculated through the Navier-Stokes equations, and inserts that change in the artifact called the "jet." The jet is the volume in the region behind the SSB. In doing this for each delta t, we maintain a $U = 10$ m/s self-propelled body in the -x direction. These results are congruent with Meunier and Spedding (2006), which found that for lower speeds, the momentum flux expelled by the propeller is higher than that produced by the drag force and the opposite for higher speeds.

We were ecstatic to discover that our velocity profiles in Figure 48 were consistent with those of de Stadler and Sarkar (2011). The zero added momentum $a = 0.0$ resembles the Gaussian profile of (a) towed body with no propulsion, where the drag force is entirely transferred from the propagating submerged body to the medium. This profile yields a velocity deficit only, meaning the dragged prolate ellipsoid produces a full momentum wake. The momentum excess coefficient $a = 1.0$ depicts the profile (b) constant velocity, self-propelled body with zero net momentum. The drag and thrust

51

forces are perfectly balanced, hence no net momentum is transferred from the submarine to the ocean. The double inflected profile portrays the two drag (velocity deficit) lobes adjacent to the central thrust (velocity excess) lobe directly in line with the propagating body at a constant velocity (de Stadler and Sarkar 2011). Profile $a = 2.0$ again illustrates a self-propelled submerged body propagating at constant velocity, yet this body has excess momentum added to the jet behind it. The addition of the momentum excess signifies acceleration, and similar deficit lobes with a stronger thrust lobe occur. Not depicted in the figure above, but added to our study for interest, is the $a = -1.0$ negative momentum excess or momentum deficit. This represents submersible deceleration, and yields similarities to the $a = 1.0$ case with an inverse velocity profile. Both the thrust and drag forces are in the same direction, thus signatures should be more evident.
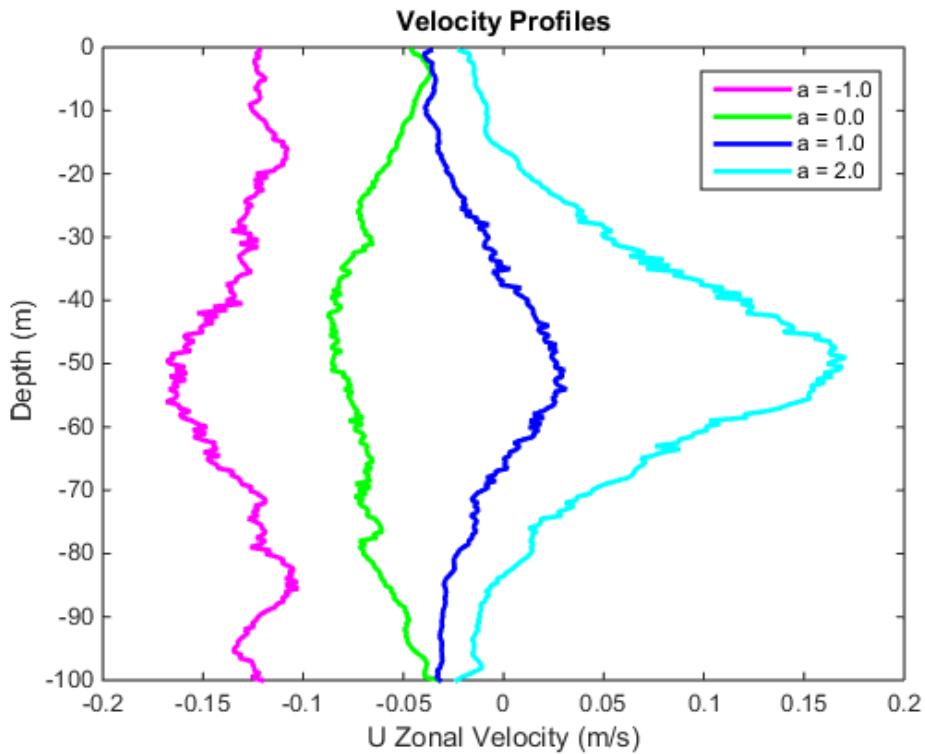
Velocity profiles were averaged in half grid space in order to capture the internal signatures behind the propagating bodies, neglecting the regions of non-flow.

Figure 48.   Velocity Profiles Varying Momentum Excess

Another important finding in our research that is also consistent with de Stadler and Sarkar (2011), shown in Figure 49, is that though seemingly momentumless by force balances, even the $a = 1.0$ case has momentum exchange from the wake to the fluid via internal waves, specifically later in time. Research from Novikov et al. (2009) delivered the near impossibility of experimentally modeling momentumless wakes, with the imbalance at approximately one percent. In our study, there exists momentum signatures even in our zero net momentum wakes.
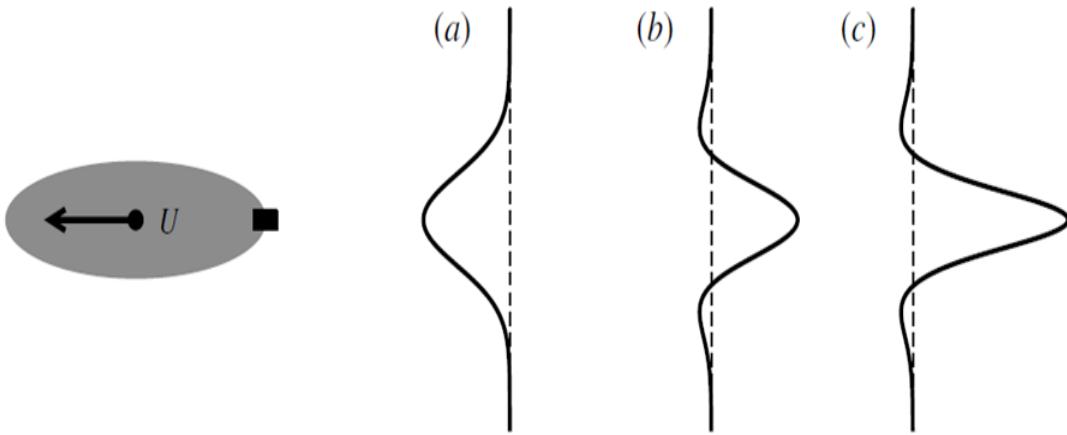
Velocity profiles in a stratified fluid of: (a) dragged body with no propulsion, (b) self-propelled body with zero net momentum, and (c) propelled body with excess momentum. The dashed line represents zero velocity. Source: de Stadler and Sarkar (2011).

Figure 49.   Published Theoretical Velocity Profiles

1.   **Impact on Thermal Surface Signature and Extent**

Initially in Figure 50, notice the downward trend expected from the transitions of the negative momentum to the towed body to the zero net momentum cases. Where the other cases flatten out in the later times, the negative momentum case continues to increase. The drag force and thrust force interfere constructively where the zero net momentum and momentum excess cases have destructive interference of the wake energy. We would, however, expect the $a = 2.0$ case to have a larger impact than the zero net momentum run.
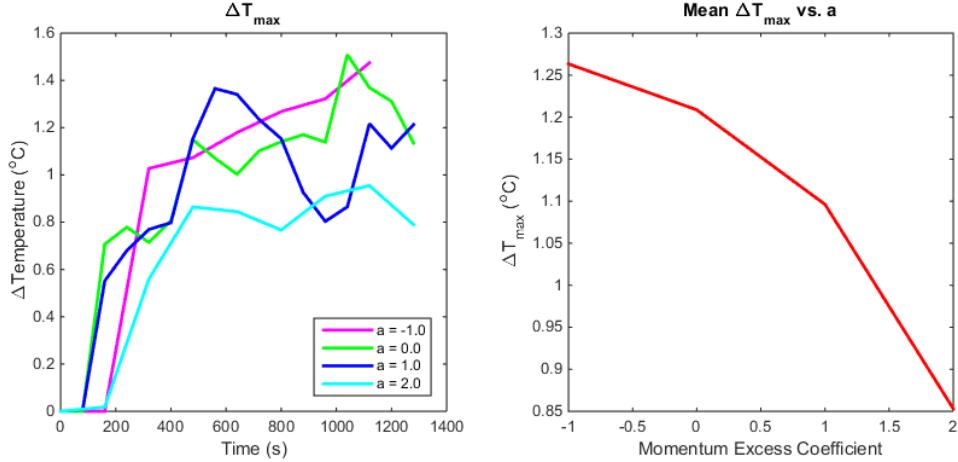
Time series of ΔT_{max} while varying *a* (left). Relationship of ΔT_{max} and *a* (right).

Figure 50.   Thermal Surface Signature

A similar trend is depicted from the areal extent of the thermal surface signature in Figure 51. The continued increase of surface area covered by the signature of the negative momentum model run is immense.
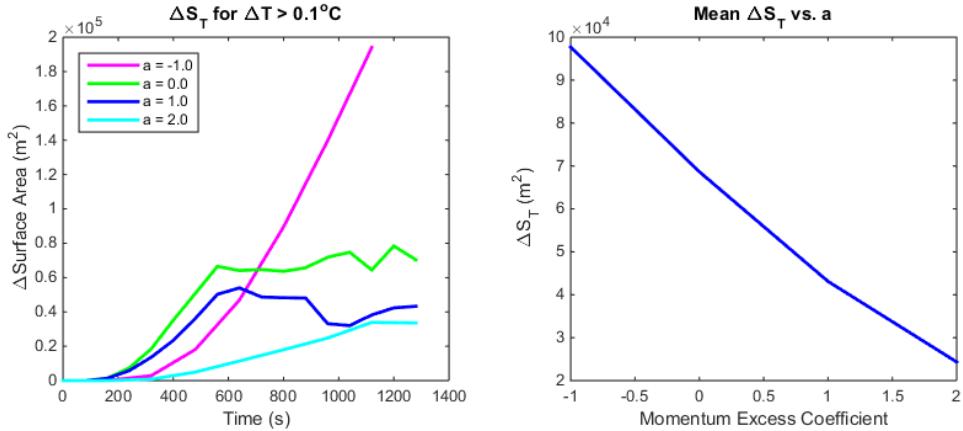
Time series of ΔS_T while varying *a* (left). Relationship of ΔS_T and *a* (right).

Figure 51.   Areal Extent of Thermal Surface Signature

54

2.   Impact on Temperature Perturbations in the Interior

The internal signatures are more representative of the results expected when the experiments were run. Though not phenomenally different in order of magnitudes, the signatures in Figure 52 do portray the trend hypothesized. The destructive interference of the $a = 1.0$ case is likely to reduce signature, but as previously mentioned, the zero-momentum case still produces a detectable response.
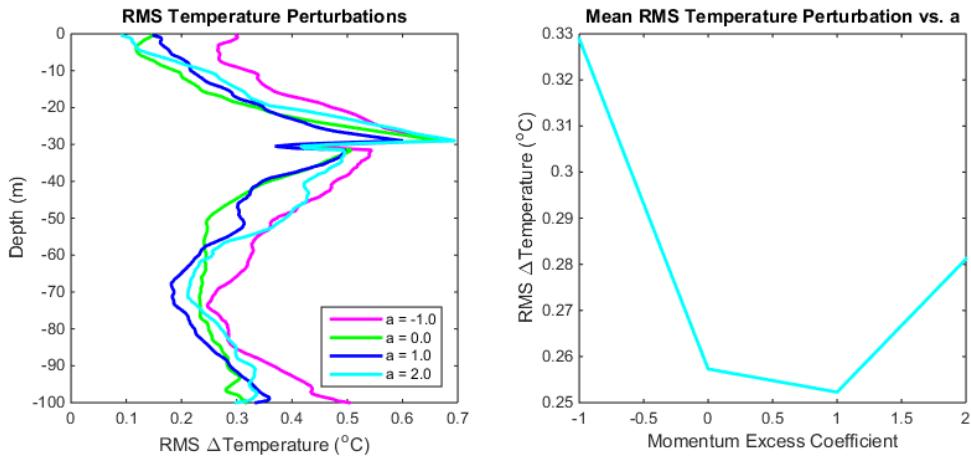
RMS temperature perturbations in depth, z, while varying a (left). Relationship of RMS temperature perturbation and a (right).

Figure 52.   Internal RMS Temperature Perturbations

Figure 53 displays the vertical cross-section of the internal temperature perturbations for each momentum experiment run time in its entirety. The first two images, depicting the net negative momentum and towed body runs, show the most impressive internal temperature perturbations. With the wider contour intervals in the top two vertical cross-sections, we see they are still the most vivid in color. The bottom intervals are narrower, and still the wake signatures are faded. The baseline experiment, $a = 1.0$, in particular, signifies that though an internal wake is generated, it is much less noticeable than those with net momentum fluxes. Notice also, how the wakes towards the end of the run become horizontally wider and their vertical signatures are weaker, through wake dispersion. This finding is consistent with late-wake studies that the

initially turbulent vortex streets will become stable in time as the stratification hinders vertical development, but the horizontal pancake eddies grow (Voropayev and Smirnov 2003). Wake formation and development are influenced by the density gradient or stratification, which stabilize the late flow.
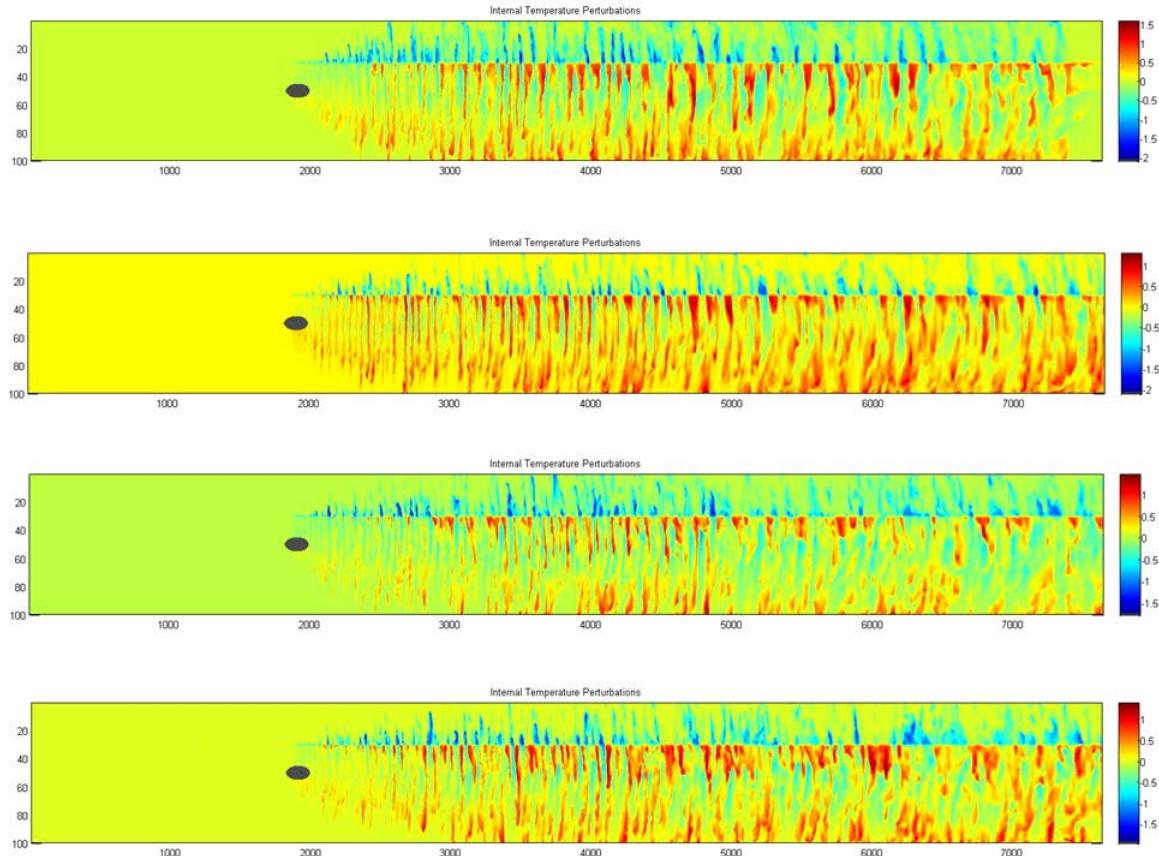
The varied momentum excess follows each image respectively, $a = -1, 0, 1, 2$.

Figure 53.   Internal Temperature Perturbations Varying Momentum Excess

The full run time averaged plots in Figure 54 represent, even better, the initial downward trend followed by an increase in temperature perturbation from the excess momentum body run.
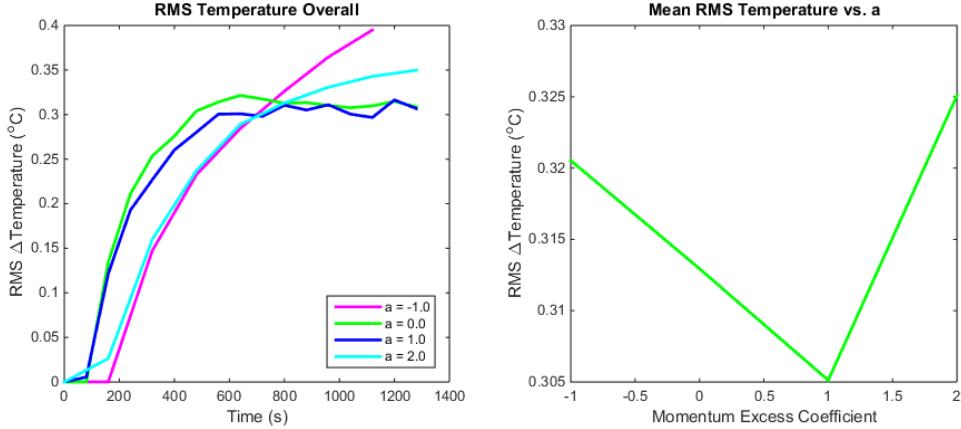
56

RMS temperature perturbations while varying *a* (left). Relationship of RMS temperature perturbations and *a* (right).

Figure 54.   Overall Internal RMS Temperature Perturbations

3.   Impact on Velocity Perturbations in the Interior

The most noticeable of trends is in the velocity signatures. Like the temperature signatures in the early experiments where temperature gradients were varied, we expected the greatest velocity signatures to be with experimental changes in velocity or momentum. While in appearance there are similarities between Figure 55 and Figure 48 velocity profiles, the RMS velocity perturbations represent the changes occurring internally. The momentum deficit case has the most change in momentum, and it is fairly uniform throughout the interior grid space. The momentum excess case of *a* = 2.0, remains truest to the velocity profile in Figure 48, with the greatest velocity in the wake of the sub. The towed body experiment yields visible internal changes in velocity. Finally, the zero net momentum case, which though true to the velocity profile form, is the least changing internally. This finding is important as it conveys that the experiments were run correctly, and have major impacts for momentum signatures as well as internal submerged body detection.
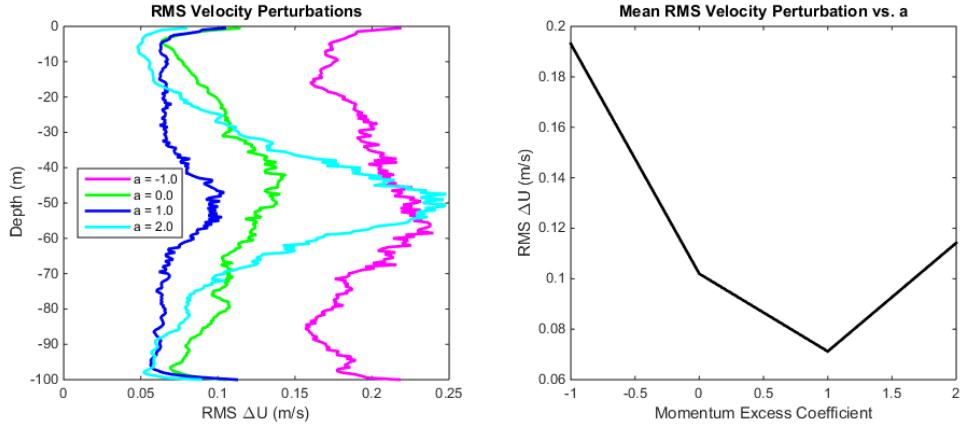
RMS velocity perturbations in depth, z, while varying *a* (left). Relationship of RMS velocity perturbation and *a* (right).

Figure 55.   Internal RMS Velocity Perturbations

While the images above portray the internal signature at the end of the respective run, Figure 56 depicts the true averaged trend. As anticipated, the greatest perturbations result from the momentum deficit case, followed by the positive momentum excess case. The zero net momentum case yields the least velocity change internally. This finding will be important for naval architects and operators alike.
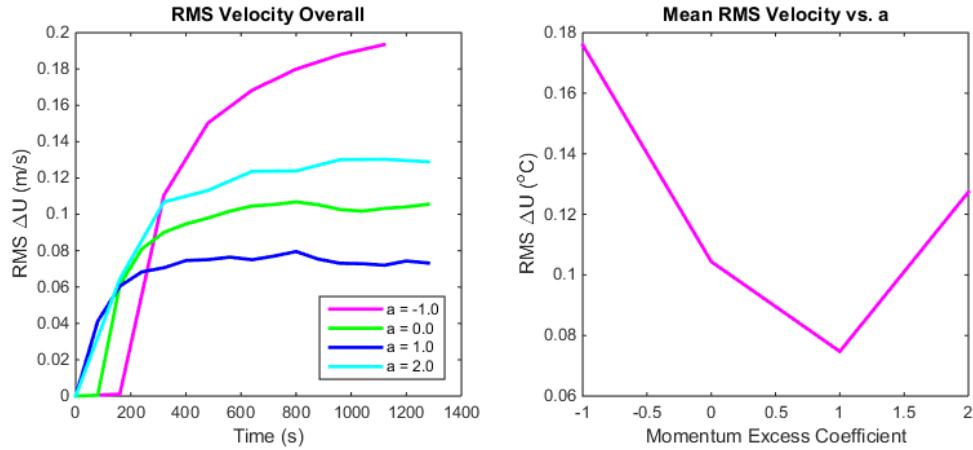
RMS velocity perturbations while varying *a* (left). Relationship of RMS velocity perturbation and *a* (right).

Figure 56.   Overall Internal RMS Velocity Perturbations

IV.   ANALYSIS OF RESULTS

A.   EXPERIMENTAL RESPONSES

1.   Environmental Parameters

The environmental parameters were buoyancy frequency, N^2, mixed layer depth, MLD, and temperature gradient, $\partial T/\partial z$. The Brunt-Väisälä Frequency runs were conducted to determine the effect of oceanic stability on the propagation of an SSB generated wake. An increased stability in the ocean strongly dampens the temperature perturbation signatures in the interior and to the surface. There is an inconclusive result in the internal velocity perturbation signatures measured with increased stability. As the wake signature propagated, the eddy vortices spread out and the signature is advected in an oscillatory motion. The mixed layer experiments indicated significant correlations between surface temperature signatures and the proximity of the SSB to the MLD. When the submarine transited near the mixed layer depth, and within the stratified medium, stronger responses were measured. The internal thermal signatures portrayed an even more apparent change. When the MLD increased to 40 m and the sub travelled along the 50 m depth line, the thermal changes were impressive. Again, a less conclusive response was viewed for the velocity perturbations. In our temperature gradient simulations, we observed linear increases in surface and internal thermal signatures with increasing $\partial T/\partial z$. The greater the stratification internally, the more significant the perturbation response will be. Specifically, in the vicinity of the MLD, there were profound signature jumps.

The strongest thermal gradient yielded the greatest RMS surface (1.175°C) and internal (0.423°C) temperature perturbations measured. The MLD proved a close second. For the internal velocity perturbation responses, however, N^2, MLD and $\partial T/\partial z$ values were all approximately 0.06 m/s.

2.   Source Parameters

The source parameters used in our experimental data sets were velocity, U, depth, H, size, L, and momentum excess, a. The source velocities were varied from 5 m/s to 15

m/s with 2.5 m/s intervals. These speeds are analogous to propagation speeds in the submarine fleets, and still enable us to use baseline modeling codes for comparative calculations. The depths of the submerged body were 10 m, 20 m, 50 m, 60 m, and 70 m. 30 m and 40 m depths were excluded from this report due to error in model outputs, we believe because of the proximity of the sub to the MLD. Viscosity inputs were later changed to generate productions for the omitted runs, but they were not comparable for this study. There were three experiments run with size variations to include a small SSB of 5x5x40 m, our baseline sub of 10x10x80 m, and a large submerged prolate ellipsoid of 20x20x160 m. The smallest SSB represents large UUVs or very small operational manned vehicles. Our baseline and large submarine specifications can be seen in fleet submarines internationally. Finally, the momentum excess parameter was varied to demonstrate subs propagating via self-propulsion, acceleration, deceleration, as well as by way of towing for continuity from Newman (2014).

While there were unconvincing results yielded from the thermal surface signatures within the velocity runs, the internal responses provided insight. The fastest SSB at $U = 15$ m/s not only propagated the greatest internal temperature changes, but the greatest velocity perturbations. The peak temperature perturbation exists around the MLD both for the final time as well as throughout the duration of the run. Each internal velocity signature varied in pattern with varying SSB propagation speed.

The sub depth varying experiments were unique in that their subsequent responses did not alone depend on the changing source parameter, but on the proximity of the SSB to the environmental parameters. When the body propagated within the mixed layer, we found minimal thermal advection to the surface, however they were the most thermally responsive in the interior. The runs where the SSB transited in the stratified medium, yet still in the vicinity of the MLD, yielded the greatest impact on thermal surface and internal velocity signatures. Unfortunately, when the closing distance between the sub and MLD was approximately 10 m or less, the model was unable to resolve the calculated perturbations, resulting in a blown up simulation. Viscosity adjustments to the model code were made to better resolve the runs within the mixed layer. The improved resolution shows how the responses in differing environmental regimes will vary.

Changes in the self-propelled submerged body size were made to reiterate the point that the volume has substantial impacts to both the internal and surface signatures in temperature and velocity. The pattern and dynamics of the wakes change with the variations in ellipsoid volume changes. Though the trend of increasing perturbation signature with increasing SSB size remains throughout the model runs, the medium is perturbed uniquely. The largest sub has a greater drag friction that pulls the medium along with it in the -x propagation direction. The internal velocity profiles of the smallest sub depict the self-propulsion as the chief contributing factor of turbulent wake generation. Consistent with Meunier and Spedding (2004), we found that wake dynamics depend on the bluff body size.

The introduction of momentum excess has shed light on the wake differences between submerged bodies propagating through a stratified ocean interior by way of towing or self-propulsion. Conducting simulations while varying the a parameter enabled us to mimic and visualize realistic submarine motions in the ocean. de Stadler and Sarkar (2011) produced velocity profiles for propagating submerged bodies generating momentum. Our results were parallel to their findings for cases modeling cases for bodies that are propagating at a constant velocity, being towed, and accelerating. The full-momentum, towed body case proved to cause the most influential for the thermal surface signatures compared to the zero-net momentum and momentum excess cases. But when compared to the decelerating case, which includes momentum from drag and thrust, the towed body signatures were considerably less. The accelerating and decelerating runs had the greatest effect on the internal thermal and velocity responses. The thrust force was captured well by the model, specifically for the velocity perturbations in the interior.

The largest sub initiated the most significant surface temperature perturbation (1.355°C), with the towed body the next closest (0.947°C). The sub depth of 20 m, only one within 10 m of the MLD, yielded the greatest internal temperature perturbation (0.431°C). The largest SSB also resulted in the greatest internal velocity perturbation overall (0.134 m/s), but the decelerating and accelerating subs created only slightly smaller values. Of note, the source parameters almost exclusively generated ΔU_{RMS} values greater than the environmental parameter outputs.

THIS PAGE INTENTIONALLY LEFT BLANK

V.   PROGNOSTIC FORMULA

A.   ALGORITHM

Computational fluid dynamics is another aspect of DNS that uses algorithms and numerical analysis to solve fluid flows. Empirical formulae can be derived in numerous methods. Dimensional analysis and Buckingham Pi Theorem were used to generate the predictive algorithm for this thesis. The concept was to create a mathematical formula to determine, globally, the maximum temperature perturbation and extent at the ocean surface for a given submerged body propagating through a stratified fluid. In order to fashion such an equation, we used Buckingham Pi Theorem to non-dimensionalize the parameters. This enables the user to insert any set of parameters and yield a resultant maximum surface thermal signature and its areal magnitude. When the output values were verified, we were then able to create a similar algorithm for internal velocity perturbation signatures. By creating an algorithm to model dynamic signatures, we reduce computational resources (time and cost), increase data production, and maintain comparable precision to DNS.

1.   Momentum Excess and Additional Parameter

The formula generated for towed bodies was the inspiration for this algorithm (Newman 2014). Using the data obtained from the momentum excess, $a = 1$ runs, this algorithm applies to all zero net momentum propagating bodies. We also included an additional parameter, source size, L. In doing this, we added a new dimensionless parameter, $\pi 5$. This algorithm is more realistic, in that it incorporates the excess momentum in the form of self-propulsion as well as the variation of SSB size. Holding the source velocity, $U = 10$ m/s, and the source depth, $H = 50$ m, constant, we were able to deduce the relational dependence of the other quantities to the signature of choice.

2.   Buckingham Pi Theorem

A formal means of dimensional analysis, Buckingham Pi Theorem is a method to make quantifiable relationships of dimensionless variables through matrix mathematics.

Determining the number of variables that exist in the problem, and the number of physical dimensions or units involved, we can establish the number of pi variables needed to solve the relational equation, regardless if the form is known (Buckingham 1914).

The equations below signify the dependent, signature variables, $\pi 1$, as well as the dimensionless, independent variables, $\pi 2$, $\pi 3$, $\pi 4$, $\pi 5$. $\pi 1(\Delta T_{max})$ represents the mean-maximum temperature perturbation measured at the surface of the ocean. $\pi 1(\Delta S)$ signifies the mean surface area extent of the temperature perturbation. $\pi 1(\Delta U_{RMS})$ denotes the mean RMS velocity or momentum perturbation measured internally. $\pi 2$ is representative of the proximity of the SSB to the mixed layer depth; the closer in proximity, the larger the signature. $\pi 3$ shows the relationship of the buoyancy frequency to the signature, with constant U and H. $\pi 4$ is the ratio of temperature gradient, gravity force, depth, and thermal expansion coefficient to source speed. $\pi 5$ represents the source size, more specifically, its volume. The analysis for $\pi 5$ was more convoluted than the other parameters, hence the extra equations to clarify below.

$$\pi 1(signature) = C\ \pi 2^{\alpha 2}\ \pi 3^{\alpha 3}\ \pi 4^{\alpha 4}\ \pi 5^{\alpha 5}$$

$$\pi 1(\Delta T_{max}) = \frac{g\ \alpha\ \Delta T_{max}\ H}{U^2}$$

$$\pi 1(\Delta S) = \frac{\Delta S}{H^2}$$

$$\pi 1(\Delta U_{RMS}) = \frac{\Delta U_{RMS}}{U}$$

$$\pi 2 = \frac{H - D}{H}$$

$$\pi 3 = \frac{N\ H}{U}$$

$$\pi 4 = \frac{g\ \alpha\ \frac{\partial T}{\partial z}\ H^2}{U^2}$$

$$\pi 5 = R\ H$$

$$R = \frac{L}{3\,d^2}\left(1 + \frac{m}{\sqrt{(1-m)}}\tanh\left(\sqrt{(1-m)}\right)\right) \quad \text{and} \quad m = \frac{d^2}{L^2}$$

3. Curve Fitting for α, Control Values

By curve fitting the $\pi 1$ signature value to the pi properties that define it, we can obtain the relative dependence of each signature to the specific properties. These control values, α, signify the dependence each signature has on the pi property. Multiplying the properties raised to their control will determine the value on the right hand side of the pi theorem equation. We are then left with simple division to determine the pi coefficient for that signature. With the coefficient, C, any user can plug π properties into the dimensionless algorithm to obtain their surface or internal signature.

4. Thermal Surface Signature

The thermal surface signature $\pi 1$, when plotted against the mixed layer depth $\pi 2$, yielded an α2 value of 0.5836. There is a strong positive relationship between the surface signature and the proximity of the SSB to the MLD as depicted in Figure 57. The closer the submerged volume is to the mixed layer depth, especially while still propagating in the stratified regime, the stronger the $\pi 1$ signature, as temperatures from the depths are advected to the surface.
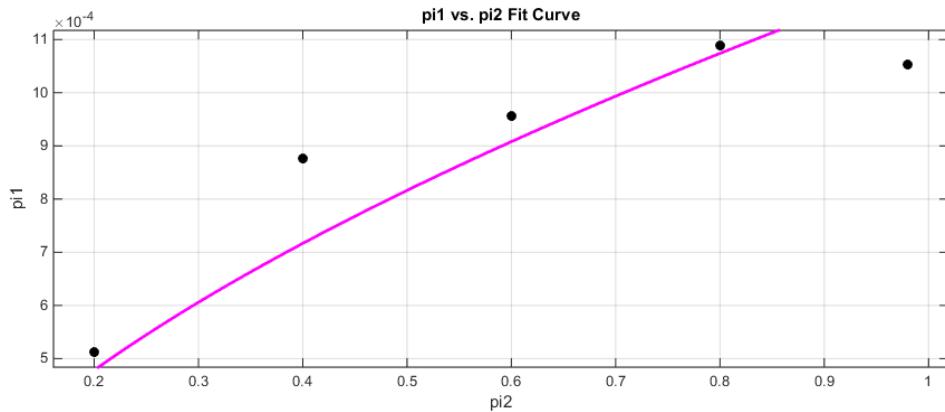
$\pi 2$ represents the variations in mixed layer depth, MLD.

Figure 57.   Fitted Curve of $\pi 1(\Delta T_{max})$ vs. $\pi 2$

65

There is an extremely slight negative correlation between the increasing buoyancy frequency of π3 and the thermal perturbation signatures of π1. The relational dependence of α3 is -0.02847, as shown in green on Figure 58.
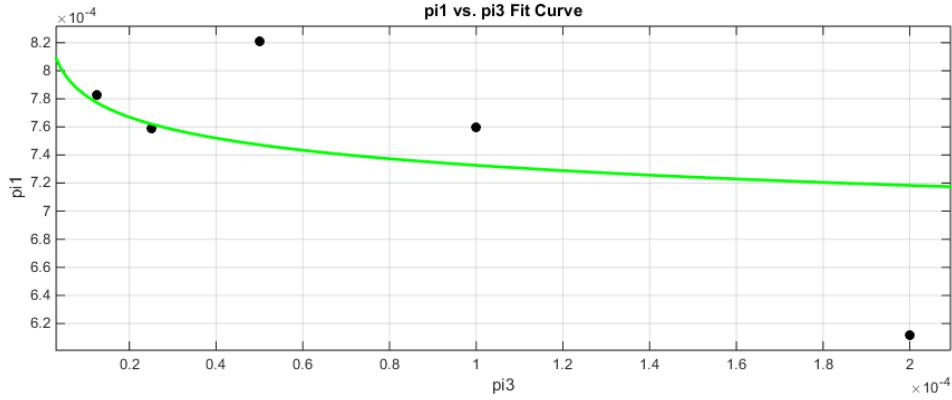
π3 represents the variations in buoyancy frequency, N^2.

Figure 58.   Fitted Curve of $\pi1(\Delta T_{max})$ vs. $\pi3$

A nearly linear dependence exists between π1 and π4. Figure 59 portrays the relationship with an α4 value, linking the thermal signature to the temperature gradient, of 0.9055. We expect a strong positive correlation between the gradient and the perturbation because there is more opportunity for temperature advection to the surface, with an increased thermocline.
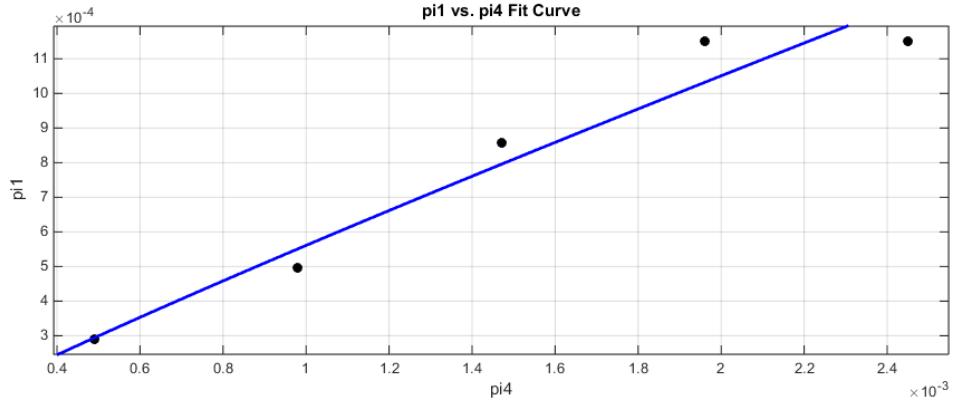
π4 represents the variations in temperature gradient, $\partial T/\partial z$.

Figure 59.   Fitted Curve of $\pi 1 (\Delta T_{max})$ vs. $\pi 4$

While there is an obvious increase in perturbation with increasing submerged body size, the relationship of $\pi 1$ and $\pi 5$ is the opposite. $\pi 5$ represents the inverse of increasing size, just in a more convoluted fashion. The $\alpha 5$ value as visualized in Figure 60 is -0.6008.
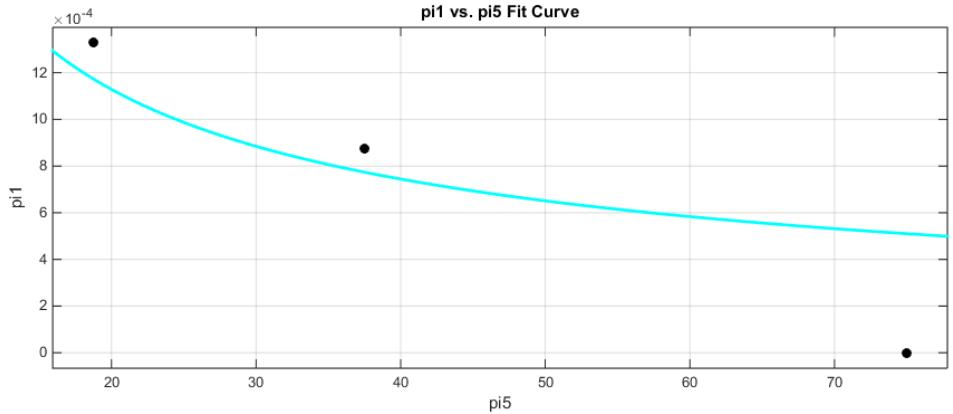
π5 represents the variations in source size, L.

Figure 60.   Fitted Curve of $\pi 1 (\Delta T_{max})$ vs. $\pi 5$

Through the equations presented earlier in the Chapter and the α, curve fitting values, we were able to deduce a mean coefficient for the thermal surface signature, C_{mean} = 2.595140894403584. Rearranging the equations, we are left with the final equation for the surface thermal perturbation algorithm.

$$\pi 1(\Delta T_{max}) = 2.595 \, \pi 2^{0.584} \, \pi 3^{-0.0285} \, \pi 4^{0.906} \, \pi 5^{-0.601}$$

$$\frac{g \, \alpha \, \Delta T_{max} \, H}{U^2} = 2.595 \left(\frac{H - D^{0.584}}{H}\right)\left(\frac{N \, H^{-0.0285}}{U}\right)\left(\frac{g \, \alpha \, \frac{\partial T}{\partial z} \, H^2}{U^2}\right)^{0.906}(R \, H^{-0.601})$$

$$\Delta T_{max} = 2.595 \left(\frac{U^2}{g \, \alpha \, H}\right)\left(\frac{H - D^{0.584}}{H}\right)\left(\frac{N \, H^{-0.0285}}{U}\right)\left(\frac{g \, \alpha \, \frac{\partial T}{\partial z} \, H^2}{U^2}\right)^{0.906}(R \, H^{-0.601})$$

5.   Surface Area of Thermal Surface Signature

The proximity of the SSB to the MLD has a linear relationship to the areal extent of the thermal signature at the air-sea interface. With an α2 value of 0.984, Figure 61 illustrates that correlation.
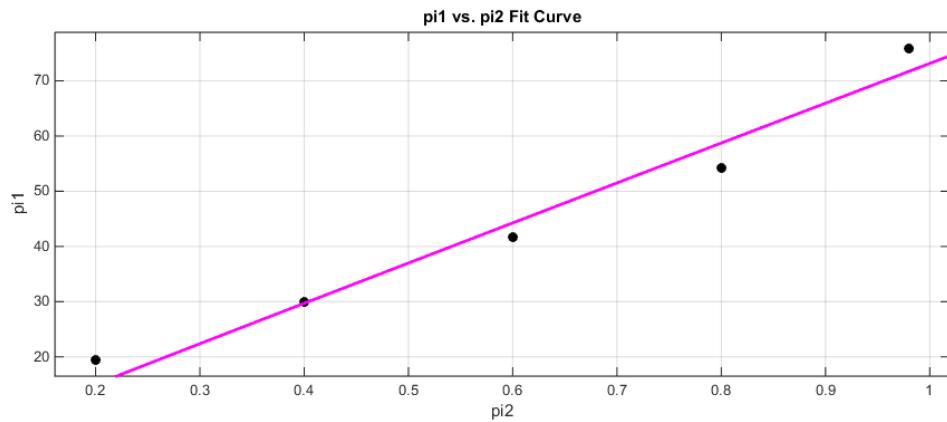
π2 represents the variations in mixed layer depth, MLD.

Figure 61.   Fitted Curve of $\pi 1(\Delta S_T)$ vs. $\pi 2$

Similar to the response between π1 and π2 for the thermal signature, π1 responds with a slightly negative slope to the π2 for the areal extent. An increasing stability, the more dampened the surface response will be. Figure 62 shows the plot of the α3 value, -0.1425.
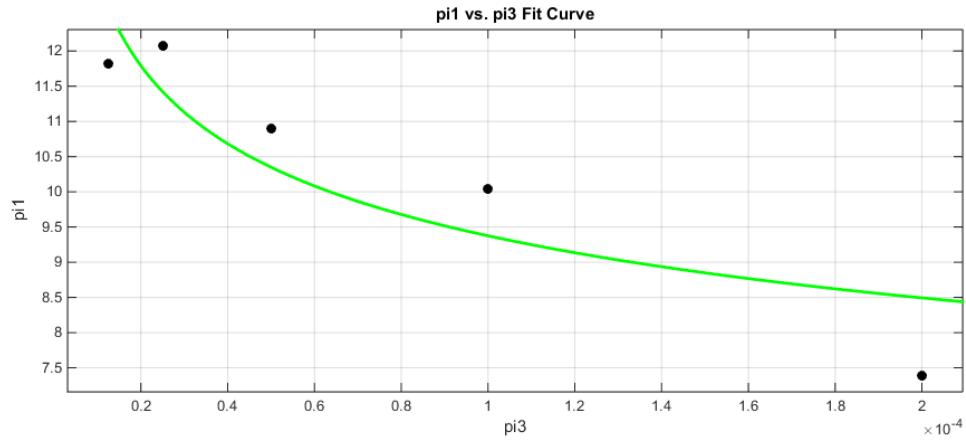
π3 represents the variations in buoyancy frequency, N^2.

Figure 62.   Fitted Curve of $\pi 1(\Delta S_T)$ vs. $\pi 3$

Again, a very strong positive relationship exists between $\partial T/\partial z$ and π1 for surface area of signature. The α4 value of 0.7902 denoted in Figure 63 shows how increasing temperature gradients with depth have resultant effects at the surface.
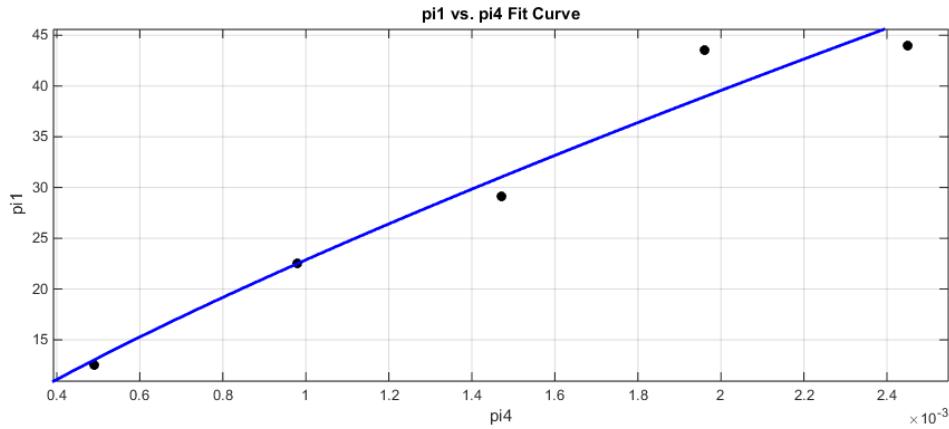
π4 represents the variations in temperature gradient, $\partial T/\partial z$.

Figure 63.   Fitted Curve of $\pi 1(\Delta S_T)$ vs. $\pi 4$

Figure 64 displays a plot similar to negative log. The α5 value of -3.365 means a very strong negative relationship between size and extent of the signature. π5 again represents inverse SSB size and each sub is double the size of the one before it.
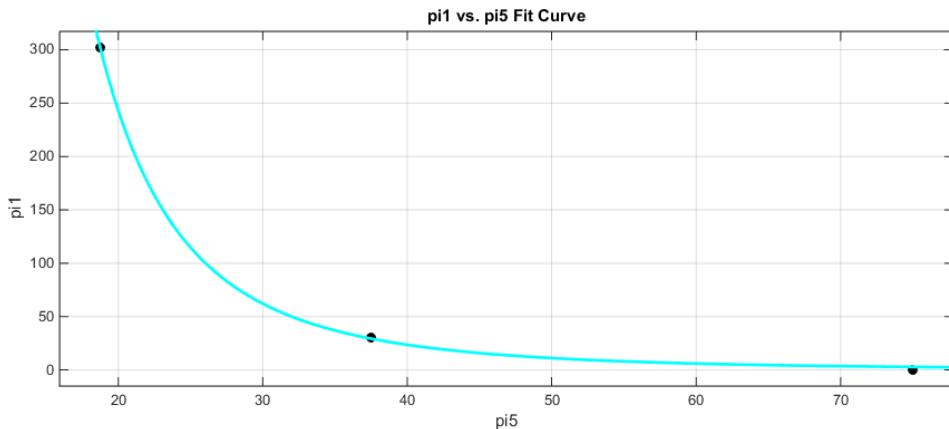
π5 represents the variations in source size, L.

Figure 64.   Fitted Curve of $\pi 1(\Delta S_T)$ vs. $\pi 5$

The mean coefficient for the thermal surface area signature is $C_{\text{mean}} =$ 178597996.2637273. The following equations are reordered to give the resultant $\pi 1$ signature.

$$\pi 1(\Delta S) = 1.786x10^8 \; \pi 2^{0.984} \; \pi 3^{-0.143} \; \pi 4^{0.790} \; \pi 5^{-3.365}$$

$$\frac{\Delta S}{H^2} = 1.786x10^8 \left(\frac{H - D^{0.984}}{H} \right) \left(\frac{N \, H^{-0.143}}{U} \right) \left(\frac{g \, \alpha \, \frac{\partial T}{\partial z} \, H^2}{U^2} \right)^{0.790} (R \, H^{-3.365})$$

$$\Delta S = 1.786x10^8 (H^2) \left(\frac{H - D^{0.984}}{H} \right) \left(\frac{N \, H^{-0.143}}{U} \right) \left(\frac{g \, \alpha \, \frac{\partial T}{\partial z} \, H^2}{U^2} \right)^{0.790} (R \, H^{-3.365})$$

6. RMS Internal U Zonal Velocity

As we concluded in the DNS Chapter, there is a minimal, if not inconclusive, relationship between the thermal environmental properties and the velocity signatures. A very small $\alpha 2$ value of -0.002414 shown in pink in Figure 65, it is apparent the SSB and MLD proximity are less important to the internal features of the velocity propagation.
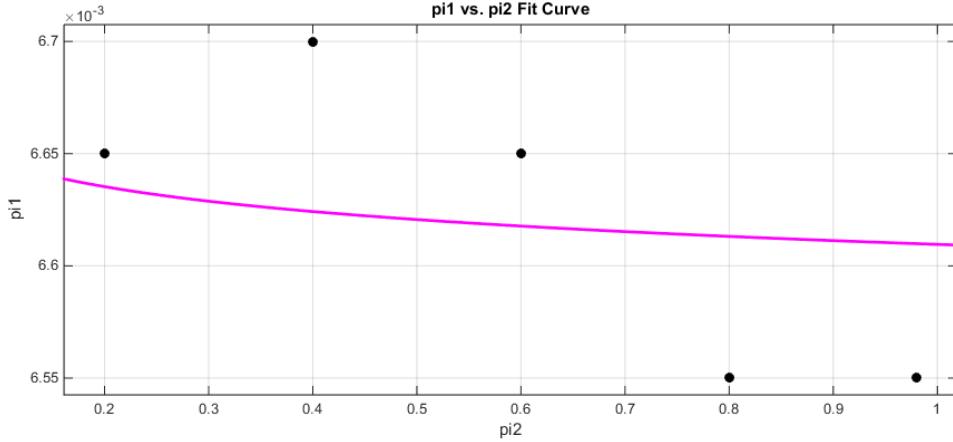
$\pi 2$ represents the variations in mixed layer depth, MLD.

Figure 65.   Fitted Curve of $\pi 1(\Delta U_{\text{RMS}})$ vs. $\pi 2$

Figure 66 is analogously inconclusive. The effect the buoyancy frequency has on the momentum perturbations with an α3 value of 0.004806 does not yield much insight.
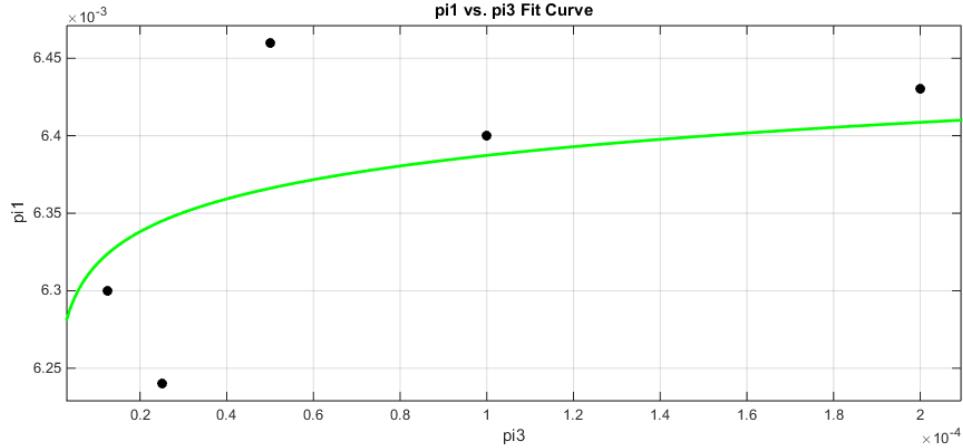
π3 represents the variations in buoyancy frequency, N^2.

Figure 66.   Fitted Curve of $\pi1(\Delta U_{RMS})$ vs. $\pi3$

A faintly larger α4 value of 0.0143 is obtained from Figure 67, but the thermal gradient still does not strongly sway the internal RMS velocity perturbations either way.
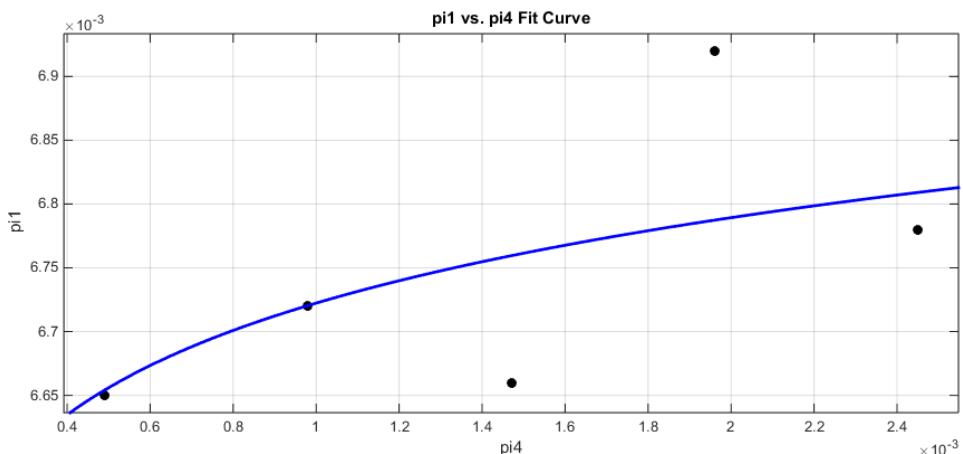
π4 represents the variations in temperature gradient, $\partial T/\partial z$.

Figure 67.   Fitted Curve of $\pi1(\Delta U_{RMS})$ vs. $\pi4$

The most influential relationship of this series is from π5. With an inverse relationship, the larger the submerged prolate ellipsoid, the larger the internal velocity signature. The α5 for Figure 68 is -1.044.
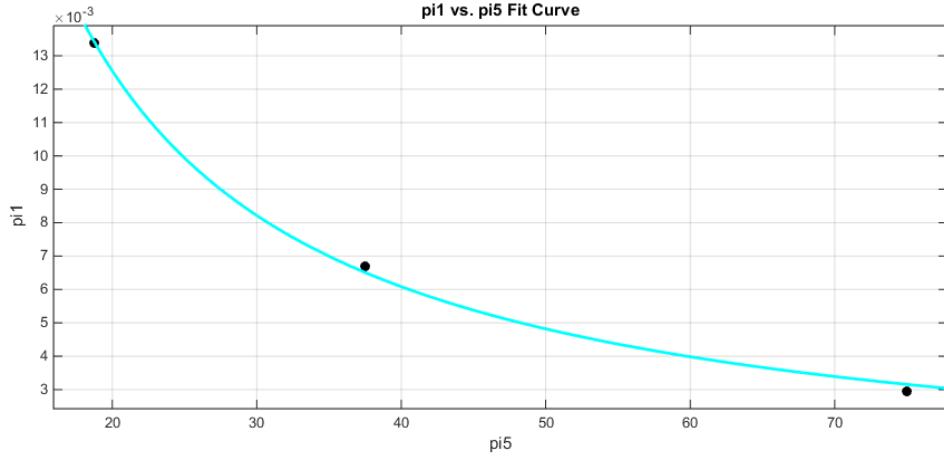
π5 represents the variations in source size, *L*.

Figure 68.   Fitted Curve of $\pi1(\Delta U_{RMS})$ vs. $\pi5$

The internal RMS velocity perturbation signature is shown in the formula below, with a mean coefficient, $C_{mean} = 0.331778190353263$.

$$\pi1(\Delta U_{RMS}) = 0.332\ \pi2^{-0.002}\ \pi3^{0.005}\ \pi4^{0.014}\ \pi5^{-1.044}$$

$$\frac{\Delta U_{RMS}}{U} = 0.332\left(\frac{H-D}{H}\right)^{-0.002}\left(\frac{N\,H}{U}\right)^{0.005}\left(\frac{g\,\alpha\,\frac{\partial T}{\partial z}\,H^2}{U^2}\right)^{0.014}(R\,H^{-1.044})$$

$$\Delta U_{RMS} = 0.332(U)\left(\frac{H-D}{H}\right)^{-0.002}\left(\frac{N\,H}{U}\right)^{0.005}\left(\frac{g\,\alpha\,\frac{\partial T}{\partial z}\,H^2}{U^2}\right)^{0.014}(R\,H^{-1.044})$$

B. VISUAL APPLICATION OF THE ALGORITHM

The images below denote the algorithm in a visual application. Using the *WOA13* climatological data in MATLAB, we were able to insert signature values obtained from our algorithm to yield geographic images of thermal surface signatures and their areal extent. Seasonal climatological norms are used as the baseline profiles in the code. This same code enables the user to plug in their respective values, specifying the sub size, depth, and speed in a region of the world for a specific season. Similar output images were portrayed in Newman (2014), but his work was representative of the towed body SB, where we will demonstrate the case of the zero net-momentum, self-propelled, submerged body case propagating at zonal velocity, $U = 10$ m/s, and depth, $H = 50$ m.

Figures 69, 70, 71, and 72 depict the seasonal outputs for the thermal surface signature and extent. The strongest signatures exist where the ocean surface has warmed atop much cooler waters below. The equatorial regions are a prime example, specifically alone the eastern boundary currents to include the California and Humboldt Currents, which flow along the Americas. These currents generate strong upwelling regions where cool water from below is brought to the upper ocean layer. These strong temperature gradients, like in our research, will yield the strongest thermal responses. Similarly, the northern and southern hemisphere mid-latitude signatures in the northern hemisphere summer and winter occur because the surface layers are much warmer due to seasonal heating, but the deeper layers remain relatively temperate. These values are more symbolic of those generated by our study. This is consistent with the synthetic profiles we created to emulate the mid-latitude regions.

1. Spring Signatures

In the Spring, we observe temperature differences of up to 2.5°C in the equatorial regions and along equatorward eastern boundary currents.
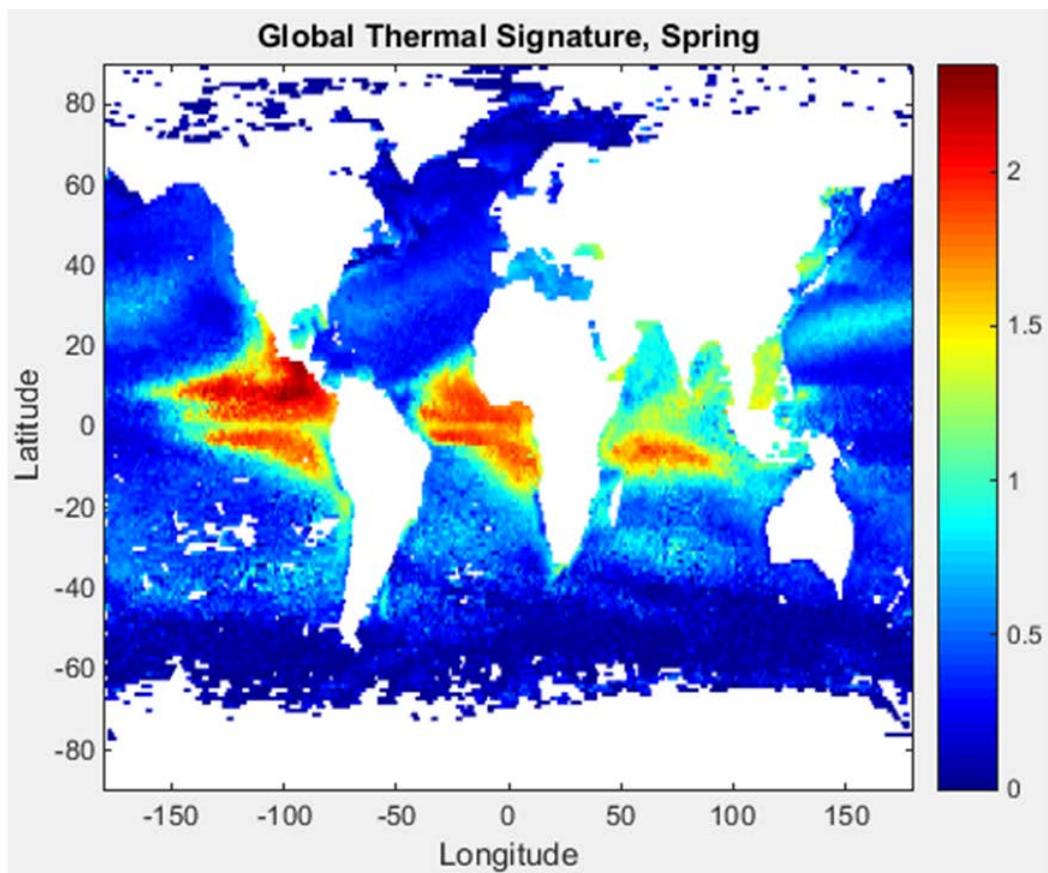
Global Thermal Signature, Spring

Signatures are surface temperature perturbations calculated using algorithm with baseline conditions and typical seasonal profiles.

Figure 69.   Global Thermal Surface Signatures, Spring

2.   Summer Signatures

In the Summer, signatures of up to 2.5°C are seen in the equatorial Eastern Pacific Ocean, but also nearly 1.5°C along northern hemisphere mid-latitudes.
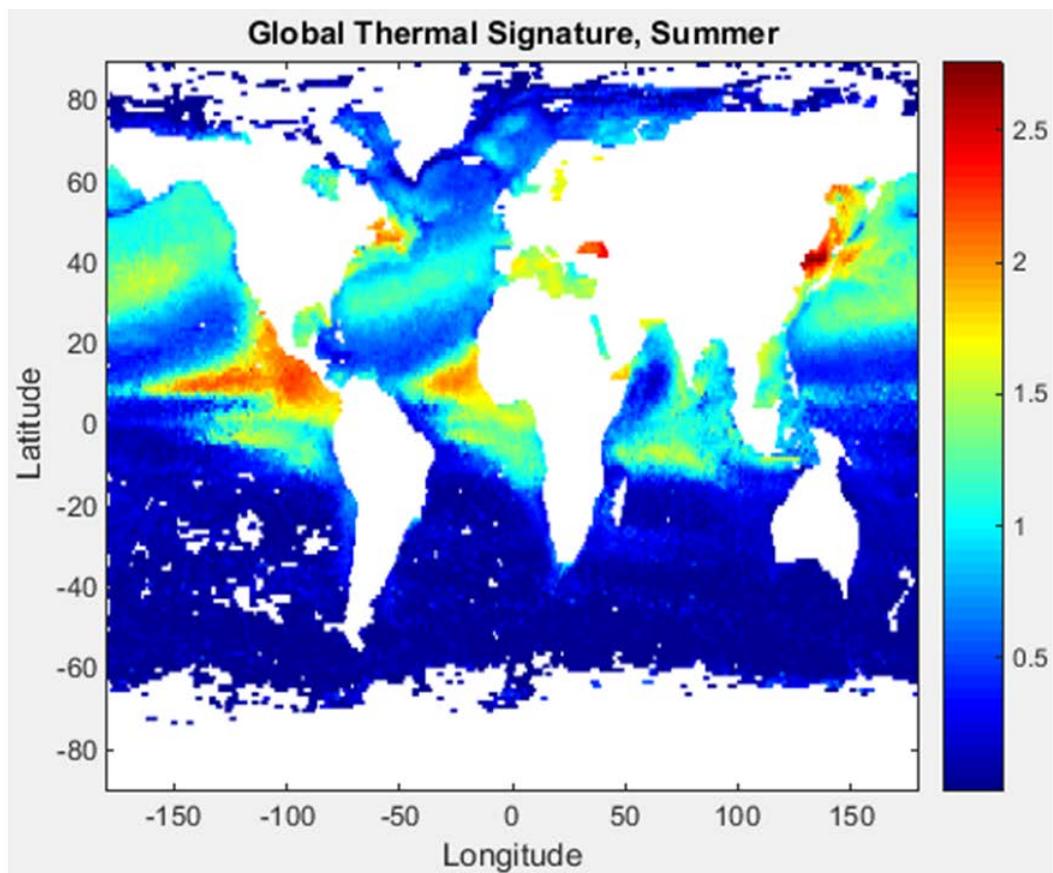
Signatures are surface temperature perturbations calculated using algorithm with baseline conditions and typical seasonal profiles.

Figure 70.　　Global Thermal Surface Signatures, Summer

3.　　Autumn Signatures

In the Autumn, temperature responses of up to 2.3°C exist in the equatorial regions, and sparse pockets of up to 1°C in the northern hemisphere tropics.
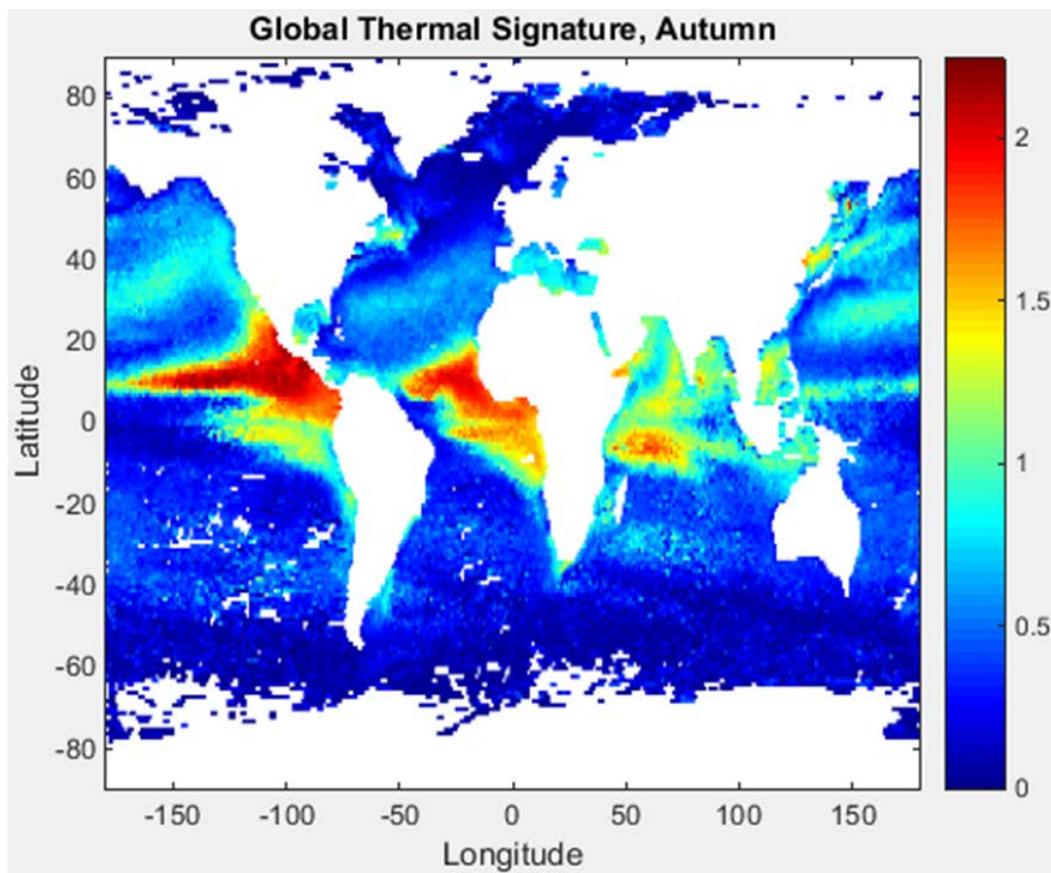
Signatures are surface temperature perturbations calculated using algorithm with baseline conditions and typical seasonal profiles.

Figure 71.   Global Thermal Surface Signatures, Autumn

4.   Winter Signatures

In the Spring, thermal signatures of up to 2.2°C are observed in the equatorial regions, and along southern hemisphere tropical and mid-latitude regions.
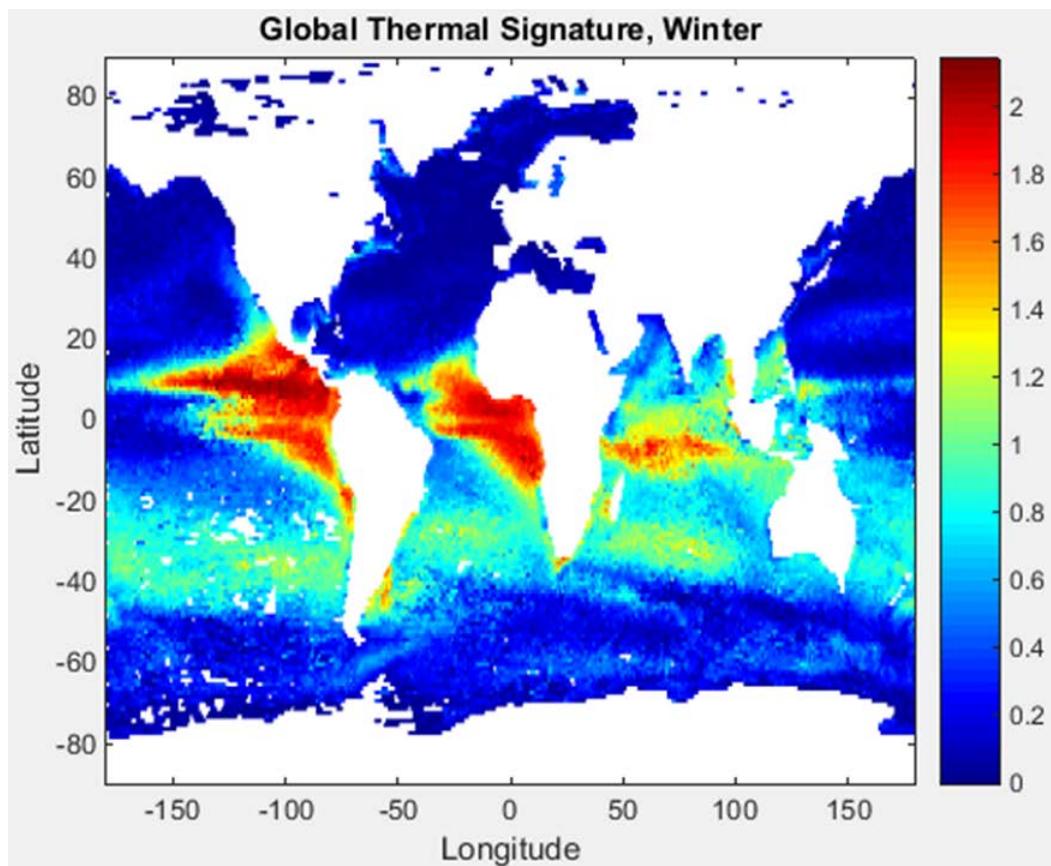
Global Thermal Signature, Winter

Signatures are surface temperature perturbations calculated using algorithm with baseline conditions and typical seasonal profiles.

Figure 72.   Global Thermal Surface Signatures, Winter

VI. DISCUSSION

A. CONCLUSIONS

Submerged bodies propagating in stratified fluid generate turbulent wakes that influence the ocean surface and interior. The pattern and dynamics of these wakes in the intermediate range, t ~ 20 minutes, vary for towed and self-propelled submerged bodies. Zero net momentum cases, where the thrust and drag forces are balanced, yield the minimum perturbations modeled. While the towed body experiments presented a significant array of temperature and velocity responses, the accelerating and decelerating runs resulted in the strongest surface and internal signatures overall. By polishing the algorithm generated by Newman (2014) using the data gathered in this study, we were able to create an alternate method for non-acoustic signature prediction.

B. OPERATIONAL RELEVANCE

Internal turbulent wakes not only disrupt fluid flow, they affect naval operations. Determining the fundamental differences between towed body and self-propelled body interactions with various environmental profiles presents naval officials tactical insight. As non-acoustic methods of submarine detection become more viable, the findings from this and similar studies offer a significant contribution. Satellite sensors can be used to measure thermal wake signatures that reach the ocean surface with accuracy to the $\pm 0.1°C$. Confirmation of the initial SAR detection can be made via UUV sensing of internal momentum perturbations. The U.S. Navy is interested in optimizing its operational success, exploiting limitations of other navies, and minimizing its environmental footprint. Unmanned system remote sensing minimizes submarine surfacing and the use of active SONAR. This optimizes mission stealth and operational safety, while preserving marine life from mass stranding.

C. FUTURE RESEARCH

The findings of this study were limited to DNS and CFD. We recommend research comparing numerical and field study results to provide an even more

comprehensive analysis of propagating submerged body interaction with a stratified ocean.

APPENDIX A. DNS EXPERIMENTS

Table 1.   Experiments Listed with Varying Control Parameters

Exp.#	Parameter Value	N²	MLD	∂T/∂z	L	a	H	U
1	2.5e-06 s⁻²	**2.5e-06 s⁻²**	30 m	0.03 °C/m	10 m x 80 m x 10 m	1	50 m	10 m/s
2	5e-06 s⁻²	**5e-06 s⁻²**	30 m	0.03 °C/m	10 m x 80 m x 10 m	1	50 m	10 m/s
3	1e-05 s⁻²	**1e-05 s⁻²**	30 m	0.03 °C/m	10 m x 80 m x 10 m	1	50 m	10 m/s
4	2e-05 s⁻²	**2e-05 s⁻²**	30 m	0.03 °C/m	10 m x 80 m x 10 m	1	50 m	10 m/s
5	4e-05 s⁻²	**4e-05 s⁻²**	30 m	0.03 °C/m	10 m x 80 m x 10 m	1	50 m	10 m/s
6	1 m	1e-05 s⁻²	**1 m**	0.03 °C/m	10 m x 80 m x 10 m	1	50 m	10 m/s
7	10 m	1e-05 s⁻²	**10 m**	0.03 °C/m	10 m x 80 m x 10 m	1	50 m	10 m/s
8	20 m	1e-05 s⁻²	**20 m**	0.03 °C/m	10 m x 80 m x 10 m	1	50 m	10 m/s
9	30 m	1e-05 s⁻²	**30 m**	0.03 °C/m	10 m x 80 m x 10 m	1	50 m	10 m/s
10	40 m	1e-05 s⁻²	**40 m**	0.03 °C/m	10 m x 80 m x 10 m	1	50 m	10 m/s
11	0.01 °C/m	1e-05 s⁻²	30 m	**0.01 °C/m**	10 m x 80 m x 10 m	1	50 m	10 m/s
12	0.02 °C/m	1e-05 s⁻²	30 m	**0.02 °C/m**	10 m x 80 m x 10 m	1	50 m	10 m/s
13	0.03 °C/m	1e-05 s⁻²	30 m	**0.03 °C/m**	10 m x 80 m x 10 m	1	50 m	10 m/s
14	0.04 °C/m	1e-05 s⁻²	30 m	**0.04 °C/m**	10 m x 80 m x 10 m	1	50 m	10 m/s
15	0.05 °C/m	1e-05 s⁻²	30 m	**0.05 °C/m**	10 m x 80 m x 10 m	1	50 m	10 m/s
16	5 m x 40 m x 5 m	1e-05 s⁻²	30 m	0.03 °C/m	**5 m x 40 m x 5 m**	1	50 m	10 m/s
17	10 m x 80 m x 10 m	1e-05 s⁻²	30 m	0.03 °C/m	**10 m x 80 m x 10 m**	1	50 m	10 m/s
18	20 m x 160 m x 20 m	1e-05 s⁻²	30 m	0.03 °C/m	**20 m x 160 m x 20 m**	1	50 m	10 m/s
20	-1	1e-05 s⁻²	30 m	0.03 °C/m	10 m x 80 m x 10 m	**-1**	50 m	10 m/s
21	0	1e-05 s⁻²	30 m	0.03 °C/m	10 m x 80 m x 10 m	**0**	50 m	10 m/s
22	1	1e-05 s⁻²	30 m	0.03 °C/m	10 m x 80 m x 10 m	**1**	50 m	10 m/s
23	2	1e-05 s⁻²	30 m	0.03 °C/m	10 m x 80 m x 10 m	**2**	50 m	10 m/s
24	10 m	1e-05 s⁻²	30 m	0.03 °C/m	10 m x 80 m x 10 m	1	**10 m**	10 m/s
25	20 m	1e-05 s⁻²	30 m	0.03 °C/m	10 m x 80 m x 10 m	1	**20 m**	10 m/s
26	50 m	1e-05 s⁻²	30 m	0.03 °C/m	10 m x 80 m x 10 m	1	**50 m**	10 m/s
27	60 m	1e-05 s⁻²	30 m	0.03 °C/m	10 m x 80 m x 10 m	1	**60 m**	10 m/s
28	70 m	1e-05 s⁻²	30 m	0.03 °C/m	10 m x 80 m x 10 m	1	**70 m**	10 m/s
29	5 m/s	1e-05 s⁻²	30 m	0.03 °C/m	10 m x 80 m x 10 m	1	50 m	**5 m/s**
30	7.5 m/s	1e-05 s⁻²	30 m	0.03 °C/m	10 m x 80 m x 10 m	1	50 m	**7.5 m/s**
31	10 m/s	1e-05 s⁻²	30 m	0.03 °C/m	10 m x 80 m x 10 m	1	50 m	**10 m/s**
32	12.5 m/s	1e-05 s⁻²	30 m	0.03 °C/m	10 m x 80 m x 10 m	1	50 m	**12.5 m/s**
33	15 m/s	1e-05 s⁻²	30 m	0.03 °C/m	10 m x 80 m x 10 m	1	50 m	**15 m/s**

Note: Experiments 3, 9, 13, 17, 22, 26, and 31 are all the same baseline simulation, and are included to demonstrate experimental variations within their respective sets.

THIS PAGE INTENTIONALLY LEFT BLANK

APPENDIX B. RESPONSE VALUES

Table 2.   Maximum Response Values by Experiment

Parameter, Value	ΔT_{MAX}, t	ΔS_T, t	T_{RMS}	U_{RMS}	T_Z	U_Z
N^2=2.5e-06 s^{-2}	1.2692 °C, 480 s	63210 m², 640 s	0.3424 °C	0.0764 m/s	0.6481 °C	0.1006 m/s
N^2=5e-06 s^{-2}	1.2138 °C, 551.1 s	63320 m², 630 s	0.3165°C	0.0744 m/s	0.6483 °C	0.1104 m/s
N^2=1e-05 s^{-2}	1.3653 °C, 551.1 s	54000 m², 630 s	0.3105 °C	0.0795 m/s	0.6635 °C	0.1046 m/s
N^2=2e-05 s^{-2}	1.0360 °C, 472.4 s	49470 m², 551 s	0.2951 °C	0.0791 m/s	0.5919 °C	0.1043 m/s
N^2=4e-05 s^{-2}	0.8879 °C, 472.4 s	36440 m², 784 s	0.2593 °C	0.0771 m/s	0.5629 °C	0.1105 m/s
MLD=1 m	1.3786°C, 1120 s	132140 m², 640 s	0.2582 °C	0.0766 m/s	0.3393 °C	0.0996 m/s
MLD=10 m	1.4324 °C, 880 s	101410 m², 960 s	0.2569 °C	0.0763 m/s	0.4447 °C	0.0973 m/s
MLD=20 m	1.2541 °C, 880 s	67534 m², 640 s	0.2865 °C	0.0788 m/s	0.5852°C	0.0979 m/s
MLD=30 m	1.3653 °C, 560 s	53996 m², 640 s	0.3164 °C	0.0795 m/s	0.6008 °C	0.1122 m/s
MLD=40 m	0.8318 °C, 800 s	40866 m², 880 s	0.3443 °C	0.0772 m/s	0.6842 °C	0.1046 m/s
0.01 °C/m	0.4118 °C, 400 s	23481 m², 640 s	0.1032 °C	0.0773 m/s	0.2191 °C	0.1100 m/s
$\partial T/\partial z$ =0.02 °C/m	0.7695 °C, 320 s	45669 m², 560 s	0.2122 °C	0.0775 m/s	0.3916 °C	0.1033 m/s
$\partial T/\partial z$ =0.03 °C/m	1.3653 °C, 560 s	53996 m², 640 s	0.3164 °C	0.0795 m/s	0.6152 °C	0.1021 m/s
$\partial T/\partial z$ =0.04 °C/m	1.7914 °C, 800 s	74706 m², 640 s	0.4166 °C	0.0811 m/s	0.8246 °C	0.1089 m/s
$\partial T/\partial z$ =0.05 °C/m	1.9430 °C, 880 s	76102 m², 960 s	0.5374 °C	0.0794 m/s	1.0931 °C	0.1052 m/s
L=5 m x 40 m x 5 m	0.0000 °C, 0 s	0 m², 0 s	0.1761 °C	0.0349 m/s	0.5799 °C	0.0587 m/s
L=10 m x 80 m x 10 m	1.3653 °C, 560 s	53996 m², 640 s	0.3164 °C	0.0795 m/s	0.6008 °C	0.1122 m/s
L=20 m x 160 m x 20 m	1.6418 °C, 640 s	468440 m², 640 s	0.4694 °C	0.1491 m/s	0.7946 °C	0.2398 m/s
a=-1	1.474 °C, 1120 s	194060 m², 1120 s	0.3949 °C	0.1935 m/s	0.6884 °C	0.2397 m/s
a=0	1.5086 °C, 1040 s	78399 m², 1200 s	0.3215 °C	0.1068 m/s	0.668 °C	0.1441 m/s
a=1	1.3653 °C, 560 s	53996 m², 640 s	0.3164 °C	0.0795 m/s	0.6008 °C	0.1122 m/s
a=2	0.9547 °C, 1120 s	33910 m², 1120 s	0.3498 °C	0.1303 m/s	0.6961 °C	0.2483 m/s
H=10 m	0.0000 °C, 0 s	0 m², 0 s	0.2276 °C	0.0398 m/s	0.9246 °C	0.0475 m/s
H=20 m	0.2975 °C, 80 s	2462 m², 160 s	0.5429 °C	0.0851 m/s	0.8004 °C	0.0906 m/s
50 m	1.3653 °C, 560 s	53996 m², 640 s	0.3164 °C	0.0795 m/s	0.6152 °C	0.1021 m/s
H=60 m	1.3386 °C, 960 s	27020 m², 800 s	0.3205 °C	0.0769 m/s	0.7233 °C	0.1144 m/s
H=70 m	0.3687 °C, 640 s	920 m², 640 s	0.2943 °C	0.0738 m/s	0.7789 °C	0.1613 m/s
U=5 m/s	1.1402 °C, 1120 s	27179 m², 1280 s	0.2992 °C	0.0402 m/s	0.6054 °C	0.0511 m/s
U=7.5 m/s	1.0063 °C, 1200 s	61713 m², 1200 s	0.3317 °C	0.06 m/s	0.6415 °C	0.0808 m/s
U=10 m/s	1.3653 °C, 560 s	53996 m², 640 s	0.3164 °C	0.0795 m/s	0.6008 °C	0.1122 m/s
U=12.5 m/s	1.1496 °C, 1280 s	52096 m², 1040 s	0.3355 °C	0.0968 m/s	0.6407 °C	0.1299 m/s
U=15 m/s	1.2232 °C, 400 s	41402 m², 400 s	0.3899 °C	0.1114 m/s	0.7871 °C	0.1151 m/s

Note: The responses were averaged in half grid space in order to properly capture the extent of the maximum values and neglect the undisturbed grid space. They were also averaged in half time in order to measure the signature once it reached the surface.

Table 3.   Mean Response Values by Experiment

Parameter, Value	ΔT_{MAX}	ΔS_T	T_{RMS}	U_{RMS}	T_Z	U_Z
N^2=2.5e-06 s^{-2}	0.7988 °C	29556 m²	0.2423 °C	0.0630 m/s	0.3119 °C	0.0738 m/s
N^2=5e-06 s^{-2}	0.7743 °C	30175 m²	0.2266 °C	0.0624 m/s	0.2984 °C	0.0735 m/s
N^2=1e-05 s^{-2}	0.8380 °C	27242 m²	0.2169 °C	0.0646 m/s	0.2854 °C	0.0766 m/s
N^2=2e-05 s^{-2}	0.7753 °C	25098 m²	0.2108 °C	0.0640 m/s	0.2817 °C	0.0752 m/s
N^2=4e-05 s^{-2}	0.6239 °C	18484 m²	0.1901 °C	0.0643 m/s	0.2328 °C	0.0751 m/s
MLD =1 m	1.0738 °C	77517 m²	0.1983 °C	0.0655 m/s	0.2473 °C	0.0735 m/s
MLD =10 m	1.1106 °C	55348 m²	0.1976 °C	0.0655 m/s	0.2459 °C	0.0704 m/s
MLD =20 m	0.9753 °C	42586 m²	0.2237 °C	0.0665 m/s	0.2633 °C	0.0740 m/s
MLD =30 m	0.8936 °C	30504 m²	0.2432 °C	0.0670 m/s	0.2921 °C	0.0721 m/s
MLD =40 m	0.5232 °C	19722 m²	0.2724 °C	0.0665 m/s	0.3083 °C	0.0720 m/s
$\partial T/\partial z$ =0.01 °C/m	0.2954 °C	12759 m²	0.0818 °C	0.0665 m/s	0.0972 °C	0.0717 m/s
$\partial T/\partial z$ =0.02 °C/m	0.5078 °C	23035 m²	0.1664 °C	0.0672 m/s	0.1963 °C	0.0753 m/s
$\partial T/\partial z$ =0.03 °C/m	0.8737 °C	29706 m²	0.2392 °C	0.0666 m/s	0.3008 °C	0.0735 m/s
$\partial T/\partial z$ =0.04 °C/m	1.1746 °C	44383 m²	0.3296 °C	0.0692 m/s	0.386 °C	0.0781 m/s
$\partial T/\partial z$ =0.05 °C/m	1.1745 °C	44893 m²	0.4227 °C	0.0678 m/s	0.4953 °C	0.0748 m/s
L=5 m x 40 m x 5 m	0.0000 °C	0 m²	0.1391 °C	0.0295 m/s	0.1283 °C	0.0285 m/s
L=10 m x 80 m x 10 m	0.8936 °C	30504 m²	0.2432 °C	0.0670 m/s	0.2921 °C	0.0721 m/s
L=20 m x 160 m x 20 m	1.3551 °C	308290 m²	0.3771 °C	0.1338 m/s	0.4556 °C	0.1366 m/s
a=-1	0.918 °C	61427 m²	0.2188 °C	0.1239 m/s	0.3816 °C	0.1923 m/s
a=0	0.9473 °C	46915 m²	0.2535 °C	0.0863 m/s	0.2904 °C	0.1036 m/s
a=1	0.8936 °C	30504 m²	0.2432 °C	0.0670 m/s	0.2921 °C	0.0721 m/s
a=2	0.6341 °C	14159 m²	0.2277 °C	0.1024 m/s	0.3292 °C	0.1141 m/s
H=10 m	0.0000 °C	0 m²	0.1663 °C	0.0186 m/s	0.0836 °C	0.0140 m/s
H=20 m	0.1364 °C	778 m²	0.4307 °C	0.0533 m/s	0.4960 °C	0.0502 m/s
H=50 m	0.8737 °C	29706 m²	0.2392 °C	0.0666 m/s	0.3008 °C	0.0735 m/s
H=60 m	0.7949 °C	12333 m²	0.2450 °C	0.0657 m/s	0.2747 °C	0.0705 m/s
H70 m	0.1284 °C	215 m²	0.2312 °C	0.0633 m/s	0.2618 °C	0.0666 m/s
U=5 m/s	0.6240 °C	7583.3 m²	0.1983 °C	0.0304 m/s	0.2801 °C	0.0397 m/s
U=7.5 m/s	0.7020 °C	30159 m²	0.2479 °C	0.0477 m/s	0.3038 °C	0.0586 m/s
U=10 m/s	0.8936 °C	30504 m²	0.2432 °C	0.0670 m/s	0.2921 °C	0.0721 m/s
U=12.5 m/s	0.8310 °C	29630 m²	0.2682 °C	0.0854 m/s	0.3161 °C	0.0878 m/s
U=15 m/s	0.8070 °C	11800 m²	0.3293 °C	0.0967 m/s	0.3495 °C	0.0961 m/s

Note: The responses were averaged in half grid space in order to properly capture the extent of the maximum values and neglect the undisturbed grid space.

APPENDIX C. PI THEOREM VALUES

Table 4. ΔT_{MAX} Values

π1	π2	π3	π4	π5	α2	α3	α4	α5	C
0.0007828		0.0000125				-0.02847			2.433455079
0.0007588		0.000025				-0.02847			2.405858955
0.0008212		0.00005				-0.02847			2.655596609
0.0007598		0.0001				-0.02847			2.506009874
0.0006114		0.0002				-0.02847			2.056739302
0.0011	0.98				0.5836				2.67150125
0.0011	0.8				0.5836				3.007402824
0.001	0.6				0.5836				3.233800059
0.0009	0.4				0.5836				3.687419372
0.0005	0.2				0.5836				3.069948806
0.0003			0.0005				0.9055		2.623419338
0.0005			0.001				0.9055		2.3341771
0.0009			0.0015				0.9055		2.910420053
0.0012			0.002				0.9055		2.990627928
0.0012			0.0025				0.9055		2.443488886
0				74.995				-0.6008	0
0.0009				37.495				-0.6008	2.910420053
0.0013				18.75				-0.6008	2.772250611

π1 values depend on the π2, π3, π4, and π5 values, and change for each varying experimental parameter. α values are calculated based on the plotting of the π dependent variables. *C* coefficients are obtained from the equations and averaged to yield a C_{mean}.

Table 5. ΔS_T Values

π1	π2	π3	π4	π5	α2	α3	α4	α5	C
31.0068		0.0000125				-0.1425			345890656.8
22.1392		0.000025				-0.1425			272609245.6
17.0344		0.00005				-0.1425			231527335
12.2016		0.0001				-0.1425			183058116.6
7.8888		0.0002				-0.1425			130641129.4
11.8224	0.98				0.984				99155190.42
11.8224	0.8				0.984				121071344.2
10.8968	0.6				0.984				148106599.8
10.0392	0.4				0.984				203351948
7.3936	0.2				0.984				296222946.6
5.1036			0.0005				0.7902		165262103.4
9.214			0.001				0.7902		172532514.8
11.8824			0.0015				0.7902		161502630.3
17.7532			0.002				0.7902		192231913
17.9572			0.0025				0.7902		163008094
0				74.995				-3.365	0
12.2016				37.495				-3.365	165841117.4
123.316				18.75				-3.365	162751047.3

π1 values depend on the π2, π3, π4, and π5 values, and change for each varying experimental parameter. α values are calculated based on the plotting of the π dependent variables. *C* coefficients are obtained from the equations and averaged to yield a C_{mean}.

Table 6. ΔU_{RMS} Values

π1	π2	π3	π4	π5	α2	α3	α4	α5	C
0.0063		0.0000125				0.004806			0.320611678
0.0062		0.000025				0.004806			0.314473263
0.0065		0.00005				0.004806			0.328593255
0.0064		0.0001				0.004806			0.322461977
0.0064		0.0002				0.004806			0.321389557
0.0066	0.98				-0.002414				0.334043931
0.0066	0.8				-0.002414				0.333880323
0.0067	0.6				-0.002414				0.338703817
0.0067	0.4				-0.002414				0.338372458
0.0067	0.2				-0.002414				0.337806747
0.0067			0.0005				0.0143		0.344066924
0.0067			0.001				0.0143		0.340673377
0.0067			0.0015				0.0143		0.338703817
0.0069			0.002				0.0143		0.347382355
0.0068			0.0025				0.0143		0.341257153
0.0029				74.995				-1.044	0.302307437
0.0067				37.495				-1.044	0.338703817
0.0134				18.75				-1.044	0.328575539

π1 values depend on the π2, π3, π4, and π5 values, and change for each varying experimental parameter. α values are calculated based on the plotting of the π dependent variables. *C* coefficients are obtained from the equations and averaged to yield a C_{mean}.

THIS PAGE INTENTIONALLY LEFT BLANK

LIST OF REFERENCES

Adcroft, A., C. Hill, J. M. Campin, J. Marshall, and P. Heimbach, 2004: Overview of the formulation and numerics of the MITgcm. *Proceedings of the ECMWF seminar series on Numerical Methods, Recent developments in numerical methods for atmosphere and ocean modelling*, 139.

Afanasyev, Y. D., 2004: Wakes behind towed and self-propelled bodies: Asymptotic theory. *Phys. Fluids* **16**, 3235–3238.

Afanasyev, Y. D. and V. N. Korabel, 2006: Wakes and vortex streets generated by translating force and force doublet: laboratory experiments. *J. Fluid Mech.* **553**, 119–141.

Alpers, W., 2015: Ocean internal waves. *Encyc. Rem. Sens.* 433–437.

Boyer, T. P., Antonov, J.I., Baranova, O.K., Coleman, C., Garcia, H.E., Grodsky, A., Johnson, D.R., Locarnini, R.A., Mishonov, A.V., O'Brien, T.D., Paver, C.R., Reagan, J.R., Seidov, D., Smolyar, I.V., and Zweng, M.M., 2013. World Ocean Database 2013. S. Levitus, Editor, A. Mishonov, Technical Editor, *NOAA Atlas NESDIS 72*, 209.

Buckingham, E., 1914: On physically similar systems; illustrations of the use of dimensional equations. *Phys. Rev.* **4**, 345–376.

de Stadler, M. B. and S. Sarkar, 2011: Simulation of a propelled wake with moderate excess momentum in a stratified fluid. *J. Fluid Mech.* **692**, 28–52.

Diamessis, P. J., G. R. Spedding, and J. A. Domaradzki, 2010: Similarity scaling and vorticity structure in high-Reynolds-number stably stratified turbulent wakes. *J. Fluid Mech.* **671**, 60.

Emery, W. J., S. Castro, G. A. Wick, P. Schluessel, and C. Donlon, 2001: Estimating sea surface temperature from infrared satellite and in situ temperature data. *Bull. Amer. Meteor. Soc.* **82**, 2773–2785.

Gallacher, P. C. and D. A. Hebert, 2009: Simulating a self-propelled submerged body in a coastal ocean hindcast using the NRL-MIT nonhydrostatic model. *Naval Research Laboratory, Ocean Sciences Branch, Stennis Space Center*, 2–9.

Garrett, C. and W. Munk, 1979: Internal waves in the ocean. *Annu. Rev. Fluid Mech.* **11**, 339–369.

Haun, E. A., 2012: Dynamic and kinematic signatures of propagating bodies in thermohaline staircases. *Master's Thesis, Department of Oceanography, Naval Postgraduate School*, 99.

Higuchi, H. and T. Kubota, 1990: Axisymmetric wakes behind a slender body including zeromomentum configurations. *Phys. Fluids* **2**, 1615–1623.

Klemas, V., 2012: Remote sensing of ocean internal waves: An overview. *J. Coast. Res. 2012* **28**, 540–546.

Landau, L. D. and E. M. Lifshitz, 1987: Course of theoretical physics: Fluid mechanics. *Pergamon Press*, **6**, 1–5.

Lin, J. T. and Y. H. Pao, 1979: Wakes in stratified fluids. *Annu. Rev. Fluid Mech.* **11**, 317–338.

Locarnini, R. A., A. V. Mishonov, J. I. Antonov, T. P. Boyer, H. E. Garcia, O. K. Baranova, M. M. Zweng, C. R. Paver, J. R. Reagan, D. R. Johnson, M. Hamilton, and D. Seidov, 2013. World Ocean Atlas 2013, Volume 1: Temperature. S. Levitus, Editor; A. Mishonov, Technical Editor, *NOAA Atlas NESDIS 73*, 40.

Meunier, P. and G. R. Spedding, 2004: A loss of memory in stratified momentum wakes. *Phys. Fluids* **12**, 298–305.

Meunier, P. and G. R. Spedding, 2006: Stratified propelled wakes. *J. Fluid Mech.* **552**, 229–256.

Newman, T. P., 2014: Surface signatures of submerged bodies propagating in stratified fluids. *Master's Thesis, Department of Oceanography, Naval Postgraduate School*, 59.

Novikov, B. G., 2009: Numerical simulation of dynamics of turbulent wakes behind towed bodies in linearly stratified media. *J. Eng. Thermo.* **18**, 279.

Orlanski, I., 1976: A simple boundary condition for unbounded hyperbolic flows. *J. Comput. Phys.* **21**, 251–269.

Schnitzler, H. U., E. K. V. Kalko, I. Kaipf, and A. D. Grinnell, 1994: Fishing and echolocation behavior of the greater bulldog bat, Noctilio leporinus, in the field. J. Behav. Eco. Sociobio. **35**, 327–345.

Voropayev, S. I. and S. A. Smirnov, 2003: Vortex streets generated by a moving momentum source in a stratified fluid. *Phys. Fluids* **15**, 618–624.

Zweng, M. M, J. R. Reagan, J. I. Antonov, R. A. Locarnini, A. V. Mishonov, T. P. Boyer, H. E. Garcia, O. K. Baranova, D. R. Johnson, D. Seidov, and M. M. Biddle, 2013. World Ocean Atlas 2013, Volume 2: Salinity. S. Levitus, Editor, A. Mishonov Technical Editor; NOAA Atlas NESDIS 74, 39.

INITIAL DISTRIBUTION LIST

1. Defense Technical Information Center
    Ft. Belvoir, Virginia

2. Dudley Knox Library
    Naval Postgraduate School
    Monterey, California